Novel aspects of radiation pressure in hybrid quantum systems

A Thesis

by

Sanket Das
Reg. no. 176121008

Supervisor:
Prof. Tarak Nath Dey

Submitted in partial fulfilment of the requirements for the award of

Doctor of Philosophy

Department of Physics
Indian Institute of Technology Guwahati

July 2024

Dedicated to my family

Declaration

I hereby declare that the contents of this thesis are original and have not been submitted for consideration for any other degree or qualification in this, or any other university. This dissertation is my own work and contains nothing which is the outcome of work done by others, except for the collaboration as specified in the text and acknowledgments.

Sanket Das
July 2024

Certificate

This is to certify that the work contained in the thesis entitled "**Novel aspects of radiation pressure in hybrid quantum systems**" submitted by Sanket Das in the partial fulfillment of the requirement for the award of the degree of Doctor of Philosophy in Physics, Department of Physics, Indian Institute of Technology Guwahati, is a record of the candidate's own work carried out by him under my supervision and guidance. The matter embodied in this report has not been submitted in part or full to any other university or institute for the award of any degree.

Dr. Tarak Nath Dey
Professor
Department of Physics
Indian Institute of Technology Guwahati
Guwahati - 781039
Assam, India.

Acknowledgment

Firstly, I express my humble gratitude to my thesis supervisor, Professor Tarak Nath Dey, for his constant guidance, encouragement, and freedom to endeavor in a new subject of cavity optomechanics during my Ph.D tenure. I have always been motivated by his highly hard-working capabilities. I am also thankful to him for allowing me to be involved in different types of problems and collaborations that immensely helped me increase my experience and knowledge about the subject.

I acknowledge my doctoral committee members- Prof. Bosanta Ranjan Boruah, Dr. Pankaj Kumar Mishra, and Dr. Vinay Wagh, for their valuable suggestions during the yearly assessment of the research work. I am deeply thankful to all HODs (Prof. Subhradip Ghosh, Prof. Perumal Alagarsamy, and Prof. Bosanta Ranjan Boruah) for their help during my Ph.D tenure. I also thank all the academic and non-academic staff of the physics department who helped me in various ways. I want to express my appreciation for Prasenjit-da, with whom engaged in lighthearted chats rather sometimes.

I am grateful to the Ministry of Human Resource and Development, Government of India, and IIT Guwahati for the financial support during my Ph.D tenure. I would also like to thank the Department of Physics at IIT Guwahati for providing the essential computational facilities.

I want to thank my former and present group members, Dr. Sandeep Sharma, Dr. Nawaz Sarif Mallick, Dr. Nilamoni Daloi, Samit Kumar Hazra, Partha Das, Madan Mohan Mahana, and Guanjan Yadav for their continuous support and wonderful friendship.

I want to express my heartfelt gratitude to all my fellow batchmates - Surojit, Samit, Rony, Subrata, Arghyajit, Pronoy, Tathagata, Riajul, Shilpi, Nitu, and Manisha. Your care and support have been invaluable during this journey. I am also grateful for the cherished memories shared with Sovan, Rajat, Rajesh-da, Nasimul-da, Subhadeep-da, Ayan, Subhasish, Niloy, Swarup, Golam, Sahabub, Gargi, Soumen, Gourav, Sudam, Tushar and many others. I would also like to thank the members of our Kameng Hostel group, Anjishnu, Arin, Aritra Mitra, Anindya, Aritra Roy, Tandrima, Jyotirmoy, Santanu, Partha, Adri, Tanay, Alik for being there at every ups and downs throughout the long Ph.D. journey.

I want to express my heartfelt gratitude to all my cricket teammates of Bengal tigers and department of Physics. I hope both the teams will win many more PPL and ISPL trophies in the upcoming days. All the very best guys!

Finally, I thank my parents and all my family members for their unconditional love and care. Without their support and inspiration, I would not have been able to take a single step forward. Their simple lifestyle and understanding of life made me realize the importance of being a good human being in any aspect of life.

Abstract

The study of radiation pressure involves a wave's average force on a surface or a particle. This force arises from the transfer of linear momentum when the wave interacts with the surface or particle. The study covers various applications, from the universe's development to modern laser applications, such as optical tweezers and cavity optomechanics. In cavity optomechanics, when a laser is reflected from a surface, it generates various types of elastic waves that travel through the object but are generally delicate. In simple terms, light can cause a slight movement within the material. This light-induced mechanical deformation has been observed in whispering-gallery-mode resonators and optomechanical crystals with photonic and phononic modes. In recent years, researchers have made significant efforts to understand the quantum nature of macroscopic systems, ranging from dimensions of micrometers to nanometers. The use of radiation pressure has led to the achievement of quantum entanglement between macroscopic objects, quantum state transfer, ponderomotive squeezing, and ground state cooling of the mechanical mode, resulting in the quadrature squeezing of a mechanical mode. The radiation pressure force gives rise to various physical phenomena arising from semi-classical light-matter interaction. For example, optomechanical systems exhibit a mechanical analog of Electromagnetically Induced Transparency (EIT), as proposed by Harris et al. in 1990. In EIT, an initially opaque three-level atomic medium becomes transparent with strong control and weak probe fields. The destructive interference between two excitation pathways generates a narrow transparency window and an anomalous dispersion, giving rise to slow light effects. In the presence of a strong drive field and a weak probe field, an optomechanical system with a single cavity mode and an acoustic mode closely resembles an atomic three-level system. In this analogy, the cavity decay rate and the mechanical damping mirror the radiative and non-radiative decay rates in the atomic system, respectively. In the second and third chapters of the thesis, we have formulated two problems based on the EIT phenomenon in an optomechanical and magnomechanical platform. In the final problem, we investigated various quantum effects, such as optical field squeezing, bipartite, and tripartite entanglement generation in a hybrid optorotational system consisting of annularly trapped Bose-Einstein condensates.

The thesis contains five chapters. Chapter 1 serves as the introduction of the thesis. We begin the discussion by quantizing the electromagnetic field inside a Fabry-Perot cavity, followed by the system-reservoir interaction, essential to describe a damping process. Then, we briefly discuss the resonator-generated optical lattice by invoking the quantized atom-field interaction. We then delve into the optomechanical interaction, highlighting its various consequences, such as optomechanical cooling, macroscopic entanglement generation, and Optomechanically Induced Transparency.

Chapter 2 proposes a controllable output field generation in a ring cavity resonator that comprises two nearly degenerate movable mirrors. In addition to the robust control and weak probe fields, we apply an external mechanical drive to produce mechanical coherences. Under the appropriate conditions, the control field's phase and the mechanical drive intensity enable controllable resonator-generated output field intensity that also enables distortionless pulse propagation through the medium.

Chapter 3 investigates the controllable probe field transmission in a magnomechanical system that consists of two coupled microwave resonators. One of them comprises a ferrimagnetic yttrium iron garnet (YIG) sphere. An external bias field activates its magnon mode and deforms its shape. The shape deformation leads to the magnon-phonon coupling. The magnon mode also interacts with the cavity mode. The system exhibits significant absorption when both cavities are passive. However, introducing gain to the auxiliary cavity can help us to produce an overall gain to the system along with anomalous dispersion. Hence, the output probe pulse amplifies with superluminal probe pulse propagation. Furthermore, adjusting the strength of photon exchange interaction can regulate the effective gain and the steepness of the dispersion curve. Consequently, the output probe pulse amplifies, and either the group velocity of the probe pulse surpasses the speed of light in a vacuum. Our research also establishes an upper limit for intensity amplification, and it elucidates that the advancement of the probe pulse is contingent on stability conditions.

Chapter 4 presents a hybrid optomechanical system featuring an annularly trapped Bose-Einstein condensate within an optical cavity. The cavity is stimulated by optical Laguerre-Gaussian modes and comprises two spiral phase elements serving as the cavity's end mirrors. The rear mirror undergoes torsional oscillations around the cavity's axis via a clamped support, creating a rotational counterpart to standard optomechanics. In this hybrid setup, we investigate the possibility of linking the optical amplitude and phase quadratures to produce ponderomotive squeezing. We also explore various bipartite and tripartite entanglements among the cavity, atomic matter waves, and the macroscopic rotating mirror.

In chapter 5, we provide the conclusion of this thesis along with future prospective of related research work.

Contents

1 Introduction **20**
- 1.1 Two mirror cavity . . . 21
  - 1.1.1 Bandwidth, finesse and quality of two mirror cavity . . . 22
- 1.2 Quantization of the Electromagnetic field . . . 23
  - 1.2.1 System-reservoir interaction . . . 25
- 1.3 Quantization of the Paraxial electromagnetic field . . . 26
- 1.4 The Jaynes-Cummings model . . . 28
  - 1.4.1 Resonator generated optical lattice . . . 29
- 1.5 Optomechanical interaction . . . 30
- 1.6 Dynamics of an optomechanical system . . . 32
  - 1.6.1 Stability Analysis . . . 33
- 1.7 Optomechanical cooling . . . 34
- 1.8 Optomechanical Entanglement . . . 36
- 1.9 The standard quantum limit . . . 37
- 1.10 Optomechanically induced transparency . . . 39
- 1.11 Cavity magnomechanics . . . 43
- 1.12 Outline of the Thesis . . . 45

2 Phase-dependent controllable field generation in a ring cavity resonator **46**
- 2.1 Introduction . . . 46
- 2.2 Theoretical model . . . 47
- 2.3 Numerical results of the controllable output probe field generation . . . 51
  - 2.3.1 Group delay . . . 55
- 2.4 Controllable Stokes field generation . . . 58
- 2.5 Conclusion . . . 59

3 Gain assisted controllable fast light generation in cavity magnomechanics **61**
- 3.1 Introduction . . . 61
- 3.2 Theoretical Model . . . 62
- 3.3 Results . . . 66
  - 3.3.1 Stability Analysis . . . 66
  - 3.3.2 Absorption and dispersion spectrum . . . 67
  - 3.3.3 Output probe transmission . . . 71
  - 3.3.4 Group delay . . . 73
- 3.4 Conclusion . . . 75

4 Hybrid Rotational Cavity Optomechanics Using Atomic Superfluid in a Ring **77**
4.1 Introduction . . . 77
4.2 Model . . . 79
4.2.1 Ring BEC . . . 79
4.2.2 Optical Cavity . . . 80
4.3 Quantum Dynamics . . . 80
4.3.1 Hamiltonian . . . 80
4.3.2 Steady State . . . 82
4.3.3 Stability Analysis . . . 83
4.4 Ponderomotive Squeezing . . . 83
4.4.1 Quadrature Noise Spectrum . . . 83
4.4.2 Optimum Squeezing . . . 85
4.5 Entanglement . . . 87
4.5.1 Bipartite Entanglement . . . 87
4.5.2 Tripartite Entanglement . . . 90
4.6 Conclusion . . . 91

5 Conclusions and future plan **93**

A Appendix of chapter 4 **95**
A.1 Power Spectral Density . . . 95
A.2 Optimized Squeezing . . . 96

List of Figures

1.1 A schematic of the Fabry-Perot cavity with two mirrors separated by a distance of L. The reflectance and transmittance of the first mirror are r_1, and t_1, respectively. Similarly, the second mirror's reflectance and transmittance are r_2, and t_2. 22

1.2 Electric field inside a cavity of length L is shown. The polarization of the electric field is considered in the x-direction and it is propagating along z-direction. 24

1.3 Schematic diagram of an optical cavity driven by Laguerre-Gaussian modes. The cavity comprises two spiral phase plates. The colored arrows signify the orbital angular momentum at different positions: The purely extra cavity field, the purely intracavity field and the intracavity field arising from the intracavity field are green, red, and blue arrows, respectively. 27

1.4 Schematic diagram of a Fabry-Perot cavity with one partially transmittive fixed mirror while the movable rear mirror is perfectly reflective. 30

1.5 Steady-state photon number is shown as a function of (a) input power for three different detuning cases and (b) cavity detuning for three different input powers. The resonance frequency of the movable mirror is $\omega_m/2\pi = 10$ MHz, mass of the mirror is $m = 250$ ng, the damping of the mirror is $\gamma_m/2\pi = 100$ Hz, the cavity decay rate is $\kappa = 0.75\ \omega_m$. 32

1.6 The stable and unstable regions are determined as functions of the normalized effective optomechanical coupling G/ω_m and the normalized detuning Δ_c/ω_m. All the other parameters are same as in Figure 1.5. 34

1.7 The effective phonon number as a function of the optical field intensity and the normalized cavity detuning. The cavity length is $L = 1$ mm, mass of the movable mirror is $m = 250$ ng and the environmental temperature of the mirror is $T = 2$ K. All the other parameters are same as in Figure 1.6. 36

1.8 The logarithmic negativity is plotted as a function of (a) cavity detuning when the mirror's bath temperature is 0.4 K and (b) the environmental temperature of the movable mirror when $\Delta_c = \omega_m$. We have considered the effective optomechanical coupling strength $G = -0.4\ \omega_m$ for the numerical simulation. All the other parameters are same as in Figure 1.6. 37

1.9 Power spectral density for different bath temperatures is shown. The cavity's length and resonance frequency are $L = 1$ mm and $\omega_c/2\pi = 10^{15}$ Hz. All the other parameters are the same as in Figure 1.6. With all these parameters, the optimal power is $P_{in} = 1.2$ μW. 39

1.10 Schematic diagram of an optomechanical system. A red-detuned strong coupling field of frequency ω_c and a weak probe field of frequency ω_p are applied. The output field is denoted by ε_{out}. 40

1.11 Various components of the intracavity field is shown as a function of probe detuning when (a) $P_c/P_p = 100$, and (b) $P_c/P_p = 2.04$. The wavelength of coupling laser $\lambda = 2\pi c/\omega_c = 1064$ nm, $L = 25$ mm, $m = 145$ ng, $\kappa = 2\pi \times 215$ KHz, $\omega_m = 2\pi \times 947$ KHz, $\gamma_m = 2\pi \times 141$ Hz, the cavity detuning is $\Delta_c = \omega_m$ and coupling laser power $P_c = 6.9$ mW. 41

1.12 Absorption and dispersion spectrum is shown with respect to δ. All the other parameters are same as in Figure 1.11(a). 42

1.13 Schematic of yttrium iron garnet (YIG) sphere interacting with a cavity mode a. The bias magnetic field along z-direction activates the magnon mode of the YIG sphere. 43

2.1 Schematic diagram of a ring cavity resonator. A strong coupling field of frequency ω_c and a weak probe field of frequency ω_p are applied along with a weak mechanical drive of frequency ω_m. The two movable mirrors have different resonant frequencies ω_1 and ω_2. 48

2.2 The level diagram of the ring cavity optomechanical system. $|N\rangle$, $|n_1\rangle$ and $|n_2\rangle$ are the number states of the cavity mode, phonon modes of the first and second nanomechanical oscillators, respectively. The application of a strong control field to the red-detuned cavity allows the transition $|N+1, n_1, n_2\rangle \leftrightarrow |N, n_1+1, n_2\rangle$. Whereas the presence of a weak probe field increases the cavity photon number by unity. An external weak mechanical force directly couples $|N, n_1, n_2\rangle \leftrightarrow |N, n_1+1, n_2\rangle$. 52

2.3 Normalised transmission at the upper mechanical sideband is plotted against normalized mechanical drive detuning for different control powers. The other parameters are $\omega_1 = 2\pi \times 56.98$ MHz, $\omega_2 = 2\pi \times 46.62$ MHz, $\gamma_1 = \gamma_2 = 2\pi \times 4.1$ KHz, $\kappa = 2\pi \times 15$ MHz and the effective cavity detuning is $\Delta' = 2\pi \times 51.8$ MHz. 53

2.4 The control field phase-dependent normalized transmission of the output probe field is plotted as a function of normalized detuning between the control and the probe field when the mechanical drive is in-phase with the input probe field. All other parameters are the same as before. 54

2.5 The normalized optical probe field transmission through the upper transparency window is plotted as a function of normalized mechanical drive amplitude for different values of the control field phase. Here we consider the control field power to be 2 mW. 54

2.6 Time delay of the probe pulse for different mechanical drive amplitudes have been plotted against the normalized probe detuning δ/Δ' while the control power is 2 mW. The mechanical drive is considered to be in-phase with the probe field. All other parameters are taken as the same as Figure 2.3. 56

2.7 The normalized probe pulse intensity with respect to its peak value is plotted against the normalized time $\Gamma\tau$. The solid black curve represents the input probe pulse propagating at speed c through the ring cavity. The red dashed and the blue dot-dashed curves represent the output probe pulse in the presence of mechanical pump with $\eta = 0.07$ and 0.25, respectively. Variation of the relative intensity of the output probe pulse is shown in the inset. 57

2.8 The normalized lower sideband transmission is plotted against normalized mechanical drive detuning for three different control powers $P_c = 2, 5$ and 10 mW. All other parameters are same as in Figure 2.3. 58

2.9 The normalized intensity of the generated Stokes field is plotted as a function of normalized detuning between the control and the probe field. The mechanical drive is in-phase with the input probe field. The control power is taken as 2 mW. All other parameters are same as in Figure 2.3. 59

2.10 The normalized intensity of the generated Stokes field through the upper transparency window is plotted as a function of normalized mechanical drive amplitude for different values of the control phase. The external mechanical pump is considered to be in-phase with the applied probe field ($\phi_m = \phi_p$). Here we consider the control field power to be 2 mW. 60

3.1 The schematic diagram of a hybrid cavity magnomechanical system. The system consists of two coupled microwave cavities. One of them is passive, and another one is active. The passive cavity contains a ferrimagnetic YIG sphere inside it. The applied bias magnetic field produces the magnetostrictive interaction between magnon and phonon. The coupling rates between the magnon-photon and magnon-phonon are g_{ma} and g_{mb}, respectively. Strong control field of frequency ω_l and a weak probe field of frequency ω_p are applied to the passive cavity. The output field is denoted as ε_{out}. 63

3.2 The stable and unstable regions are determined as a function of normalized evanescent coupling strength (J/κ_1) and the cavity-magnon coupling strength (g_{ma}) when the loss of the CMM-resonator is perfectly balanced by the gain of the auxiliary cavity ($\kappa_1 = \kappa_2$). We consider the control field intensity to be 10 mW. The other parameters are $\omega_c = 2\pi \times 7.86$ GHz, $\omega_b = 2\pi \times 11.42$ MHz, $\Delta_a = \Delta'_m = \omega_b = 2\pi \times 11.42$ MHz, $\kappa_1 = \kappa_2 = \pi \times 3.35$ MHz, $\kappa_m = \pi \times 1.12$ MHz, $\kappa_b = \pi \times 300$ Hz, and $g_{mb} = 2\pi$ Hz. 67

3.3 The ratio of the noise intensity (of the passive resonator) with respect to the steady-state field intensity (of the passive resonator) is plotted as a function of normalized time under the magnomechanical resonance condition ($\delta = \omega_b$). We consider the control and the probe field intensity to be 10 mW and 10 nW, respectively. All the other parameters are the same as Figure 3.2. 68

3.4 Level diagram of the model system. $|n_i\rangle$,$|m\rangle$ and $|b\rangle$ represents the photon number state of i^{th} cavity, magnon mode and phonon mode, respectively. The presence of a weak probe field increases the photon number of CMM resonator by unity. The magnon-photon interaction couples $|n_1 + 1, n_2, m, b\rangle$ and $|n_1, n_2, m + 1, b\rangle$. Whereas g_{mb} couples $|n_1, n_2, m + 1, b\rangle$ and $|n_1, n_2, m, b + 1\rangle$. The hopping interaction between the two cavities directly couples $|n_1 + 1, n_2, m, b\rangle \leftrightarrow |n_1, n_2 + 1, m, b\rangle$. 68

3.5 (a) Absorption and (b) dispersion spectrum of the model system. The slope of the dispersion curve is shown in the inset. Here we consider both the microwave cavities are passive, with identical decay rates ($\kappa_1 = -\kappa_2$). The magnon-photon couplong strength, g_{ma} is taken as 2 MHz. All the other parameters are the same as in Figure 3.2. . . . 69

3.6 (a) Absorption and (b) dispersion spectrum of the model system. The slope of the dispersion curve is shown in the inset. Here we consider the second cavity as a gain cavity, with $\kappa_2 = \kappa_1$. All the other parameters are the same as in Figure 3.2. 70

3.7 Exchange interaction-dependent normalized output probe transmission is plotted as a function of normalized detuning between the control and the probe field when (a) both the cavities are passive ones, in the inset we present the same quantity at the extreme vicinity of the magnomechanical resonance, and (b) one is active and another one is passive. All the other parameters are taken the same as in Figure 3.2. 72

3.8 The output probe transmission response at $\delta = \omega_b$ is presented as a function of J. In the inset the enhanced magnon-phonon coupling strength is plotted as a function of photon exchange interaction strength. All the other parameters are the same as in Figure 3.2. . . . 73

3.9 Time delay of the probe pulse for different evanescent coupling strength J have been plotted against the normalized probe detuning δ/ω_b, while the control power is 10 mW. All other parameters are taken as the same as in Figure 3.2. 74

3.10 The relative intensity of the output probe pulse is plotted against the normalized time (Γt) for different photon-photon exchange interaction strengths when both cavities are operating under balanced gain-loss condition. The input probe pulse width, Γ is taken as 7.17 kHz. All the other parameters are the same as in Figure 3.2. 74

4.1 Schematic diagram of a hybrid setup consisting of a ring BEC inside a cavity. The cavity comprises two spiral phase elements: one is fixed and partially transmissive, while the other is rotating and highly reflective. The colored arrows show the orbital angular momentum at different positions: The purely extra cavity field, the purely intracavity field, and the intracavity field arising from the intracavity field are green, red, and blue arrows, respectively. The interference between the transmitted and the reflected intracavity fields produces an optical lattice that probes the ring BEC with winding number L_p. 79

4.2 Bistability plot as a function of (a) input power and (b) cavity detuning. Here $\tilde{\Delta}_{\rm cr}/2\pi = -0.17$ MHz, and $P_{\rm cr} = 1$ pW. The parameters used are $R = 12$ μm, $N = 10^4$, $\omega_\rho/2\pi = \omega_z/2\pi = 840$ Hz, $\gamma_o/2\pi = 0.2$ MHz, $\Delta_a/2\pi = 5.4$ GHz, $g_a/2\pi = 0.7$ MHz, $U_0/2\pi = 90.7$ Hz, $L_p = 1$, $l = 10$, $G/2\pi = 3.2$ kHz, $\gamma_m/2\pi = 0.8$ Hz, $\omega_o/2\pi = 10^{15}$ Hz, $a_{\rm Na} = 0.1$ nm, $\tilde{g} = 14\tilde{g}_m$, $\tilde{g}_m/2\pi = 78.8$ μHz, $L = 4$ mm, $M = 3.08$ μg, $\omega_\phi/2\pi = 653$ Hz, $\gamma_\phi = 0.1\gamma_m$, and $R_m = 15$ μm. 82

4.3 The stable and unstable regions are determined as functions of the normalized optorotational coupling g_ϕ/G and the normalized frequency of the rotating mirror ω_ϕ/Ω_d. We consider $\Delta^{'} = \omega_\phi$, $P_{\rm in} = 12.4$ fW. The other parameters are the same as in Figure 4.2. 84

4.4 (a) Power spectral density (PSD) of the output optical quadrature as a function of the response frequency $\omega/2\pi$, for the measurement angles $\theta = 90°$ (black solid line), $\theta = 30°$ (red dashed line), and $\theta = 5°$ (blue dot-dashed line). (b) PSDs as a function of the measurement angle θ. Black solid, and black dot-dashed curves are produced by fixing the response frequency near Ω_d and Ω_c, respectively. Also, in these plots the spectrum is normalized to the shot noise (black dotted line). Parameters used are $T = 10$ nK, $T_\phi = 1$ mK and other parameters are same as in Figure 4.3. 85

4.5 Optimized PSD of the optical quadrature as a function of the response frequency for $G/2\pi = 3.2$ kHz (black solid line), $G/2\pi = 9.6$ kHz (red solid line), and $G/2\pi = 22.4$ kHz (blue solid line). Parameters used are same as in Figure 4.2. 86

4.6 Optimized PSD of the output optical quadrature plotted at the frequency of the rotating mirror as a function of the winding number L_p. Parameters used are same as in Figure 4.2. 87

4.7 Various bipartite entanglements are plotted as a function of (a) cavity detuning when the orbital angular momentum of the input field $l = 243$ (b) the OAM of the driving field for $L_p = 1$ and (c) the winding number of BEC for $l = 243$ while the cavity detuning is $\Delta' = -1.2\omega_\phi$. We consider the resonance frequency of the rotating mirror to be $\omega_\phi = 3$ MHz, mass of the mirror $M = 0.1$ ng, radius $R_m = 20$ μm, the cavity length $L = 1$ mm, $\gamma_0/2\pi = 0.48$ MHz, $\gamma_m/2\pi = 0.8$ Hz, $\gamma_\phi/2\pi = 4.77$ Hz, $\omega_0/2\pi = 10^{15}$ Hz, $G/2\pi = 7.67$ kHz, $U_0/2\pi = 153.5$ Hz, $\Delta_a = 1.04$ GHz, $\omega_\rho/2\pi = 8.4$ kHz, and $a_{Na} = 2.5$ nm. The input power of the driving field is 0.19 nW. The bath temperature of the rotating mirror is $T_\phi = 5$ mK and the temperature of the atomic side modes are $T = 10$ nK. All the other parameters are same as in Figure 4.2. 88

4.8 The mean phonon number of the rotating mirror as a function of the topological charge of the input field when $L_p = 1$. The inset presents the variation of effective phonon number as a function of the winding number of BEC for $l = 243$. The dotted lines correspond to the unity of the effective phonon number. All the other parameters are the same as in Figure 4.7. 89

4.9 Tripartite entanglement in terms of minimum residual contangle versus (a) cavity detuning for $l = 243$, (b) the OAM of the driving field for $L_p = 1$ and $\Delta' = -1.9\omega_\phi$. The black solid curve accounts for the tripartite entanglement associated with the cavity-mirror-atomic c mode. The red solid curve accounts for the tripartite entanglement associated with the cavity-mirror-atomic d mode. All the other parameters are same as in Figure 4.7. 91

Chapter 1

Introduction

The mechanical pressure from the electromagnetic radiation exposed to any surface is known as radiation pressure. In the early seventeenth century, Johannes Kepler identified the role of radiation pressure to explain why the tails of a comet point away from the sun. In 1871, J.C. Maxwell theoretically predicted that the object's and electromagnetic fields' momentum exchange caused the radiation pressure [1]. In 1901, three decades after the theory was proposed, Peter Lebedew conducted the first experimental verification of it by measuring the mechanical pressure exerted by light on a solid body [2]. In the 1970s, Braginsky and his colleagues investigated the effect of radiation pressure in the context of measurement sensitivity of gravitational wave interferometers [3]. They also predicted radiation pressure-induced dynamical instabilities [4] and the cooling of a mechanical oscillator [5]. From then, various advancements in micro- and nanofabrication techniques have led to numerous studies aimed at reducing the size of mechanical components. Decreasing the size of the mechanical oscillator raises its resonance frequency, thereby enhancing the sensitivity of the optomechanical system to mechanical displacement [6–8]. The coupling between optical and mechanical components has been reported in high-finesse optical microtoroid resonators [9–11], nanorods inside Fabry-Perot resonators [12], whispering gallery microdisks [13, 14], optomechanical crystals [8], Fabry-Perot cavity with a movable end mirror [15–17], with a semi-transparent mirror placed inside a Fabry-Perot cavity [18–21], nanomechanical mirror coupled to a superconducting microwave cavity [22, 23] and so on. Utilizing the radiation pressure interaction, these various geometries has been realized to control optical pulse propagation [24,25], amplifying [26,27], and cooling of vibrational modes [28–30], wavelength conversion between optical and microwave fields [31,32], storage and retrieval of optical signal [33], entanglement generation between the optical and the vibrational mode [34–37], and squeezed light generation [38, 39]. Along with the investigations in cavity optomechanics, recently, a tremendous effort has been made to integrate different elements from distinct physical domains, such as optics, mechanics, and magnetic materials, via the interaction with quantized spin waves (magnons) [40–42]. The strong coupling between magnon and photon provides an excellent platform for studying various strong coupling cavity QED effects [43, 44]. Moreover, the tunability of magnon modes provides extra controllability over the standard optomechanical platforms that can be utilized in microwave field transmission [45, 46] and weak force detection [47]. All the studies mentioned above fall under the broader scope of Atomic, Molecular, and Optical (AMO) physics. The invention of the laser [48] opened up

a new dimension of AMO physics by manipulating the atoms or molecules. Paul and Dehmelt [49, 50] first successfully trapped single ions, and later on, the trapped ions are cooled down to nano-Kelvin temperature [51]. With this controllability, in 1995 a distinctive state of Bose-Einstein condensate (BEC) is born [52, 53], where a significant fraction of bosons occupy the same quantum state. Interacting BEC with a cavity field further probes new possibilities for controlling collective quantum effects, such as quantum entanglement [54, 55], superradiance [56, 57], and quantum synchronization [58].

This chapter briefly discusses the simplest Fabry-Perot cavity. We then quantize the electromagnetic field within a Fabry-Perot cavity and discuss the system-reservoir interaction, which is essential for describing a damping process. Next, we'll briefly touch on the resonator-generated optical lattice by considering the quantized atom-field interaction. After that, we'll explore the optomechanical interaction and highlight its various consequences, such as optomechanical cooling, generation of macroscopic entanglement, and Optomechanically Induced Transparency. Finally, we discuss the magnomechanical interactions as a building block of the Hybrid solid-state platform.

1.1 Two mirror cavity

We begin the discussion, by considering a Fabry-Perot interferometer or cavity consisting of two mirrors separated by a distance L. Each mirror is considered as a beam splitter. Using the beam splitter conventions, electric field amplitude at different positions of Figure 1.1 satisfies the relations,

$$\begin{aligned} E_a &= it_1 E_{in} + r_1 E_b, \\ E_b &= r_2 e^{2iKL} E_a, \\ E_t &= it_2 e^{iKL} E_a, \\ E_r &= r_1 E_{in} + it_1 E_b, \end{aligned} \tag{1.1}$$

where the plane wave incorporates an extra phase factor e^{iKL} after traveling a distance L. The equations in Eq. (1.1) are linear and can be solved easily to produce the intensity ratios at different locations

$$I_t = \left|\frac{E_t}{E_{in}}\right|^2 = \frac{(t_1 t_2)^2}{(1 - r_1 r_2)^2 + 4 r_1 r_2 \sin^2 KL}, \tag{1.2a}$$

$$I_r = \left|\frac{E_r}{E_{in}}\right|^2 = \frac{(r_1 - r_2)^2 + 4 r_1 r_2 \sin^2 KL}{(1 - r_1 r_2)^2 + 4 r_1 r_2 \sin^2 KL}, \tag{1.2b}$$

$$I_a = \left|\frac{E_a}{E_{in}}\right|^2 = \frac{t_1^2}{(1 - r_1 r_2)^2 + 4 r_1 r_2 \sin^2 KL}. \tag{1.2c}$$

From Eq. (1.2a), it is evident that the transmitted field intensity (I_t) vanishes if the transmittance of any one or both mirrors is zero. For non-vanishing transmittance ($t_{1,2} \neq 0$), the maximum transmission occurs at the resonance frequencies $\nu = nc/2L$, $n = 1, 2, 3...$, where c is the velocity of light in vacuum. The frequency separation between two successive resonances is known as the free spectral range, $\Delta\nu = c/2L$.

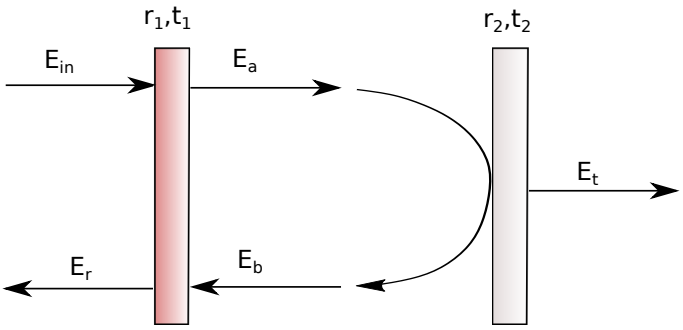

Figure 1.1: A schematic of the Fabry-Perot cavity with two mirrors separated by a distance of L. The reflectance and transmittance of the first mirror are r_1, and t_1, respectively. Similarly, the second mirror's reflectance and transmittance are r_2, and t_2.

As a consequence of the conservation of energy, the reflected and transmitted fields satisfy the relation $I_t + I_r = 1$. Under the resonance condition ($KL = n\pi$), Eq. (1.2b) suggests that the relative intensity of the reflected field reads $I_r^{res} = (r_1 - r_2)^2/(1 - r_1 r_2)^2$, which vanishes for $r_1 = r_2$. It is known as the impedance-matched condition. However, I_r^{res} can be unity if one of the mirrors is perfectly reflective *i.e.,* either $r_1 = 1 \neq r_2$ or $r_2 = 1 \neq r_1$.
However, the circulating photons inside the cavity have non-vanishing intensity as the transmittance of the input mirror becomes non-zero. The circulating field's intensity at the resonance frequencies is $I_{a,max} = t_1^2/\left(1 - r_1 r_2\right)^2$. Experimentally, the circulating field's intensity can be enhanced 10^5 times when both the mirrors have the same reflectance ($r_1 = r_2 = r$). Even when both mirrors have different reflectances ($r_1 \neq r_2$), one can enhance the intensity of the circulating photon. For $r_2 = 1$, we calculate $I_a = (1 + r_1)/(1 - r_1)$, which increases with r_1 and diverges as $r_1 \to 1$. Hence, a Fabry-Perot cavity with a perfectly reflective end mirror and a slightly transmissive input mirror can be used to enhance the intensity of the circulating photons inside the cavity.

1.1.1 Bandwidth, finesse and quality of two mirror cavity

The bandwidth of the cavity field can be evaluated by identifying the wave-number ($K_\pm$) associated with the half of the maximum intensity, $I_a = I_{a,max}/2$. Using Eq. (1.2c), the condition reads

$$\frac{t_1^2}{\left(1 - r_1 r_2\right)^2 + 4 r_1 r_2 \sin^2(K_\pm L)} = \frac{t_1^2}{2\left(1 - r_1 r_2\right)^2}. \tag{1.3}$$

Defining the cavity bandwidth as

$$\delta\nu = \frac{\omega_+ - \omega_-}{2\pi} = \frac{\gamma_0}{2\pi}, \tag{1.4}$$

we find

$$\gamma_0 = \frac{2c}{L} \sin^{-1}\left(\frac{1 - r_1 r_2}{2\sqrt{r_1 r_2}}\right), \tag{1.5a}$$

$$\delta\nu = \frac{c}{\pi L}\sin^{-1}\left(\frac{1-r_1r_2}{2\sqrt{r_1r_2}}\right) \approx \frac{c}{2\pi L}\left(\frac{1-r_1r_2}{\sqrt{r_1r_2}}\right), \tag{1.5b}$$

where in the last step, we consider the argument of the inverse sin function to be small. The finesse of the cavity measuares the sharpness of the intensity resonance with respect to the spectral separation between the two successive resonance. The cavity finesse can be evaluated as

$$\mathcal{F} = \frac{\text{free spectral range}}{\text{bandwidth}} = \frac{\Delta\nu}{\delta\nu} \approx \frac{\pi\sqrt{r_1r_2}}{1-r_1r_2}. \tag{1.6}$$

The quality factor of a cavity measures the efficiency of storing energy with respect to the energy lost per cycle. It can be quantified as

$$Q = \frac{\text{resonance frequency}}{\text{bandwidth}} = \frac{\nu}{\delta\nu} = n\mathcal{F}. \tag{1.7}$$

1.2 Quantization of the Electromagnetic field

This section discusses the quantization of the electromagnetic field in a vacuum. The Maxwell's equation can describe the propagation of an electromagnetic field in free space. In mks units, Maxwell's equations are

$$\vec{\nabla}\cdot\vec{D} = 0, \qquad \text{(Gauss's Law)} \tag{1.8a}$$

$$\vec{\nabla}\cdot\vec{B} = 0, \tag{1.8b}$$

$$\vec{\nabla}\times\vec{E} = -\frac{\partial\vec{B}}{\partial t}, \qquad \text{(Faraday's Law)} \tag{1.8c}$$

$$\vec{\nabla}\times\vec{H} = \frac{\partial\vec{D}}{\partial t}, \qquad \text{(Ampere's Law)} \tag{1.8d}$$

with the relations

$$\vec{B} = \mu_0\vec{H}, \tag{1.9a}$$

$$\vec{D} = \epsilon_0\vec{E}. \tag{1.9b}$$

The electric field, magnetic field, electric displacement, and magnetic flux density vectors are expressed as $\vec{E}, \vec{H}, \vec{D}$, and $\vec{B}$, respectively. The free space permittivity and permeability are μ_0 and ϵ_0, respectively and they are related with the speed of light in vacuum as $c = 1/\sqrt{\mu_0\epsilon_0}$. Taking the curl of Eq. (1.8c) and using the relations Eq. (1.9a) and (1.9b), we obtain the wave equation in vacuum

$$\nabla^2\vec{E} - \frac{1}{c^2}\frac{\partial^2\vec{E}}{\partial t^2} = 0. \tag{1.10}$$

The wave equation of Eq. (1.10) describes the electromagnetic wave propagation through the vacuum. The spatial dependence of the electric field inside the cavity of length L (Figure 1.2) can be considered linearly polarized in the x-direction. In the cavity normal mode basis, the intracavity electric field takes the form

$$E_x(z,t) = \sum_n A_n q_n(t)\sin(k_n z), \tag{1.11}$$

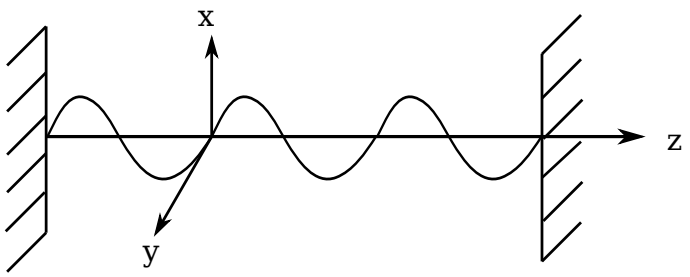

Figure 1.2: Electric field inside a cavity of length L is shown. The polarization of the electric field is considered in the x-direction and it is propagating along z-direction.

where q_n is the normal mode amplitude, and k_n is the wave number associated with n^{th} mode $k_n = n\pi/L$, with $n = 1, 2, 3, ...$ The coefficient $A_n = (2\omega_n^2 m_n/(V\epsilon_0))^{1/2}$, where $\omega_n = n\pi c/L$ is the cavity angular frequency, V is the cavity volume and m_n is a constant with a mass dimension, respectively. From Eq. (1.8d), one can find that the non-vanishing intracavity magnetic field associated with the intracavity electric field of Eq. (1.11) as

$$H_y(z,t) = \sum_n A_n \left(\frac{\dot{q}_n \epsilon_0}{k_n}\right) \cos(k_n z). \tag{1.12}$$

The total Hamiltonian of the intracavity electromagnetic field is

$$\mathcal{H} = \frac{1}{2}\int_V d\tau \left(\epsilon_0 E_x^2 + \mu_0 H_y^2\right), \tag{1.13}$$

where the integration comprises over the cavity volume. By substituting Eq. (1.11) and Eq. (1.12) into Eq. (1.13), the total Hamiltonian can be cast into the form

$$\mathcal{H} = \frac{1}{2}\sum_n \left(m_n \omega_n^2 q_n^2 + m_n \dot{q}_n^2\right), \tag{1.14a}$$

$$= \frac{1}{2}\sum_n \left(m_n \omega_n^2 q_n^2 + \frac{p_n^2}{m_n}\right), \tag{1.14b}$$

where $p_n = m_n \dot{q}_n$ is the canonical momentum of the n^{th} mode. Eq. (1.14b) implies that each cavity mode is dynamically equivalent to a mechanical harmonic oscillator. Consequently, the total Hamiltonian of the cavity field can be viewed as the sum of the energies of such independent mechanical harmonic oscillator. To quantize the Hamiltonian of Eq. (1.14b), we treat q_n and $p_{n'}$ as operators that obey the commutation relation

$$[q_n, p_{n'}] = i\hbar\delta_{nn'}, \tag{1.15a}$$

$$[q_n, q_{n'}] = [p_n, p_{n'}] = 0. \tag{1.15b}$$

Introducing a set of non-Hermitian annhilation (a) and creation operator ($a^\dagger$)

$$a_n = \frac{1}{\sqrt{2m_n\hbar\omega_n}}\left(m_n\omega_n q_n + i p_n\right), \tag{1.16a}$$

$$a_n^\dagger = \frac{1}{\sqrt{2m_n\hbar\omega_n}}\left(m_n\omega_n q_n - ip_n\right). \tag{1.16b}$$

In terms of photon creation and annihilation operators the cavity field Hamiltonian of Eq. (1.14b) can be reexpressed in quantized form

$$\mathcal{H} = \hbar\sum_n \omega_n\left(a_n^\dagger a_n + \frac{1}{2}\right), \tag{1.17}$$

where the creation and annihilation operators satisfies the commutation relation

$$\left[a_n, a_{n'}^\dagger\right] = \delta_{nn'}, [a_n, a_{n'}] = \left[a_n^\dagger, a_{n'}^\dagger\right] = 0. \tag{1.18}$$

In terms of a_n and $a_n^\dagger$, the electric and magnetic fields can be expressed as

$$E_x(z,t) = \sum_n \mathscr{E}_n\left(a_n + a_n^\dagger\right)\sin(k_n z), \tag{1.19}$$

$$H_y(z,t) = -i\epsilon_0 c\sum_n \mathscr{E}_n\left(a_n - a_n^\dagger\right)\cos(k_n z), \tag{1.20}$$

where $\mathscr{E}_n = \sqrt{\hbar\omega_n/(\epsilon_0 V)}$ carries the dimension of an electromagnetic field.

1.2.1 System-reservoir interaction

In this subsection, we briefly discuss the system-bath interaction considering a quantized cavity mode of frequency ν, interacting with all the bath modes of frequencies ν_k. The Hamiltonian of the system can be written as

$$H_0 = \hbar\nu a^\dagger a + \sum_k \hbar\nu_k b_k^\dagger b_k + \hbar\sum_k g_k\left(b_k^\dagger a + a^\dagger b_k\right). \tag{1.21}$$

The first and second terms correspond to the cavity's free energy and bath modes, respectively. The third term accounts for the system-bath coupling. The Heisenberg equation of motion of each operator reads

$$\dot{a} = -i\nu a(t) - i\sum_k g_k b_k(t), \tag{1.22a}$$

$$\dot{b}_k = -i\nu_k b_k(t) - ig_k a(t). \tag{1.22b}$$

The formal solution of Eq. (1.22b) is

$$b_k(t) = b_k(0)e^{-i\nu_k t} - ig_k\int_0^t dt' a(t')e^{-i\nu_k(t-t')}. \tag{1.23}$$

By substituting Eq. (1.23) into Eq. (1.22a), we get

$$\dot{a} = -i\nu a(t) - \sum_k g_k^2\int_0^t dt' a(t')e^{-i\nu_k(t-t')} + f_a(t), \tag{1.24}$$

where $f_a(t) = -i\sum_k g_k b_k(0)e^{-i\nu_k t}$ is the noise operator. Further, we apply a transformation rule $\tilde{a}(t) = a(t)e^{i\nu t}$ and Eq. (1.24) reduce to

$$\dot{\tilde{a}}(t) = -\sum_k g_k^2\int_0^t dt'\tilde{a}(t')e^{-i(\nu_k-\nu)(t-t')} + f_a(t)e^{i\nu t}. \tag{1.25}$$

Assuming the reservoir modes are closely spaced in frequency domain, we replace the summation over k by an integral

$$\sum_k \to \frac{2V}{(2\pi)^3}\int_0^{2\pi} d\phi \int_0^{\pi} d\theta\ \sin\theta \int_0^{\infty} dk\ k^2. \tag{1.26}$$

Then Eq. (1.25) reads

$$\dot{\tilde{a}}(t) = -\frac{V}{\pi^2 c^3}\int_0^{\infty} d\nu_k\ \nu_k^2\ g_k^2 \int_0^t dt' \tilde{a}(t') e^{-i(\nu_k-\nu)(t-t')} + f_a(t)e^{i\nu t}. \tag{1.27}$$

The significant contribution to the integration will occur around $\nu_k = \nu$, where the time integral is not negligible. We can extend the lower limit frequency integral upto $-\infty$ without loss of generality. By using the definition of the delta function

$$\int_{-\infty}^{\infty} d\nu_k e^{i(\nu-\nu_k)(t-t')} = 2\pi\delta(t-t'), \tag{1.28}$$

we obtain the Heisenberg-Langevin equation as

$$\begin{aligned}\dot{\tilde{a}}(t) &= \frac{V}{\pi^2}\int_0^t dt'\ \frac{\nu^2}{c^3}\ g_k^2\ \tilde{a}(t')\ 2\pi\delta(t-t') + f_a(t)e^{i\nu t},\\ &= -\kappa\ \tilde{a}(t) - i\sum_k g_k\ b_k(0)e^{-i(\nu_k-\nu)t},\end{aligned} \tag{1.29}$$

where the decay constant $\kappa = V\nu^2 g_k^2/(\pi c^3)$ and the noise operator is defined as $a_{in} = -i\sum_k g_k\ b_k(0)e^{-i(\nu_k-\nu)t}$.

1.3 Quantization of the Paraxial electromagnetic field

The electromagnetic field propagation in vacuum can be well understood by Eq. (1.10). Finding the analytical solutions to Eq. (1.10) is challenging. However, the analytical solution can be obtainable under slowly varying envelope approximation. Consider a quasi-monochromatic wave propagating along the z-direction inside a vacuum. One can write the electric field inside the vacuum as

$$\vec{E}(x,y,z,t) = \hat{e}\mathcal{E}(x,y,z,t)e^{-i(\omega t-kz)} + \text{c.c.}, \tag{1.30a}$$

where, $\hat{e}$ is the unit vector, ω is the carrier field frequency associated with the wave number $k = \omega/c$, and $\mathcal{E}$ represents the envelope functions of the field. By substituting the above ansatz to Eq. (1.10), one obtains the following relations for corresponding derivatives as

$$\nabla^2\vec{E} = \hat{e}\left(\nabla_\perp^2\mathcal{E} + \frac{\partial^2\mathcal{E}}{\partial z^2} + 2ik\frac{\partial\mathcal{E}}{\partial z} - k^2\mathcal{E}\right)e^{i(kz-\omega t)} + \text{c.c.}, \tag{1.31a}$$

$$\frac{\partial^2\vec{E}}{\partial t^2} = \hat{e}\left(\frac{\partial^2\mathcal{E}}{\partial t^2} - 2i\omega\frac{\partial\mathcal{E}}{\partial t} - \omega^2\mathcal{E}\right)e^{i(kz-\omega t)} + \text{c.c.}, \tag{1.31b}$$

where $\nabla_\perp^2 = \partial^2/\partial x^2 + \partial^2/\partial y^2$ is the spatial derivative in x and y-direction (transverse plane). Under "*slowly varying envelope approximation*" (SVEA) the variation of the envelope function $\mathcal{E}$ satisfies the conditions

$$\left|k^2\mathcal{E}\right| \gg \left|k\frac{\partial \mathcal{E}}{\partial z}\right| \gg \left|\frac{\partial \mathcal{E}^2}{\partial^2 z}\right|, \quad \left|\omega^2\mathcal{E}\right| \gg \left|\omega\frac{\partial \mathcal{E}}{\partial t}\right| \gg \left|\frac{\partial \mathcal{E}^2}{\partial t^2}\right|, \tag{1.32a}$$

Substituting the above equation in Eq. (1.10) and neglecting the higher order time and space derivative, we get the Helmholtz equation under SVEA as:

$$\frac{1}{2ik}\nabla_\perp^2\mathcal{E} + \frac{\partial \mathcal{E}}{\partial z} + \frac{1}{c}\frac{\partial \mathcal{E}}{\partial t} = 0. \tag{1.33}$$

One of the solutions of the free space paraxial Helmholtz equation is the Laguerre-Gaussian (LG) mode, which describes the envelope profile of the field in the cylindrical coordinate system as

$$\begin{aligned}\mathcal{E}_p^l(r,\phi,z) = \mathcal{E}_0\frac{w_0}{w(z)}\left(\frac{r\sqrt{2}}{w(z)}\right)^{|l|} L_p^{|l|}\left(\frac{2r^2}{w^2(z)}\right)\exp\left[\frac{ikr^2}{2R(z)} - \frac{r^2}{w^2(z)}\right] \\ \times \exp\left[-i\left(2p+l+1\right)\tan^{-1}\left(\frac{z}{z_R}\right) + il\phi\right],\end{aligned} \tag{1.34}$$

where,

$$w(z) = w_0\sqrt{1+\left(\frac{z}{z_R}\right)^2}, \quad R(z) = z\left[1+\left(\frac{z}{z_R}\right)^2\right], \quad \text{and } z_R = \frac{\pi w_0^2}{\lambda}. \tag{1.35}$$

In Eq. (1.34), $\mathcal{E}_0$ is the field amplitude, ϕ is the azimuthal angle, $L_p^{|l|}$ is the generalized Laguerre polynomial, where the indices, l and p are known as the orbital angular momentum (OAM) index and radial index, respectively. In Eq. (1.35), $w(z)$ and $R(z)$ are the beam radius and the radius of curvature of the beam's wavefront at a propagation distance, z, respectively. The parameter, z_R is called the "*Rayleigh*

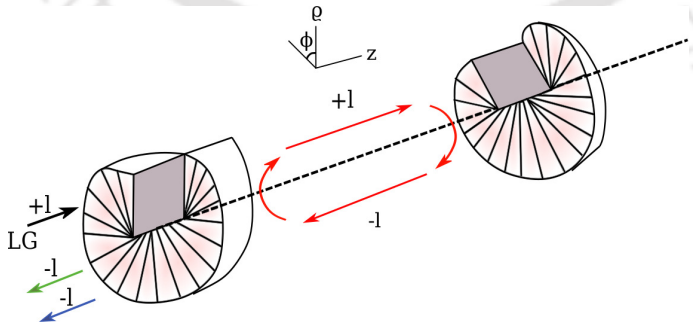

Figure 1.3: Schematic diagram of an optical cavity driven by Laguerre-Gaussian modes. The cavity comprises two spiral phase plates. The colored arrows signify the orbital angular momentum at different positions: The purely extra cavity field, the purely intracavity field and the intracavity field arising from the intracavity field are green, red, and blue arrows, respectively.

length" [59], it is the propagation distance at which $w(z) = \sqrt{2}w_0$, where, $w_0 = w(0)$ is called the beam waist [59].

In Figure 1.3, we depict the paraxial mode propagation inside the helical cavity design using a static double-sided helical mirror and an oscillating helical mirror. We consider an LG beam with orbital angular momentum ($l\hbar$) per photon incident on the static double-sided helical mirror. When the beam reflects off the outer surface of the partially reflective static double-sided helical mirror, it loses $2l\hbar$ amount of angular momentum, as indicated by the green arrow in Figure 1.3. However, its angular momentum remains unchanged when the beam passes through this mirror. Conversely, when the beam reflects off the oscillating rear mirror, it loses $2l\hbar$ angular momentum per photon. Superposition of the two intracavity fields with opposite OAM produces the effective mode function $u(r, \phi, z) = \mathcal{E}_l^p(r, \phi, z) + \mathcal{E}_{-l}^p(r, \phi, z)$. At some specific position (R, z_0) the effective transverse mode becomes $u(\phi) \propto \cos(l\phi)$. Hence, the electric field associated with the intracavity mode can be expressed in the quantized notation as

$$\hat{\mathbf{E}}(\phi) = \mathbf{e}\sqrt{\frac{\hbar\omega_c}{\epsilon_0 V}}\left(a + a^\dagger\right)\cos(l\phi). \tag{1.36}$$

1.4 The Jaynes-Cummings model

This subsection will review the basic concepts of a single atom interacting with a quantized paraxial electric field inside a cavity [60]. Here we consider the atom consists of two states, ground state $|g\rangle$ and an excited state $|e\rangle$. The atom-field interaction Hamiltonian is

$$H^I = -\hat{\mathbf{d}}.\hat{\mathbf{E}} \tag{1.37a}$$

$$= \hat{d}\, G(\phi)\left(a + a^\dagger\right), \tag{1.37b}$$

where $\hat{\mathbf{d}}$ is the atom's dipole moment operator, defined as $\hat{d} = \hat{\mathbf{d}}.\mathbf{e}$, the quantized electric field inside the cavity is $\hat{\mathbf{E}}$, and $G(\phi) = -\sqrt{\hbar\omega_c/(\epsilon_0 V)}\cos(l\phi)$. At this point, we introduce atom's raising operator as $\sigma_+ = |e\rangle\langle g|$ and the lowering operator as $\sigma_- = |g\rangle\langle e|$. The population inversion operator $\sigma_z = |e\rangle\langle e| - |g\rangle\langle g|$, satisfies the commutation relation $\sigma_z = [\sigma_+, \sigma_-]$. By the parity selection rule $\langle e|\hat{d}|e\rangle = \langle g|\hat{d}|g\rangle = 0$, we only keep the off-diagonal elements of $\hat{d}$. Under such conditions the dipole operator $\hat{d}$ can be expressed as

$$\hat{d} = d\left(\sigma_- + \sigma_+\right), \tag{1.38}$$

where $\langle e|\hat{d}|g\rangle = \langle g|\hat{d}|e\rangle = d$. Substituting Eq. (1.38) into Eq. (1.37b), the interaction Hamiltonian takes the form

$$H^I = \hbar g(\phi)\left(\sigma_+ + \sigma_-\right) \otimes \left(a + a^\dagger\right). \tag{1.39}$$

The atom field coupling strength $g(\phi) = -d\cos(l\phi)\sqrt{\omega_c/(\varepsilon_0 V\hbar)} = g_0\cos(l\phi)$. The above atom-field interaction Hamiltonian contains four terms. The energy-conserving terms are only $\sigma_+ \otimes a$ and $\sigma_- \otimes a^\dagger$. Keeping only the energy-conserving terms, the total Hamiltonian can be cast into the form of the famous Jaynes-Cummings model [61]

$$H_s = \hbar\omega_c a^\dagger a + \hbar\omega_{eg}|e\rangle\langle e| + \hbar g(\phi)\left(\sigma_+ a + \sigma_- a^\dagger\right), \tag{1.40}$$

where the energy difference between the two levels is ω_{eg}.

1.4.1 Resonator generated optical lattice

This subsection briefly discusses an application of the Jaynes-Cummins model where a single two-level atom interacts with a quantized paraxial electric field in the presence of a cavity driving.The total Hamiltonian describing the system can be cast into the form

$$H_s = \frac{p^2}{2m} + \hbar\omega_{eg}|e\rangle\langle e| + \hbar\omega_c a^\dagger a + \hbar g(\phi)\left(\sigma_+ a + \sigma_- a^\dagger\right) - i\hbar\varepsilon\left(ae^{-i\omega_l t} - a^\dagger e^{i\omega_l t}\right), \tag{1.41}$$

where m and p are the mass and momentum of the atom, respectively, and the last term signifies the optical pumping effect. The drive field amplitude associated with the input power as $\varepsilon = \sqrt{2\kappa P_{in}/(\hbar\omega_c)}$. Now, we reexpress the above Hamiltonian in a rotating frame moving with angular frequency ω_l. In such a rotating frame, the Hamiltonian can be obtained by $H_{rot} = RHR^\dagger + i\hbar(\partial R/\partial t)R^\dagger$ with the unitary operator $R = \exp\left[i\omega_l t(\sigma_+\sigma_- + a^\dagger a)\right]$. The Hamiltonian in the rotating reference frame can be expressed as

$$H_{rot} = \frac{p^2}{2m} - \hbar\Delta_a|e\rangle\langle e| - \hbar\Delta_c a^\dagger a + \hbar g(\phi)\left(\sigma_+ a + \sigma_- a^\dagger\right) - i\hbar\varepsilon(a - a^\dagger), \tag{1.42}$$

where $\Delta_a = \omega_l - \omega_{eg}$ and $\Delta_c = \omega_l - \omega_c$ are the atom-drive and cavity-drive detuning, respectively. Temporal evolution of the expectation values of each operator obeys the following Heisenberg equation of motions

$$\langle\dot{\sigma_-}\rangle = (i\Delta_a - \gamma)\langle\sigma_-\rangle + ig(\phi)\langle\sigma_z a\rangle, \tag{1.43a}$$
$$\langle\dot{\sigma_+}\rangle = -(i\Delta_a + \gamma)\langle\sigma_+\rangle - ig(\phi)\langle\sigma_z a^\dagger\rangle, \tag{1.43b}$$
$$\langle\dot{a}\rangle = (i\Delta_c - \kappa)a - ig(\phi)\langle\sigma_-\rangle + \eta. \tag{1.43c}$$

In this thesis, we only work in low-saturation regime, where the saturation parameter $s = g_0^2/(\Delta_a^2 + \gamma^2) \ll 1$. This situation can easily attainable by choosing large atomic detuning, Δ_a. For low saturation, the expectation value of the population inversion operator $\langle\sigma_z\rangle$ can be approximated by -1 [62] and the atomic raising and lowering operators can be adiabatically eliminated from the cavity field dynamics with their respective steady-state values,

$$\langle\sigma_+\rangle = \frac{ig(\phi)}{i\Delta_a + \gamma}\langle a^\dagger\rangle \tag{1.44a}$$
$$\langle\sigma_-\rangle = \frac{ig(\phi)}{i\Delta_a - \gamma}\langle a\rangle. \tag{1.44b}$$

Substituting Eq. (1.44b) into Eq. (1.43c), we obtain

$$\langle\dot{a}\rangle = \left[i\Delta_c - \kappa - (\Gamma_0 + iU_0)\cos^2(l\phi)\right]\langle a\rangle + \eta, \tag{1.45}$$

where $\Gamma_0 = g_0^2\gamma/(\gamma^2 + \Delta_a^2)$ and $U_0 = g_0^2\Delta_a/(\gamma^2 + \Delta_a^2)$. The physical significance of U_0 can be interpreted as the energy shift of each photon and Γ_o signifies the modification in cavity decay rate due to the atom-photon interaction. Considering the atomic detuning to be much higher than its damping rate, the cavity mode

becomes unmodified and the energy shift per photon (U_0) tends to g_0^2/Δ_a. Thus the single atom-photon interaction process can be described by the Hamiltonian

$$H_{eff} = \frac{\hat{p}^2}{2m} - \hbar\Delta_c a^\dagger a + \hbar U_0 \cos^2(l\phi) a^\dagger a - i\hbar\eta(a - a^\dagger). \tag{1.46}$$

Now, we consider N two-level atoms with moment of inertia I and the angular momentum L, trapped annularly inside a Laguerre-Gaussian cavity. The dynamics of such a system can be described by the second quantized Hamiltonian as

$$H = \int_0^{2\pi} d\phi\ \Psi^\dagger(\phi) \left[\frac{L^2}{2I} + \hbar U_0 \cos^2(l\phi) a^\dagger a\right] \Psi(\phi) - \hbar\Delta_c a^\dagger a - i\hbar\eta(a - a^\dagger). \tag{1.47}$$

In the subsequent chapter of this thesis, we will directly use Eq. (1.47) as the second quantized form of the annularly trapped Bose-Einstein condensate (BEC) inside the cavity.

1.5 Optomechanical interaction

Canonical optomechanics is a field that deals with the interaction between optics and mechanics. This subject examines how the optical field can manipulate mechanical systems at the micro and nanoscale and vice-versa. The term "canonical" refers to the standard quantum and classical mechanics techniques to describe such interactions. The canonical optomechanical system can be modeled as a Fabry-Perot cavity consisting of one fixed partially transmitting mirror and one perfectly reflective movable mirror of frequency ω_m as shown in Figure 1.4. We apply an external laser drive at frequency ω_l to circulate the photons inside the cavity. We consider ω_m to be much smaller than the free spectral range of the cavity ($c/2L$), so the input laser drive excites a single cavity mode of frequency ω_c. During the cavity round trip time $t = 2L/c$, the linear momentum transferred by n circulating photons to the movable mirror is $P = 2n\hbar\omega_c/c$. Hence, the amplitude of the radiation pressure force can be easily estimated as $F = \hbar\omega_c n/L$. Due to the radiation pressure force, the movable mirror oscillates, and the cavity length changes. Thus, the angular frequency of the cavity modifies as $\omega_c(q) = n\pi c/(L+q)$, where q is the displacement of

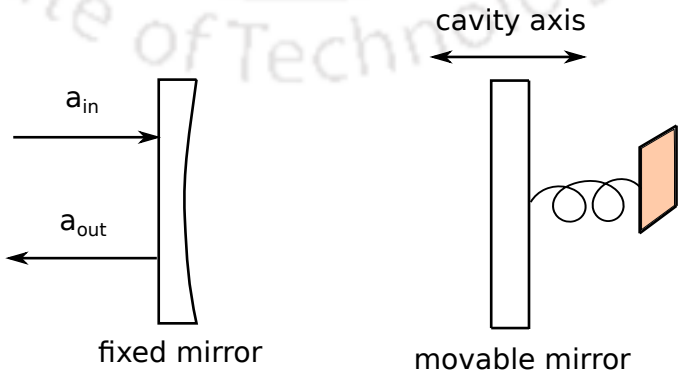

Figure 1.4: Schematic diagram of a Fabry-Perot cavity with one partially transmittive fixed mirror while the movable rear mirror is perfectly reflective.

the movable mirror from the equilibrium position. In the small displacement limit, the cavity resonance frequency $\omega_c(q)$ can be approximated as

$$\omega_c(q) = \omega_c + gq, \tag{1.48}$$

where $\omega_c = n\pi c/L$ and $g = -\omega_c/L$ is the single-photon optomechanical coupling strength between the cavity and the movable mirror. The optomechanical Hamiltonian can be written as

$$H = \hbar\omega_c(q)a^\dagger a + \frac{p^2}{2m} + \frac{1}{2}m\omega_m^2 q^2 + i\hbar\varepsilon(a^\dagger e^{-i\omega_l t} - \text{h.c}), \tag{1.49}$$

where the first term signifies the Hamiltonian corresponding to the single mode cavity field. The annihilation (creation) operator of the cavity mode is denoted by $a(a^\dagger)$. The second and third terms correspond to the kinetic and potential energy of the movable mirror, respectively. The fourth term arises due to the interaction between the cavity field with input drive field. Further, we define the dimensionless position and momentum operators as $Q = q\sqrt{m\omega_m/\hbar}$ and $P = p\sqrt{1/\hbar m\omega_m}$. By substituting Eq. (1.48) into Eq. (1.49), the above Hamiltonian takes the form as

$$H = \hbar\omega_c a^\dagger a + \frac{\hbar\omega_m}{2}(Q^2 + P^2) + \hbar g_0 a^\dagger a Q + i\hbar\varepsilon(a^\dagger e^{-i\omega_l t} - \text{h.c}), \tag{1.50}$$

where the third term represents the optomechanical interaction with the coupling rate $g_0 = g\sqrt{\hbar/m\omega_m}$. We can eliminate the time dependency from the above Hamiltonian by moving to a rotating frame with driving field frequency (ω_l) as

$$H_{rot} = \hbar\Delta_c a^\dagger a + \frac{\hbar\omega_m}{2}(Q^2 + P^2) + \hbar g_0 a^\dagger a Q + i\hbar\varepsilon(a^\dagger - a), \tag{1.51}$$

where the cavity detuning is $\Delta_c = \omega_c - \omega_l$. The time evolution of each operator can be obtained by using the Heisenberg-Langevin equation as

$$\dot{Q} = \omega_m P, \tag{1.52a}$$

$$\dot{P} = -\omega_m Q - g_0 a^\dagger a - \gamma_m P + \xi, \tag{1.52b}$$

$$\dot{a} = -(i\Delta_c + \kappa)a - ig_0 aQ + \varepsilon + \sqrt{2\kappa}a_{in}, \tag{1.52c}$$

where κ is the cavity decay rate that appears due to system-reservoir interaction. To obtain the above equations, we have utilized the commutation relation as $[Q, P] = i$. a_{in} and ξ represent the input vacuum noise operator and the mechanical noise due to the Brownian motion, respectively. The input vacuum noise and the mechanical noise satisfies two-time correlation as

$$\langle a_{in}(t)a_{in}^\dagger(t')\rangle = \delta(t - t'), \langle a_{in}^\dagger(t)a_{in}(t')\rangle = 0, \tag{1.53a}$$

$$\langle \xi(t)\xi(t')\rangle = \frac{\gamma_m}{2\pi\omega_m}\int d\omega\ \omega\ e^{-i\omega(t-t')}\left[1 + \coth\left(\frac{\hbar\omega}{2k_B T}\right)\right], \tag{1.53b}$$

where k_B is the Boltzmann constant and T is the bath temperature of the movable mirror.

1.6 Dynamics of an optomechanical system

In the presence of a strong driving field, we linearize the nonlinear Eq. (1.52a)-(1.52c) by expressing each operator $\mathcal{O}(t)$ as a sum of the steady-state value $\mathcal{O}_s$ and a time-dependent fluctuating value $\delta\mathcal{O}(t)$. The steady-state values of each operator are

$$Q_s = \frac{-g_0|a_s|^2}{\omega_m}, \tag{1.54a}$$

$$P_s = 0, \tag{1.54b}$$

$$a_s = \frac{\varepsilon}{i\Delta_c' + \kappa}, \tag{1.54c}$$

where the effective detuning $\Delta_c' = \Delta_c + g_0 Q_s$. The steady-state photon number ($x = |a_s|^2$) satisfies a cubic equation as

$$\frac{g_0^4}{\omega_m^2}\, x^3 - \frac{2\Delta_c\, g_0^2}{\omega_m}\, x^2 + (\kappa^2 + \Delta_c^2)\, x = \frac{2\kappa P_{in}}{\hbar\omega_c}, \tag{1.55}$$

where P_{in} and ω_c correspond to the input power and the frequency of the input laser drive, respectively. Without the driving field, the only physically admissible solution to the above cubic equation is $x = 0$. One can obtain the critical cavity detuning Δ_{cr} by realizing a single non-zero solution of the above cubic equation where the input power attains an extrema value ($\partial P_{in}/\partial x = 0$). Figure 1.5(a) depicts the bistability response of the intracavity photon number while the cavity detuning is greater than the critical value ($\Delta_{cr} = \sqrt{3}\kappa$). Furthermore, the intra-cavity photon number as a function of cavity detuning for different input drive intensities is shown in Figure 1.5(b). The critical input power is calculated as $P_{cr} = \hbar\omega_i(4\kappa^2\omega_m/3\sqrt{3}g_0^2)$. When the input power is weaker than the critical value, the cavity photon number exhibits a single-valued response as a function of Δ_c. However, when the input power exceeds the critical value, the steady-state photon number becomes multi-valued at a specific cavity range detuning, leading to the bistability response.

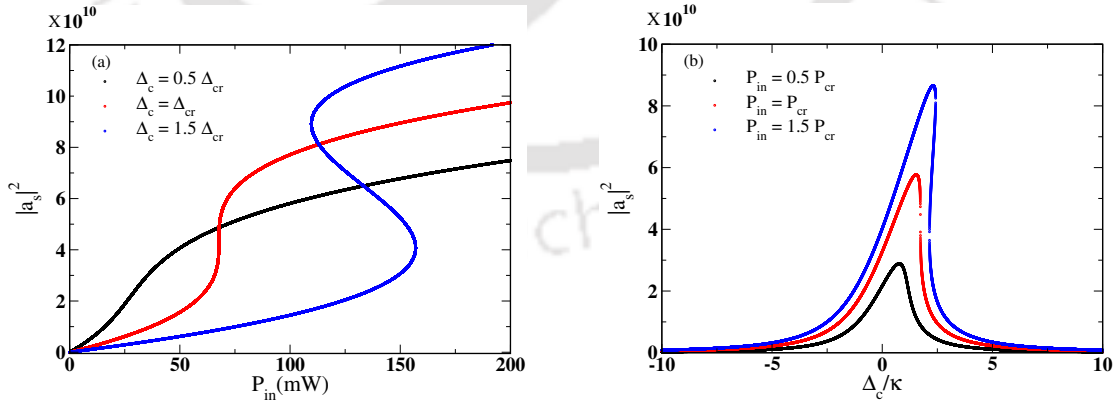

Figure 1.5: Steady-state photon number is shown as a function of (a) input power for three different detuning cases and (b) cavity detuning for three different input powers. The resonance frequency of the movable mirror is $\omega_m/2\pi = 10$ MHz, mass of the mirror is $m = 250$ ng, the damping of the mirror is $\gamma_m/2\pi = 100$ Hz, the cavity decay rate is $\kappa = 0.75\ \omega_m$.

1.6.1 Stability Analysis

The word stability means a small additional perturbation to the solution of a dynamical system that always decays down around a stable and steady state, whereas it enhances exponentially around an unstable steady state solution. In this subsection, we determine the stability conditions of an optomechanical system before obtaining a formal solution of Eq. (1.52a)-(1.52c). The bosonic operator of the acoustic mode is related to the normalized position and momentum operator as $Q = (b + b^\dagger)/\sqrt{2}$ and $P = (b - b^\dagger)/i\sqrt{2}$. With the above definitions, Eq. (1.52a)-(1.52c) can be expressed as

$$\dot{u}(t) = Fu(t) + v(t), \tag{1.56}$$

where $u(t) = (\delta a, \delta a^\dagger, \delta b, \delta b^\dagger)^T$ is the fluctuation vector and the vector of noise operator is $v(t) = (\sqrt{2\kappa}\delta a_{in}, \sqrt{2\kappa}\delta a_{in}^\dagger, f_{in}, f_{in}^\dagger)^T$. The coefficient matrix F governs the evolution of the state vector is

$$F = -\begin{pmatrix} \kappa + i\Delta_c & 0 & -iG & -iG \\ 0 & \kappa - i\Delta_c & iG & iG \\ -iG & -iG & \gamma_m/2 + i\omega_m & 0 \\ iG & iG & 0 & \gamma_m/2 - i\omega_m \end{pmatrix}, \tag{1.57}$$

where the enhanced optomechanical interaction is $G = g_0|a_s|/\sqrt{2}$. The stability of the solutions of Eq. (1.56) requires all the eigenvalues to have a negative real part. The polynomial equation of the eigenvalues of the drift matrix F determines the stability condition by utilizing the Routh-Hurwitz criterion. The determinant of $(F - \lambda\mathbb{1})$ reads

$$\mathrm{Det}(F - \lambda\mathbb{1}) = \lambda^4 + h_1\lambda^3 + h_2\lambda^2 + h_3\lambda + h_4, \tag{1.58}$$

where

$$h_1 = \gamma_m + 2\kappa, \tag{1.59a}$$

$$h_2 = \frac{\gamma_m^2}{4} + \Delta_c^2 + 2\gamma_m\kappa + \kappa^2 + \omega_m^2, \tag{1.59b}$$

$$h_3 = \gamma_m\Delta_c^2 + \frac{1}{2}\gamma_m^2\kappa + \gamma_m\kappa^2 + 2\kappa\omega_m^2, \tag{1.59c}$$

$$h_4 = \frac{1}{4}\gamma_m^2\Delta_c^2 + \frac{1}{4}\gamma_m^2\kappa^2 - 4G^2\Delta_c\omega_m + \Delta_c^2\omega_m^2 + \kappa^2\omega_m^2. \tag{1.59d}$$

Routh-Hurwitz criterion suggests all the eigenvalues of F have a negative real part when
(i) All the h_i's are positive.
(ii) The determinants of all the Hurwitz matrices $|H_i|$ are positive, where the Hurwitz matices are defined as

$$H_1 = h_1, H_2 = \begin{pmatrix} h_1 & h_3 \\ 1 & h_2 \end{pmatrix}, \text{ and } H_3 = \begin{pmatrix} h_1 & h_3 & 0 \\ 1 & h_2 & h_4 \\ 0 & h_1 & h_3 \end{pmatrix}. \tag{1.60}$$

Utilizing the coefficients of Eq. (1.59a)-(1.59d), we find

$$4G^2\Delta_c\omega_m < \left(\Delta_c^2 + \kappa^2\right)\left(\frac{1}{4}\gamma_m^2 + \omega_m^2\right), \tag{1.61a}$$

$$4G^2\Delta_c(\gamma_m+2\kappa)^2\omega_m > -\frac{\gamma_m\kappa}{8}\left(4\Delta_c^2+(\gamma_m+2\kappa)^2\right)^2 - 2\gamma_m\kappa\omega_m^2 - 2\gamma_m\kappa\omega_m^4. \quad (1.61b)$$

Satisfying the above two conditions of effective optomechanical coupling keeps the complete system in a stable region. From the above two conditions, it is evident that if the cavity is red-detuned ($\Delta_c > 0$) to the drive frequency, Eq. (1.61a) provides an upper bound on the intensity of the laser driving. Contrary to that, if the cavity is blue-detuned to the external driving field ($\Delta_c < 0$), the maximum permissible drive field intensity is determined by Eq. (1.61b). From Figure 1.6, we observe when $\Delta_c > 0$, the composite system lies in a stable region for sufficiently large values of effective optomechanical coupling strength. Whereas for $\Delta_c < 0$, one may need to work with meager effective coupling strength $|G|$ to ensure the system's stability.

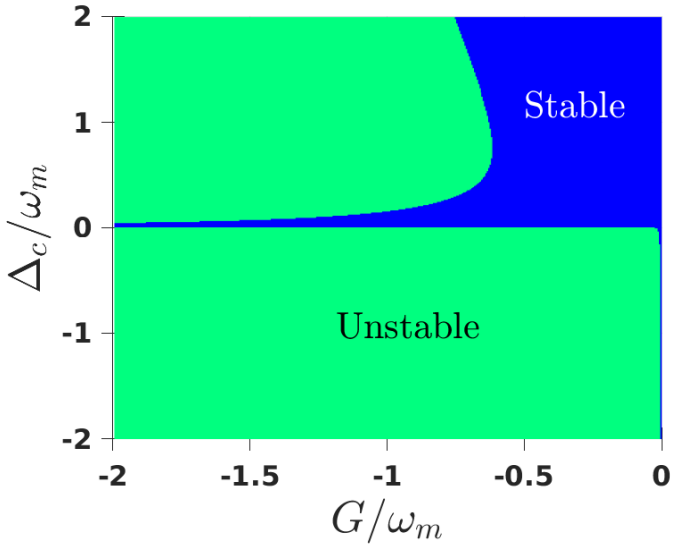

Figure 1.6: The stable and unstable regions are determined as functions of the normalized effective optomechanical coupling G/ω_m and the normalized detuning Δ_c/ω_m. All the other parameters are same as in Figure 1.5.

1.7 Optomechanical cooling

In the last decade, researchers demonstrated the mechanical mirror's cooling in the resolved sideband limit where the mirror's resonance frequency exceeds the cavity decay rate [29, 63–65]. Recently, studies have followed to integrate optomechanical systems with other quantum technologies, such as superconducting circuits, trapped atoms, and solid-state qubits. Hence, cooling is necessary to observe macroscopic quantum phenomena in such hybrid optomechanical systems to reduce the quantum fluctuation of the movable mirror. Before presenting the formulation of resolved sideband cooling, we discuss briefly the physical phenomenon underneath it.

The radiation pressure interaction between the strong control field of frequency ω_l and the movable mirror of frequency ω_m creates the Stokes sideband with frequency $\omega_l + \omega_m$ and anti-Stokes sideband with frequency $\omega_l - \omega_m$ inside the cavity. Between them, only the Stokes field survives when the cavity field frequency exceeds

the drive frequency by ω_m. In other words, during the Stokes process, a quantum of energy $\hbar\omega_m$ is released from the movable mirror and associated with the drive field to form the intracavity photon of frequency $\omega_l + \omega_m$. Hence, the mechanical excitation decreases, and the cooling phenomenon occurs. Here we follow the covariance approach and calculate effective phonon number to demonstrate the cooling effect due to the radiation pressure interaction. To obtain the effective phonon number, we express Eq. (1.56) as

$$\dot{w}(t) = Aw(t) + n(t) \ , \tag{1.62}$$

where the fluctuation vector is $w(t) = (\delta Q(t), \delta P(t), \delta X(t), \delta Y(t))^T$, the input noise operator is $n(t) = (0, \xi, \sqrt{2\kappa}\delta X_{in}, \sqrt{2\kappa}\delta Y_{in})^T$ and the coefficient matrix is

$$A = -\begin{pmatrix} 0 & \omega_m & 0 & 0 \\ -\omega_m & -\gamma_m & -2G & 0 \\ 0 & 0 & -\kappa & \Delta_c \\ -2G & 0 & -\Delta_c & -\kappa \end{pmatrix}. \tag{1.63}$$

We have defined the cavity field amplitude and phase quadratures as $\delta X = (\delta a + \delta a^\dagger)/\sqrt{2}$ and $\delta Y = (\delta a - \delta a^\dagger)/i\sqrt{2}$, respectively and the quadrature of the input noise operators are $\delta X_{in} = (\delta a_{in} + \delta a_{in}^\dagger)/\sqrt{2}$ and $\delta Y_{in} = (\delta a_{in} - \delta a_{in}^\dagger)/i\sqrt{2}$. The formal solution to the Eq. (1.62) is $w(t) = M(t)w(0) + \int_0^t dsM(s)n(t-s)$, where $M(t) = \exp\{At\}$. The elements of the covariance matrix V can be written as

$$\begin{aligned} V_{ij} &= \frac{1}{2}\langle w_i(\infty)w_j(\infty) + w_j(\infty)w_i(\infty)\rangle, \\ &= \sum_{kl}\int_0^\infty ds \int_0^\infty ds' M_{ik}(s)M_{jl}(s')\Phi_{kl}(s-s'), \end{aligned} \tag{1.64}$$

where $\Phi_{kl}(s-s') = \langle n_k(s)n_l(s') + n_l(s')n_k(s)\rangle/2$ is the matrix of the noise correlation function. By utilizing the delta correlation function of the input noises Eq. (1.53a), one can get $\Phi_{kl}(s-s') = D_{kl}\delta(s-s')$, where $D = \text{diag}\,[0, \gamma_m(2n_m+1), \kappa, \kappa]$ and thermal excitation of the movable mirror $n_m = (\exp\{\hbar\omega_m/k_BT\} - 1)^{-1}$. Under the stable condition, the covariance matrix V satisfies the Lyapunov equation

$$AV + VA^T = -D. \tag{1.65}$$

From the above formalism, we obtain the energy of the movable mirror and the effective phonon number from the relation

$$\begin{aligned} U &= \frac{\hbar\omega_m}{2}[\langle\delta Q^2\rangle + \langle\delta P^2\rangle] = \frac{\hbar\omega_m}{2}(V_{11} + V_{22}), \\ &= \frac{\hbar\omega_m}{2}\left(n_{eff} + \frac{1}{2}\right). \end{aligned} \tag{1.66}$$

Figure 1.7, suggests that for $\Delta' \approx \omega_m$ and the input power $P_{in} = 25$ mW, the effective phonon number is reduced to $n_{eff} = 1.135$ that corresponds to the effective temperature of the acoustic mode $T_{eff} = \hbar\omega_m/\left(2k_B \ln\left(1 + (1/n_{eff})\right)\right) \approx 0.37$ mK.

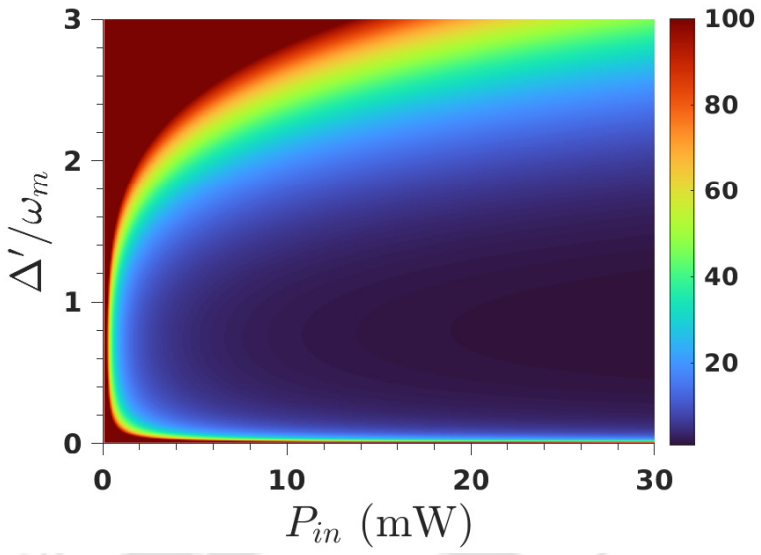

Figure 1.7: The effective phonon number as a function of the optical field intensity and the normalized cavity detuning. The cavity length is $L = 1$ mm, mass of the movable mirror is $m = 250$ ng and the environmental temperature of the mirror is $T = 2$ K. All the other parameters are same as in Figure 1.6.

1.8 Optomechanical Entanglement

Over the last decade, several studies have presented entanglement generation between an optical field and a mechanically pliable object. It demonstrates the validity of quantum mechanics in the macroscopic realm and has several applications in information processing [66, 67] and quantum teleportation. Here, we briefly discuss the entanglement generation between the optical and the mechanical modes by identifying the radiation pressure interaction as

$$H_I = \hbar g_0 a^\dagger a Q. \tag{1.67}$$

Rewritting the dimensionless position operator Q in term of the bosonic creation and annihilation operator $Q = (1/\sqrt{2})\left(b + b^\dagger\right)$, we can express the interaction Hamiltonian as

$$H_I = \frac{\hbar g_0}{\sqrt{2}} a^\dagger a \left(b^\dagger + b\right), \tag{1.68}$$

where a and $a^\dagger$ corresponds to the annihilation and creation operator of the cavity mode. Following the linearization technique as described in Section. 1.6 and keeping only the terms that are of second order in fluctuations, the interaction Hamiltonian takes the form

$$H_I' = \hbar G \left(\delta a^\dagger \delta b + \delta a \delta b^\dagger\right) + \hbar G \left(\delta a \delta b + \delta a^\dagger \delta b^\dagger\right), \tag{1.69}$$

where the first term describes the energy exchange between the optical field and the mirror, commonly known as the beam splitter interaction. The second term signifies the creation or destruction of photons or phonons in pairs, widely known as the parametric down-conversion process [68–70].

At this point, we focus on the situation, where the cavity is over-detuned from the drive frequency by ω_m. Under this condition, the interaction Hamiltonian is primarily governed by the beam-splitter interaction, $\delta a^\dagger \delta b + \delta b^\dagger \delta a$. However, the parametric down-conversion process contributes to the Hamiltonian at the order of G/ω_m. It indicates that when the effective optomechanical coupling G is comparable to ω_m, the interaction Hamiltonian significantly involves contributions from both the parametric down-conversion process and the beam-splitter term. The beam-splitter interaction brings the system close to its quantum ground state and reduces thermal fluctuation. Whereas, the parametric down-conversion process produces entanglement between the optical and the mirror mode. Here we quantify the bipartite entanglement between the optical and the mechanical mode by evaluating the logarithmic negativity $\mathcal{E}_\mathcal{N}$ as

$$\mathcal{E}_\mathcal{N} = \max[0, -\ln 2\eta^-] \,, \tag{1.70}$$

where $\eta^- = 2^{-1/2}\left[\Sigma(V) - [\Sigma(V)^2 - 4\det(V)]^{1/2}\right]^{1/2}$, with $\Sigma(V) = \det A + \det B - 2\det C$. Here, V is the covariance matrix of Eq. (1.65)

$$V = \begin{pmatrix} A & C \\ C^T & B \end{pmatrix} \,. \tag{1.71}$$

The 2×2 blocks of the covariance matrix V are represented as A, B and C. The bipartite entanglement exists if $E > 0$ *i.e.,* when $\eta^- < 1/2$. Figure. 1.8(a) sug-

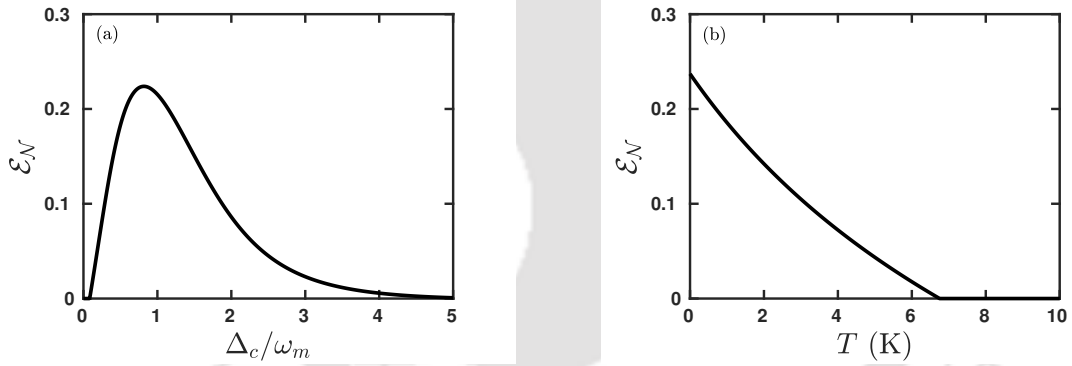

Figure 1.8: The logarithmic negativity is plotted as a function of (a) cavity detuning when the mirror's bath temperature is 0.4 K and (b) the environmental temperature of the movable mirror when $\Delta_c = \omega_m$. We have considered the effective optomechanical coupling strength $G = -0.4\,\omega_m$ for the numerical simulation. All the other parameters are same as in Figure 1.6.

gests that the cavity-mirror entanglement is maximum around $\Delta_c \approx \omega_m$ when the effective optomechanical coupling $|G|$ has a similar order of magnitude with ω_m. In Figure. 1.8(b), the robustness of cavity-mirror entanglement is shown as a function of the movable mirror's environmental temperature.

1.9 The standard quantum limit

Another important aspect of cavity optomechanics is studying the moving mirror's measurement sensitivity [7, 71, 72]. However, the position measurement of the mov-

able mirror is limited due to various noises, *i.e.,* photon shot noise [73], radiation pressure noise [74], and thermal noise. Therefore, one can reduce the measurement imprecision by reducing the collaborative effects of such noises. A systematic demonstration begins with the Heisenberg-Langevin equation of the fluctuating parts of the system's operators as

$$\delta\dot{Q} = \omega_m \delta P, \tag{1.72a}$$

$$\delta\dot{P} = -\omega_m \delta Q - 2G\delta X - \gamma_m \delta P + \xi, \tag{1.72b}$$

$$\delta\dot{X} = -\kappa\delta X + \sqrt{2\kappa}X_{in}, \tag{1.72c}$$

$$\delta\dot{Y} = -\kappa\delta Y - 2G\delta Q + \sqrt{2\kappa}Y_{in}. \tag{1.72d}$$

Here, zero detuning ($\Delta_c = 0$) is considered since the information of the mirror's displacement is imprinted only into the phase quadrature of the cavity field. By Fourier transforming Eq. (1.72a)-(1.72d), one can obtain the cavity field phase quadrature as

$$\delta Y(\omega) = A(\omega)X_{in}(\omega) + B(\omega)Y_{in}(\omega) + C(\omega)\xi(\omega), \tag{1.73}$$

where

$$A(\omega) = -\frac{4\sqrt{2}G^2\sqrt{\kappa}\omega_m}{(\kappa - i\omega)^2\left(i\gamma_m\omega + \omega^2 - {\omega_m}^2\right)}, B(\omega) = \frac{\sqrt{2\kappa}}{\kappa - i\omega}, \text{ and}$$
$$C(\omega) = \frac{2G\omega_m}{(\kappa - i\omega)\left(i\gamma_m\omega + \omega^2 - {\omega_m}^2\right)}. \tag{1.74}$$

The cavity output phase quadrature is related to the corresponding input phase quadrature as

$$\delta Y_{out}(\omega) = \sqrt{2\kappa}\delta Y(\omega) - \delta Y_{in}(\omega). \tag{1.75}$$

The output noise power can be measured by evaluating the power spectral density

$$S_{\delta Y_{out}\delta Y_{out}}(\omega) = \frac{1}{2\pi}\int_{-\infty}^{\infty} d\omega' \langle \delta Y_{out}(\omega')\delta Y_{out}(\omega)\rangle. \tag{1.76}$$

$$= \frac{\omega^2\left(\kappa^2+\omega^2\right)^2\left(\gamma_m^2+\omega^2\right) + \left(\kappa^2+\omega^2\right)^2\omega_m^4 - 2\omega^2\left(\kappa^2+\omega^2\right)^2\omega_m^2}{2\left(\kappa^2+\omega^2\right)^2\left(\omega^2\gamma_m^2 + \left(\omega^2-\omega_m^2\right)^2\right)}$$
$$+ \frac{8G^2\kappa\omega\gamma_m\omega_m \coth\left(\frac{\hbar\omega}{2k_BT}\right)}{\left(\kappa^2+\omega^2\right)\left(\omega^2\gamma_m^2 + \left(\omega^2-\omega_m^2\right)^2\right)} + \frac{32G^4\kappa^2\omega_m^2}{\left(\kappa^2+\omega^2\right)^2\left(\omega^2\gamma_m^2 + \left(\omega^2-\omega_m^2\right)^2\right)}. \tag{1.77}$$

The first, second, and last terms of Eq. (1.77) correspond to shot, thermal, and radiation pressure noise, respectively. To obtain the above noise spectral density, we have utilized the frequency space correlation functions of the optical and the mechanical noises as

$$\langle \delta X_{in}(\omega')\delta X_{in}(\omega)\rangle = \langle \delta Y_{in}(\omega')\delta Y_{in}(\omega)\rangle = \pi\delta(\omega' + \omega)\ ,$$
$$\langle \delta X_{in}(\omega')\delta Y_{in}(\omega)\rangle = -\langle \delta Y_{in}(\omega')\delta X_{in}(\omega)\rangle = i\pi\delta(\omega' + \omega)\ ,$$

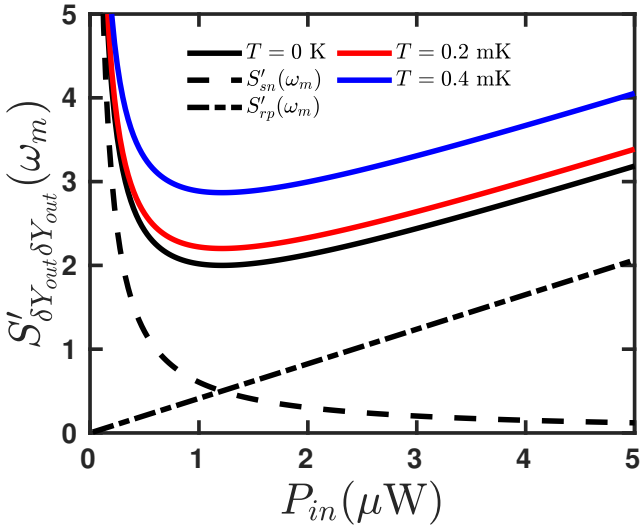

Figure 1.9: Power spectral density for different bath temperatures is shown. The cavity's length and resonance frequency are $L = 1$ mm and $\omega_c/2\pi = 10^{15}$ Hz. All the other parameters are the same as in Figure 1.6. With all these parameters, the optimal power is $P_{in} = 1.2$ μW.

$$\langle \xi(\omega^{'})\xi(\omega)\rangle = 2\pi\frac{\gamma_m\omega^{'}}{\omega_m}\left[1 + \coth\left(\frac{\hbar\omega^{'}}{2k_BT}\right)\right]\delta(\omega^{'} + \omega)\ . \tag{1.78}$$

Further, the noise spectral density $S_{\delta Y_{out}\delta Y_{out}}$ is rescaled by multiplying $\gamma_m(\kappa^2 + \omega^2)/8\kappa G^2$ to make the thermal fluctuation independent of the input power. With the above description, the rescaled photon shot noise and radiation pressure noise at the mechanical resonance frequency are denoted as

$$\begin{aligned} S_{sn}(\omega_m) &= \frac{\gamma_m(\kappa^2 + \omega_m^2)}{16G^2\kappa}, \\ S_{rp}(\omega_m) &= \frac{4G^2\kappa}{\gamma_m(\kappa^2 + \omega_m^2)}. \end{aligned} \tag{1.79}$$

The characteristic behavior of photon shot noise is that it decreases with increasing drive field intensity, while radiation pressure noise increases with increasing drive field intensity. They satisfy the relationship $S_{sn}(\omega_m)S_{rp}(\omega_m) = 1/4$, which is the lower bound of the Heisenberg uncertainty principle. In Figure 1.9, the black, red, and blue solid curves present the noise spectral density at 0 K, 0.2 mK, and 0.4 mK, respectively. The dashed curve depicts the inversely proportional behavior of shot noise with increasing drive power, whereas the radiation pressure or back action noise is proportional to the field intensity. A trade-off between these two noises produces a minimal noise spectral density at $P_{in} = m\omega_m\gamma_m L^2(\kappa^2 + \omega_m^2)/8\omega_c$.

1.10 Optomechanically induced transparency

This section discusses a different idea of power transmission, first discovered in 1991 by Harris *et al.* [75], where they observed a unique transparent response of an otherwise opaque atomic ensemble. This phenomenon is known as Electromagnetically

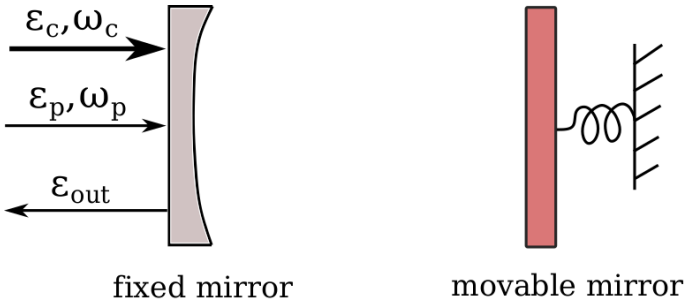

Figure 1.10: Schematic diagram of an optomechanical system. A red-detuned strong coupling field of frequency ω_c and a weak probe field of frequency ω_p are applied. The output field is denoted by ε_{out}.

induced transparency (EIT) [76], where the absorption of the probe beam gets canceled in the presence of a strong coupling field. The sharp hole in the absorption spectrum arises due to the destructive interference of two or more excitation pathways. In cold atomic ensembles, this phenomenon leads to other phenomena like optical pulse storage to slow down light pulses [77–80]. An analogous phenomenon also occurs in an optomechanical system operating in the resolved sideband region ($\omega_m \gg \kappa$), known as Optomechanically Induced Transparency (OMIT). The destructive interference of excitation pathways for the intracavity probe field gives rise to a transparency window when the two-photon resonance condition is satisfied. Like EIT in atomic systems, OMIT also provides an approach to slow down and store light pulses in optomechanical systems [33, 81] with long-lived mechanical excitations. To physically understand the OMIT process, we consider the interaction of a strong coupling field (ω_l) with a mechanical mirror (ω_m). The energy exchange between them produces the Stokes sideband ($\omega_l + \omega_m$) and anti-Stokes sideband ($\omega_l - \omega_m$). Introducing cavity detuning can create an imbalance between them. Moreover, the cavity contains only the Stokes sideband if it is overly detuned to the high-intensity control field by a mechanical resonance frequency. Now a weak probe field (ω_p), which is degenerate with the Stoke field frequency ($\omega_l + \omega_m$) transmits through the system without absorption.

We consider a basic optomechanical system consists of two mirrors as shown in Figure 1.10. Among them, the left one is fixed while the right one is harmonically bound. The cavity annihilation and creation operators a and $a^\dagger$ are satisfying the bosonic commutation relation $[a, a^\dagger] = 1$ and the dimensionless position and momentum of the nanomechanical oscillator satisfies $[Q, P] = i$. In the presence of an additional weak optical drive field, the Hamiltonian of the system is

$$H = \hbar\omega_c a^\dagger a + \frac{\hbar\omega_m}{2}(Q^2 + P^2) + \hbar g_0 a^\dagger a Q + i\hbar\varepsilon_c(a^\dagger e^{-i\omega_l t} - \text{h.c}) + i\hbar(a^\dagger \varepsilon_p e^{-i\omega_p t} - \text{h.c}), \tag{1.80}$$

where the significance of the first four terms has been discussed in Section 1.5. The last term arises due to the cavity-probe field interaction. Moving to the reference frame with the control field frequency, the above Hamiltonian takes the form

$$H_{rot} = \hbar\Delta_c a^\dagger a + \frac{\hbar\omega_m}{2}(Q^2 + P^2) + \hbar g_0 a^\dagger a Q + i\hbar\varepsilon_c(a^\dagger - a) + i\hbar(a^\dagger \varepsilon_p e^{-i\delta t} - \text{h.c}), \tag{1.81}$$

where the cavity detuning is $\Delta_c = \omega_c - \omega_l$ and the probe detuning is $\delta = \omega_p - \omega_l$. To study EIT in the output spectra, one has to deal with the mean response of the system. The mean value equations can be obtained from H_{rot} and also by adding the damping terms. The temporal evolution of the mean values corresponding to each operators can be obtained from a set of coupled differential equation

$$\langle \dot{Q} \rangle = \omega_m \langle P \rangle, \tag{1.82a}$$

$$\langle \dot{P} \rangle = -\omega_m \langle Q \rangle - g_0 \langle a^\dagger \rangle \langle a \rangle - \gamma_m \langle P \rangle, \tag{1.82b}$$

$$\langle \dot{a} \rangle = -\left(\kappa + i\left(\Delta_c + g_0 \langle Q \rangle\right)\right) \langle a \rangle + \varepsilon_c + \varepsilon_p e^{-i\delta t}. \tag{1.82c}$$

We solve the dynamical equations of Eq. (1.82a)-(1.82c) by invoking Runge-Kutta fourth order with initial values $Q(t=0) = 0$, $P(t=0) = 0$, and $a(t=0) = 0$. The Fourier transformation of $a(t)$ offers significant insights into the different components of the intracavity field.

From Figure 1.11(a), it is evident that the intracavity field has only the frequency components ω_l, ω_p, and $2\omega_l - \omega_p$. Under the two-photon resonance condition ($\Delta_c = \delta$), the cavity-generated Stokes and anti-Stokes field amplitude is weak compared to the strong drive field frequency, as shown in the black solid curve. The red and blue curves suggest that leveraging the two-photon resonance conditions can vastly enhance the Stokes field amplitude once the system reaches a stable steady-state value as illustrated in the inset of Figure 1.11(a). Thus in the intense pump field limit, the solution of Eq. (1.82a)-(1.82c) have the form

$$\langle A \rangle = \sum_{n=-1}^{+1} e^{-in\delta t} \langle A \rangle_n. \tag{1.83}$$

However, when the probe field is no longer weak, the nonlinear radiation pressure interaction generates numerous higher-order harmonics in the intracavity field and the truncation of the above ansatz up to $n = 1$ may not be valid anymore. After substituting Eq. (1.83) into Eq. (1.82a)-(1.82c) and ignoring second-order terms,

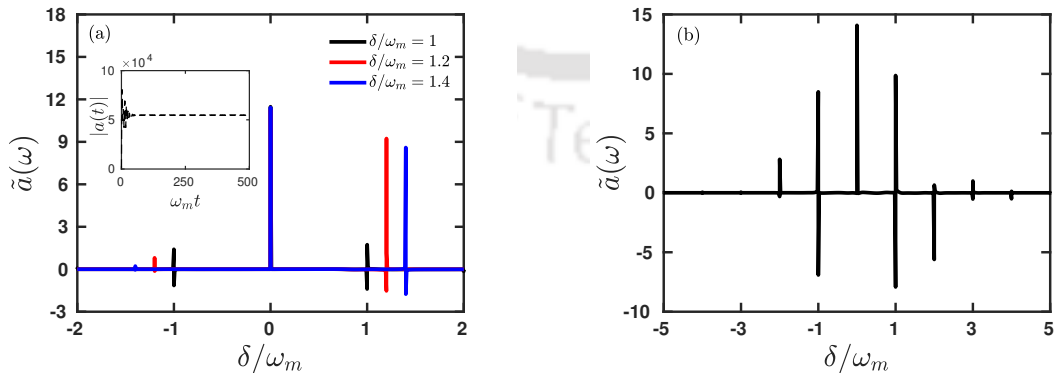

Figure 1.11: Various components of the intracavity field is shown as a function of probe detuning when (a) $P_c/P_p = 100$, and (b) $P_c/P_p = 2.04$. The wavelength of coupling laser $\lambda = 2\pi c/\omega_c = 1064$ nm, $L = 25$ mm, $m = 145$ ng, $\kappa = 2\pi \times 215$ KHz, $\omega_m = 2\pi \times 947$ KHz, $\gamma_m = 2\pi \times 141$ Hz, the cavity detuning is $\Delta_c = \omega_m$ and coupling laser power $P_c = 6.9$ mW.

we obtain

$$\langle a_{+1}\rangle = \frac{i\varepsilon_p\left(\delta\left(\delta+i\gamma_m\right)\left(\Delta_c+\delta+i\kappa\right)-\omega_m^2\left(\Delta_c+\delta+i\kappa\right)+G^2\omega_m\right)}{-2G^2\Delta_c\omega_m+\delta\left(\delta+i\gamma_m\right)\left((\delta+i\kappa)^2-\Delta_c^2\right)+\omega_m^2\left(\Delta_c^2-(\delta+i\kappa)^2\right)}, \quad (1.84)$$

where the effective optomechanical coupling $G = g_0|a_s|$ is treated as phase-independent by introducing an external phase to the input coupling field. The output fields having frequencies the same as the incident probe field is associated with $\langle a_{+1}\rangle$. The output field with frequency ω_p can be obtained by using the input-output relation

$$\varepsilon_{out}(t) + \varepsilon_p e^{-i\delta t} + \varepsilon_c = 2\kappa\langle a\rangle.$$

By considering the terms having only frequency component ω_p, we obtain

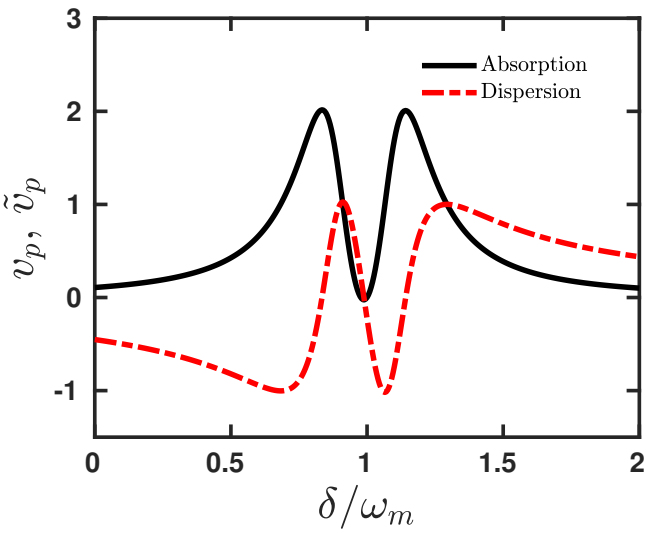

Figure 1.12: Absorption and dispersion spectrum is shown with respect to δ. All the other parameters are same as in Figure 1.11(a).

$$\varepsilon_{out} + \varepsilon_p e^{-i\delta t} = 2\kappa\langle a_{+1}\rangle e^{-i\delta t} = \varepsilon_t \varepsilon_p e^{-i\delta t}. \quad (1.85)$$

The quadratures of the field $\varepsilon_t = v_p + i\tilde{v}_p$, show the absorptive and dispersive behaviour as a function of the probe detuning as potrayed in Figure 1.12. The black solid curve shows the absorption is suppressed within a narrow frequency range near the two photon resonance condition ($\delta = \omega_m$) and the system's dispersive response is anomalous. Hence, the intense coupling field modulates the dispersive response of a system, which subsequently alters the group velocity of an optical pulse within the transparent medium. A light pulse is made up of a superposition of waves with different frequencies. In a vacuum, all frequency components travel at a constant speed of $c = 3 \times 10^8\ m/s$. Consequently, the superposition of these components also moves at this same speed, c. However, in a dispersive medium, each frequency travels at a different speed, which leads to a different envelope velocity for the optical pulse, commonly known as the "group velocity" of the optical signal. In this thesis, we will discuss further the "group delay" and "time delay" of a weak probe pulse in the subsequent chapters.

1.11 Cavity magnomechanics

Similar to phonons, which are quanta of vibrational energy, magnons are quanta of elementary magnetic excitations or spin waves in a magnetic material. In contrast to cavity optomechanics, where the single photon radiation pressure coupling is of the order of Hertz ($g_0/\kappa \approx 2\times10^{-5}$), the high spin density in ferrimagnetic insulators allows for single photon-magnon coupling at gigahertz frequencies ($g_{ma}/\kappa > 1$) [40,82]. To understand the dynamics of such system, we consider the interaction between the

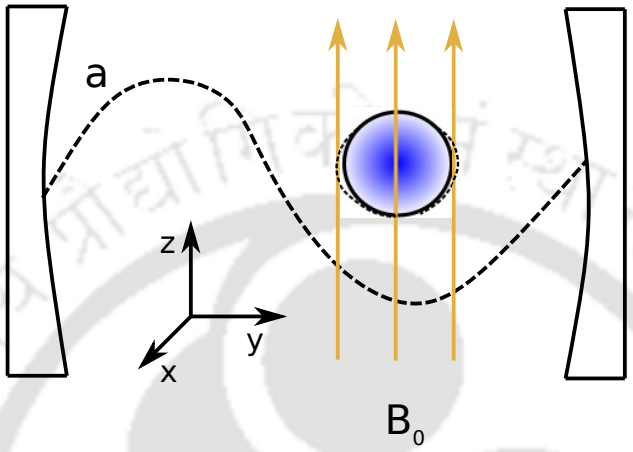

Figure 1.13: Schematic of yttrium iron garnet (YIG) sphere interacting with a cavity mode a. The bias magnetic field along z-direction activates the magnon mode of the YIG sphere.

macroscopic ferrimagnetic yttrium iron garnet sphere and the external microwave field along the x-axis. The interaction Hamiltonian can be written as

$$\begin{aligned} H_1 =& -\mu_x B_x, \\ =& -M_x V B_{vac}(a + a^\dagger), \end{aligned} \tag{1.86}$$

where B_{vac} is the microwave field amplitude of the cavity mode at a single photon level, and μ_x, M_x are the magnetic moment and the magnetization of the YIG sphere along the x-axis, respectively. The magnetization of the YIG sphere (M_x) can be represented in terms of the magnetization with a large spin S_x by the relation $M_x = \gamma_e S_x/V$, where V is the volume of the YIG sphere and γ_e is the gyromagnetic ratio of the electron spin ($\gamma_e = e/m_e c$). Moreover, in the high spin density limit, the Holstein-Primakoff transformation reads

$$\begin{aligned} S^+ =& S_x + iS_y = \sqrt{2S}\, m, \\ S^- =& S_x - iS_y = \sqrt{2S}\, m^\dagger, \end{aligned} \tag{1.87}$$

where S is the total spin of the magnetized YIG sphere. The m and $m^\dagger$ operators satisfy the Bosonic commutation relation ($[m, m^\dagger] = 1$). Further substituting Eq. (1.87) into Eq. (1.86), we obtain

$$H_1 = -\gamma_e B_{vac}\sqrt{\frac{S}{2}}(m + m^\dagger)(a + a^\dagger). \tag{1.88}$$

When both the cavity field and the magnon mode have close resonance frequency, under the rotating wave approximation, the interaction energy reads

$$H_1 \approx -\gamma_e B_{vac}\sqrt{\frac{S}{2}}(m^\dagger a + m a^\dagger). \tag{1.89}$$

and $g_{ma} = -\gamma_e B_{vac}\sqrt{S/2}$ represents the magnon-photon coupling strength.
Now, we discuss another interaction that arises due to the deformation of the magnetic material. In the presence of an external magnetic field the magnetostrictive energy density can be quantified as

$$E_{me} = \frac{B_1}{M_s^2}\left(M_x^2\epsilon_{xx} + M_y^2\epsilon_{yy} + M_z^2\epsilon_{zz}\right) + \frac{B_2}{M_s^2}\left(M_x M_y\epsilon_{xy} + M_x M_z\epsilon_{xz} + M_y M_z\epsilon_{yz}\right), \tag{1.90}$$

where B_1 and B_2 are the magnetoelastic coupling coefficients, $M_{x,y,z}$ are the magnetization components along x, y, z-directions. The energy strain tensor of the magnetic material

$$\epsilon_{ij} = \frac{1}{2}\left(\frac{\partial u_i}{\partial x_j} + \frac{\partial u_j}{\partial x_i}\right), \tag{1.91}$$

where u is the displacement. The Holstein-Primakoff transformation reads

$$M_x = \sqrt{\frac{\hbar\gamma M_s}{2V}}(m + m^\dagger), \tag{1.92a}$$

$$M_y = i\sqrt{\frac{\hbar\gamma M_s}{2V}}(m - m^\dagger), \tag{1.92b}$$

$$M_z = \left(M_s^2 - M_x^2 - M_y^2\right)^{1/2} \approx M_s - \frac{\hbar\gamma}{V}m^\dagger m. \tag{1.92c}$$

By substituting Eq. (1.92a)-(1.92c) in the first part of Eq. (1.90) and integrating it, we obtain the total magnetostrictive energy as

$$\begin{aligned}\mathbf{E}_1 =& \frac{B_1\hbar\gamma}{M_s V}m^\dagger m\int dl^3(\epsilon_{xx} + \epsilon_{yy} - 2\epsilon_{zz}) + \frac{B_1\hbar\gamma}{2M_s V}(m^2 + m^{\dagger 2})\int dl^3(\epsilon_{xx} - \epsilon_{yy}) \\ &+ \frac{B_1\hbar^2\gamma^2}{M_s^2 V^2}m^\dagger m m^\dagger m\int dl^3\epsilon_{zz}.\end{aligned} \tag{1.93}$$

The displacement due to magnetostrictive effect can be written as

$$\vec{u}(x,y,z) = \sum_{n,m,k} d^{(n,m,k)}\vec{\chi}^{(n,m,k)}(x,y,z). \tag{1.94}$$

By using the displacement amplitude $d^{(n,m,k)} = d_{zpm}^{(n,m,k)}(b_{n,m,k} + b_{n,m,k}^\dagger)$ in the first part of Eq. (1.93), the magnon-phonon interaction term brings out as

$$\mathbf{E}_1 \approx \sum_{n,m,k}\hbar g^{(n,m,k)}m^\dagger m(b_{n,m,k} + b_{n,m,k}^\dagger). \tag{1.95}$$

1.12 Outline of the Thesis

We present the outline of the thesis. The thesis comprises five chapters, including the introduction and the future plans. Here, we briefly describe the problems that have been investigated in the thesis and have been presented later on in Chapter 2, Chapter 3, and Chapter 4.

Chapter 2: In this chapter, we will describe the control field phase-dependent response of the output probe field transmission from a red detuned ring cavity resonator. We employ an additional weak mechanical drive to one of the movable mirrors. The system brings out a double transparency peak. The combined effect of the mechanical pump amplitude and the phase of the drive field provides complete control of the intensity and time delay of the output field through one transmission window.

Chapter 3: This chapter discusses our second problem based on the output probe pulse amplification assisted by the superluminal propagation in a cavity magnomechanical system that consists of two evanescently coupled microwave cavities. The lossy cavity interacts with ferrimagnetic yttrium iron garnet, which also shows shape deformation when applied to a biased magnetic field. Our system depicts high absorption under passive configuration. However, replacing the auxiliary passive cavity with an active one produces an effective gain, and an anomalous dispersion occurs under the magnomechanical resonance condition. Consequently, we observe superluminal probe pulse propagation with a 67-fold amplification.

Chapter 4: This chapter introduces a hybrid optomechanical system with an annularly trapped Bose-Einstein condensate inside an optical cavity. The cavity is driven by Lauguerre-Gaussian modes and is made of two spiral phase elements as the end mirrors of the cavity. The rear mirror oscillates torsionally about the cavity axis through a clamped support, making it a rotational analog of standard optomechanics. In this hybrid system, we utilize atomic rotation to correlate the optical amplitude and phase quadratures that provide ponderomotive squeezing *i.e.,* the quantum fluctuations at the mirror's frequency reduces below the shot noise level. We also explore bipartite and tripartite entanglement between the cavity, atomic matter waves, and the macroscopic rotating mirror with experimentally realizable parameters. By tuning the drive field's topological charge and the rotation of the condensate atoms, we reduce the frequency difference between the atomic matter waves and the mirror. Our study predicts a diminishing entanglement between the cavity and the mirror mode when the atomic matter waves degenerate with the mirror.

Chapter 5: In this chapter, we summarise all the results discussed before and concludes them. Finally, we propose some potential avenues to extend our work and offer insights into future prospects.

Chapter 2

Phase-dependent controllable field generation in a ring cavity resonator

2.1 Introduction

The radiation pressure interaction between optics and mechanics opens up promising perspectives in quantum optics and quantum information science. Over the past decade, extensive research has been conducted to explore various aspects of the radiation pressure interaction, including gravitational-wave detection [83], entanglement between two distant mechanical oscillators [84, 85], photon and phonon blockade [86–88]. The conventional optomechanical system has been extended to whispering-gallery-mode resonators [89], optomechanical crystals [90,91], electromechanical circuits [92]. The radiation pressure force mimics numerous physical phenomena associated with the semi-classical behavior of the light-matter interaction. For instance, an optomechanical system shows a mechanical analog of electromagnetically induced transparency (EIT) [93–96]. In EIT, an absorbent atomic medium becomes transparent in the presence of a strong control field. EIT has promising applications such as slow light [97] and light storage [98]. Its mechanical counterpart, known as optomechanically induced transparency (OMIT), has been theoretically predicted [24,99–101] and experimentally observed in both optical cavities [102–104] and microwave cavities [105]. In all these systems, the radiation pressure-induced displacement of the movable mirror plays a crucial role in obtaining a transparency window. However, in quadratically coupled optomechanical systems (OMS), the movable mirror's mean displacement becomes zero. In such a scenario, the fluctuations in the displacement of the movable mirror due to the interaction with the environment produce a narrow spectral window for probe transmission [106–109]. Recent investigations have explored controllable optical output field transmission, as well as absorption in the presence of weak periodic mechanical force [110–116] that produces mechanical coherences. It has been demonstrated that the behavior of the weak mechanical drive's amplitude and phase can be harnessed to achieve a controllable transmission and delay of the optical signal [110–116].

In all the previous studies, the effective optomechanical coupling is considered to be phase-independent by adding a phase to the input field. In this chapter, we present a phase-dependent controllable group delay and the transmission of the

output field in an optomechanical system. To achieve this, we use a phase-dependent strong control field and weak mechanical pump in a double OMIT configuration. For this purpose, a red detuned ring cavity is taken into account. We apply an external mechanical drive of phase ϕ_m to one of the movable mirrors. We find that the interference between the radiation pressure induced cavity fields and the mechanical pump induced sidebands leads to the enhancement of the output fields transmission while the mechanical drive is in phase with the applied probe field. However, a complete control on the output field transmission can be achieved by using the combined effect of the amplitude and the phase properties of the mechanical pump and the control field, respectively. Hence the control field phase ϕ_c invokes an extra tunability on output field transmission. We also exhibit how the probe pulse propagation delay can be changed from slow to fast light by tailoring the phase of the control field. Further, we examine the effect of control phase on Stokes field generation via the four-wave mixing process.

The chapter is organized as follows. In Section. 2.2, the theoretical model for a ring cavity optomechanical system is described. This Section. 2.2 also contains the Heisenberg equation of motion to govern the temporal evolutions of the expectation values of each operator. Section 2.3 discusses the control field phase dependency on the output probe field transmission. Further, the group velocity of the optical probe pulse has been studied analytically and verified numerically in Section 2.3.1. Section 2.4 addresses control field phase-dependent four-wave mixing (FWM) field generation. Section 2.5 contains the conclusion of this work.

2.2 Theoretical model

In the previous literature, the optical output field transmission has been studied thoroughly in a red detuned ring cavity optomechanical system [117] which consists of three mirrors as shown in Figure 2.1. Out of three mirrors, two are movable and perfectly reflecting mirrors, while the last one is fixed and partially transmitting. This cavity is strongly driven by a control field ε_c with frequency ω_c and phase ϕ_c together with a weak probe field ε_p with frequency ω_p and phase ϕ_p. In order to manipulate the transmission and group velocity of the probe pulse, a weak mechanical drive of amplitude ε_m with frequency ω_m and phase ϕ_m is applied to one of the movable mirrors [110]. The coupling between the cavity field and the movable mirrors can be achieved through radiation pressure exerted by the photons in the cavity [118, 119]. In our scheme, we treat the oscillation of the movable mirrors as quantum harmonic oscillators with resonance frequencies ω_i, effective mass m_i, and mechanical damping $\gamma_i (i = 1, 2)$. The damping of the mechanical oscillators arise from the interactions with the environment. We also assume that the mechanical frequencies ω_i are much larger than the cavity decay rate κ in order to produce well resolved sideband regime in OMIT [24, 102].
The total Hamiltonian of the model system can be expressed as

$$\begin{aligned} H = {} & \hbar\omega_0 c^\dagger c + \frac{\hbar\omega_1}{2}\left(Q_1^2 + P_1^2\right) + \frac{\hbar\omega_2}{2}\left(Q_2^2 + P_2^2\right) \\ & + \hbar\left(g_1 Q_1 - g_2 Q_2\right) c^\dagger c \cos\frac{\theta}{2} + i\hbar\varepsilon_c\left(c^\dagger e^{-i\omega_c t - i\phi_c} - \text{h.c}\right) \\ & + i\hbar\left(c^\dagger \varepsilon_p e^{-i\omega_p t - i\phi_p} - \text{h.c}\right) - 2Q_1\varepsilon_m\hbar\cos(\omega_m t + \phi_m), \end{aligned} \tag{2.1}$$

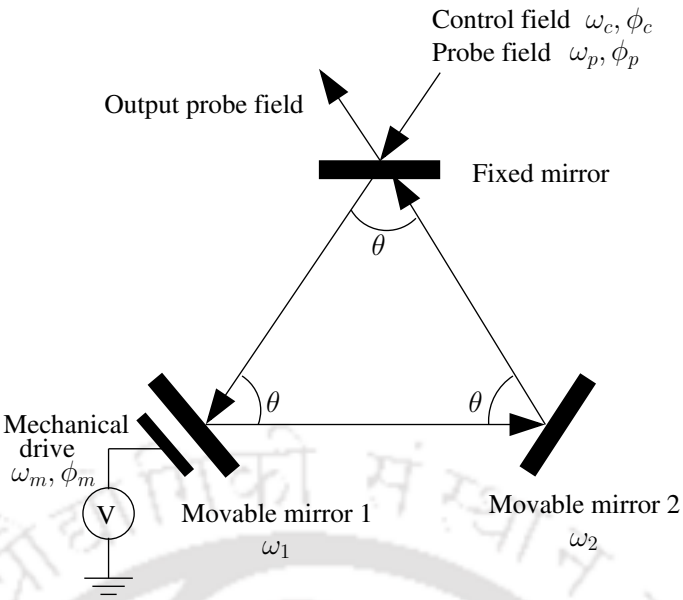

Figure 2.1: Schematic diagram of a ring cavity resonator. A strong coupling field of frequency ω_c and a weak probe field of frequency ω_p are applied along with a weak mechanical drive of frequency ω_m. The two movable mirrors have different resonant frequencies ω_1 and ω_2.

where the first term corresponds to the free Hamiltonian of the single-mode cavity with frequency ω_0. The annihilation (creation) operator of the cavity field is denoted by $c(c^\dagger)$. The second and third term describes the total energy of two nanomechanical oscillators. The fourth term illustrates the radiation pressure interaction between two movable mirrors and the cavity field. We introduced a relative minus sign between two radiation pressure terms which is consistent with the constant total cavity length, and the length between two mechanical mirrors are fixed during the oscillation. The fifth and sixth terms come from the interaction between the cavity field and two input fields. The last term accounts for the external mechanical drive that is applied to one of the movable mirrors. In an electromechanical circuit, the time-dependent voltage source produces a current on the capacitor surface. The Coulomb interaction between these two conducting surface produces the periodic mechanical driving force [120]. The dimensionless position and momentum quadratures of j^{th} nano-mechanical oscillator are defined as $Q_j = q_j\sqrt{m_j\omega_j/\hbar}$ and $P_j = p_j\sqrt{1/m_j\omega_j\hbar}$ with commutation relation, $[Q_j, P_k] = i\delta_{jk}(j,k \in 1,2)$. The amplitude of the control, probe, and the mechanical drive inside the ring cavity is given by $\varepsilon_i = \sqrt{2\kappa P_i/\hbar\omega_i}$, $(i = c, p, m)$ with P_i, being the respective power of fields and κ the cavity decay rate. The Hamiltonian of the system in a rotating frame with respect to the coupling field frequency ω_c is defined by $H_{rot} = RHR^\dagger + i\hbar\left(\partial R/\partial t\right)R^\dagger$, where $R = e^{i\omega_c c^\dagger ct}$. By using Baker-Campbell-Hausdorff formula

$$e^{\alpha A}Be^{-\alpha A} = B + \alpha[A,B] + \frac{\alpha^2}{2!}[A,[A,B]] + ...,$$

H_{rot} can be cast into the following form

$$H_{rot} = \hbar\Delta_c c^\dagger c + \frac{\hbar\omega_1}{2}\left(Q_1^2 + P_1^2\right) + \frac{\hbar\omega_2}{2}\left(Q_2^2 + P_2^2\right)$$

$$+\hbar\left(g_1Q_1-g_2Q_2\right)c^\dagger c\cos\frac{\theta}{2}+i\hbar\varepsilon_c\left(c^\dagger e^{-i\phi_c}-\text{h.c}\right)$$
$$+i\hbar\left(c^\dagger\varepsilon_p e^{-i\delta t-i\phi_p}-\text{h.c}\right)-2Q_1\varepsilon_m\hbar\cos(\omega_m t+\phi_m). \tag{2.2}$$

The detuning $\Delta_c=\omega_0-\omega_c$ and $\delta=\omega_p-\omega_c$. In this study, we treat the control and probe field as classical fields. We use the mean response of the system for investigating the transmitted output. The mean response of the system can be obtained by using the Heisenberg - Langevin equation as $\langle\dot{\mathcal{O}}\rangle=i\langle[H,\mathcal{O}]\rangle/\hbar+\langle N\rangle$, under the rotating frame with frequency ω_c. The N stands for quantum fluctuation. Here we assume white noise as a quantum fluctuation [24,121]. By using Heisenberg - Langevin equation, we obtain a set of coupled differential equations as

$$\langle\dot{c}\rangle=-\left[\kappa+i\left(\Delta_c+\left(g_1\langle Q_1\rangle-g_2\langle Q_2\rangle\right)\cos\frac{\theta}{2}\right)\right]\langle c\rangle+\varepsilon_c e^{-i\phi_c}+\varepsilon_p e^{-i\phi_p}e^{-i\delta t}, \tag{2.3a}$$

$$\langle\ddot{Q}_1\rangle=-\gamma_1\langle\dot{Q}_1\rangle-\omega_1^2\langle Q_1\rangle-\omega_1 g_1\langle c^\dagger\rangle\langle c\rangle\cos\frac{\theta}{2}-2\varepsilon_m\omega_1\cos(\omega_m t+\phi_m), \tag{2.3b}$$

$$\langle\ddot{Q}_2\rangle=-\gamma_2\langle\dot{Q}_2\rangle-\omega_2^2\langle Q_2\rangle+\omega_2 g_2\langle c^\dagger\rangle\langle c\rangle\cos\frac{\theta}{2}. \tag{2.3c}$$

The radiation pressure force as well as the periodic mechanical force produce two sets of optical output fields at frequency $\omega_c\pm m\delta$, and frequency $\omega_c\pm n\omega_m$, respectively. Further, the resonant condition $\omega_m=\delta=\omega_1$ allows these two components of the output field to exhibit interference phenomena depending on the relative phase $\phi=\phi_p-\phi_m$ between the probe field and mechanical drive. In the strong driving field region, the mean values of any operator $\mathcal{O}(t)$ can be expressed as a sum of its steady-state value $\mathcal{O}_s$ and a small fluctuating time-dependent term $\tilde{\mathcal{O}}(t)$. The steady-state values of each operator are

$$Q_{1s}=-\frac{G_1}{\omega_1}c_s^*,\quad Q_{2s}=\frac{G_2}{\omega_2}c_s^*,\quad c_s=\frac{\varepsilon_c e^{-i\phi_c}}{\kappa+i\Delta'}, \tag{2.4}$$

where $G_i=g_i c_s\cos\theta/2$ for $i=1,2$ are the effective optomechanical coupling rates and $\Delta'=\Delta_c+(g_1Q_{1s}-g_2Q_{2s})\cos\theta/2$ is the effective detuning. Time dependent part of Eq. (2.3a)-(2.3c) reads

$$\dot{\tilde{c}}+(\kappa+i\Delta')\,\tilde{c}=-iG_1\tilde{Q}_1+iG_2\tilde{Q}_2+\varepsilon_p e^{-i\delta t}e^{-i\phi_p}, \tag{2.5a}$$

$$\ddot{\tilde{Q}}_1+\gamma_1\dot{\tilde{Q}}_1+\omega_1^2\tilde{Q}_1=-\omega_1G_1\tilde{c}^*-\omega_1G_1^*\tilde{c}-2\varepsilon_m\omega_1\cos(\omega_m t+\phi_m), \tag{2.5b}$$

$$\ddot{\tilde{Q}}_2+\gamma_2\dot{\tilde{Q}}_2+\omega_2^2\tilde{Q}_2=\omega_2G_2\tilde{c}^*+\omega_2G_2^*\tilde{c}. \tag{2.5c}$$

We assume that the control field is much stronger than the probe field and mechanical drive. In this strong control field regime, we have adopted the following ansatz to solve the Eq. (2.5a)-(2.5c)

$$\tilde{c}=\ c_{p+}e^{-i\delta t}+c_{p-}e^{i\delta t}+c_{m+}e^{-i\omega_m t}+c_{m-}e^{i\omega_m t}, \tag{2.6a}$$

$$\tilde{Q}_1=\ Q_{1p}e^{-i\delta t}+Q_{1p}^*e^{i\delta t}+Q_{1m}e^{-i\omega_m t}+Q_{1m}^*e^{i\omega_m t}, \tag{2.6b}$$

$$\tilde{Q}_2=\ Q_{2p}e^{-i\delta t}+Q_{2p}^*e^{i\delta t}+Q_{2m}e^{-i\omega_m t}+Q_{2m}^*e^{i\omega_m t}. \tag{2.6c}$$

We obtain

$$c_{p+}(\delta)=\frac{A(\delta)}{B(\delta)},\quad c_{p-}(\delta)=\frac{F(\delta)}{H(\delta)} \tag{2.7}$$

$$c_{m+}(\omega_m) = \frac{D(\omega_m)}{E(\omega_m)}, \quad c_{m-}(\omega_m) = \frac{I(\omega_m)}{J(\omega_m)}. \tag{2.8}$$

where

$$\begin{aligned}
A(\delta) &= \varepsilon_p e^{-i\phi_p}[-(i(|G_1|^2\omega_1 m_2^{-1}\chi_2^{-1}(\delta) + |G_2|^2\omega_2 m_1^{-1}\chi_1^{-1}(\delta) \\
&\quad - (m_1 m_2 \chi_1(\delta)\chi_2(\delta))^{-1}(\delta + \Delta' + i\kappa)))], \\
B(\delta) &= (((\delta + i\kappa)^2 - \Delta'^2)(m_1 m_2 \chi_1(\delta)\chi_2(\delta))^{-1} \\
&\quad + \omega_1\omega_2(G_2G_1^* - G_1G_2^*)^2 + 2\Delta'(|G_2|^2\omega_2 m_1^{-1}\chi_1^{-1}(\delta) \\
&\quad + |G_1|^2\omega_1 m_2^{-1}\chi_2^{-1}(\delta))), \\
D(\omega_m) &= \omega_1\varepsilon_m e^{-i\phi_m}[-G_1 m_2^{-1}\chi_2^{-1}(\delta)(\Delta' + i\kappa + \omega_m) \\
&\quad + G_2\omega_2(G_1G_2^* - G_2G_1^*)], \\
E(\omega_m) &= -(\Delta'^2 + (\kappa - i\omega_m)^2)(m_1 m_2 \chi_1(\omega_m)\chi_2(\omega_m))^{-1} \\
&\quad + \omega_1\omega_2(G_1G_2^* - G_2G_1^*)^2 + 2\Delta'\omega_1|G_1|^2(m_2\chi_2(\omega_m))^{-1} \\
&\quad + 2\Delta'\omega_2|G_2|^2(m_1\chi_1(\omega_m))^{-1}, \\
F(\delta) &= \varepsilon_p e^{i\phi_p}[\delta(G_1^2\gamma_2\omega_1 + G_2^2\gamma_1\omega_2) + i(G_2^2\omega_2(\delta^2 - \omega_1^2) \\
&\quad + G_1^2\omega_1(\delta^2 - \omega_2^2))], \\
H(\delta) &= -(\delta^2 - (\Delta' - i\kappa)^2)(m_1 m_2 \chi_1^*(\delta)\chi_2^*(\delta))^{-1} \\
&\quad + \omega_1\omega_2(G_2G_1^* - G_1G_2^*)^2 + 2\delta\omega_2|G_2|^2(m_1\chi_1^*(\delta))^{-1} \\
&\quad + 2\delta\omega_1|G_1|^2(m_2\chi_2^*(\delta))^{-1}, \\
I(\omega_m) &= -\varepsilon_m\omega_1 e^{i\phi_m}(G_2^2G_1^*\omega_2 - G_1(|G_2|^2\omega_2 + (\omega_m - \Delta' - i\kappa) \\
&\quad (m_2\chi_2^*(\omega_m))^{-1})), \\
J(\omega_m) &= -(\Delta'^2 + (\kappa + i\omega_m)^2)(m_1 m_2 \chi_1^*(\omega_m)\chi_2^*(\omega_m))^{-1} \\
&\quad - \omega_1\omega_2(G_2G_1^* + G_1G_2^*)^2 + 2\omega_2\Delta'|G_2|^2(m_1\chi_1^*(\omega_m))^{-1} \\
&\quad + 2\omega_1\Delta'|G_1|^2(m_2\chi_2^*(\omega_m))^{-1}.
\end{aligned}$$

Here c_{p+} and c_{p-} are the output fields having frequencies the same as incident probe field and the generated FWM field, respectively. The mechanical pump induces two sidebands whose amplitude are given by c_{m+} and c_{m-}. We introduce $\chi_i(\omega) = [m_i(\omega_i^2 - \omega^2 - i\gamma_i\omega)]^{-1}$ as the mechanical susceptibility of i^{th} oscillator. It is evident from Eq. (2.7) and Eq. (2.8) that the structures of complex poles are greatly influenced by the mechanical susceptibilities ($\chi_i(\omega)$). Therefore, the position and the width of $c_i (i = p_\pm, m_\pm)$ can be controlled by the mechanical susceptibilities of the two movable mirrors. Moreover, the output field from the cavity can be obtained by the cavity input-output relation,

$$\varepsilon_{out} = 2\kappa\langle c\rangle - \varepsilon_c - \varepsilon_p e^{-i\delta t - i\phi_p}. \tag{2.9}$$

By substituting Eq. (2.6a)-(2.6c) into Eq. (2.9), we obtain the normalized amplitude of the output probe field as

$$t_p = \frac{2\kappa c_{p+} - \varepsilon_p e^{-i\phi_p}}{\varepsilon_p e^{-i\phi_p}}. \tag{2.10}$$

Consequently, the transmitted amplitude of output FWM field at frequency $2\omega_c - \omega_p$ can be obtained as

$$t_f = \frac{2\kappa c_{p-}}{\varepsilon_p e^{i\phi_p}}. \tag{2.11}$$

In addition, the mechanical drive can generate the upper sideband $\omega_c+\omega_m$ and lower sideband $\omega_c-\omega_m$ that takes following normalized forms

$$t_u = \frac{2\kappa c_{m+}}{\varepsilon_m e^{-i\phi_m}}, \quad \text{and} \quad t_l = \frac{2\kappa c_{m-}}{\varepsilon_m e^{i\phi_m}}. \tag{2.12}$$

Since we have considered $\omega_m = \omega_1 = \delta$, therefore generated frequency of upper and lower sideband is same as probe frequency ω_p and FWM frequency $2\omega_c - \omega_p$, respectively. Then the output field amplitude oscillating at the probe frequency t_{pu} and the FWM frequency t_{fl} can be obtained from Eq. (2.10)-(2.12) as

$$t_{pu} = t_p + \eta t_u e^{i\phi} \tag{2.13}$$

and

$$t_{fl} = t_f + \eta t_l e^{-i\phi}, \tag{2.14}$$

where $\eta = \varepsilon_m/\varepsilon_p$ and $\phi = \phi_p - \phi_m$ and their intensities are given by $|t_{pu}|^2$ and $|t_{fl}|^2$, respectively. In order to study the transmitted fields from a ring cavity resonator, we use parameters similar to the previous studies [117, 122]. The strong control field of wavelength $\lambda = 775$ nm couples to two movable mirrors having resonance frequencies $\omega_1 = 2\pi \times 56.98$ MHz and $\omega_2 = 2\pi \times 46.62$ MHz. Further, we consider the mass of these two mirrors to be the same as $m_1 = m_2 = 20$ ng, the single-photon optomechanical coupling strengths are $g_1 = 2\pi \times 12$ GHz nm^{-1} $\times\sqrt{\hbar/m_1\omega_1}$ and $g_2 = 2\pi \times 12$ GHz nm^{-1} $\times\sqrt{\hbar/m_2\omega_2}$, the cavity decay rate $\kappa = 2\pi \times 15$ MHz, the mechanical damping rates are $\gamma_1 = \gamma_2 = 2\pi \times 4.1$ KHz, and the angle between two successive arms of the ring cavity is $\theta = \pi/3$.

2.3 Numerical results of the controllable output probe field generation

First, we study the analogy between EIT in an atomic system and its mechanical counterpart. The mechanical system under consideration corresponds to the level diagram of Figure 2.2, which constitutes an excited level $|2\rangle$, ground state $|1\rangle$ and two metastable states $|3\rangle$ and $|4\rangle$. In an atomic system, the radiative decay rate γ_{21} of the excited state $|2\rangle$ is much higher than the non-radiative decay rate γ_{31} and γ_{41} of metastable states $|3\rangle$ and $|4\rangle$. This is one of the criteria for formation of transparency window. In optomechanics, the cavity decay rate κ and mechanical damping rate $\gamma_i (i \in 1, 2)$ play the same role as γ_{21} and $\gamma_{i1} (i \in 3, 4)$ in an atomic system.

We now explore the weak mechanical pump induced upper mechanical sideband transmission at frequency $\omega_m + \omega_c$ given by Eq. (2.12). In Figure 2.3, we plot the upper mechanical sideband intensity $|t_u|^2$ as a function of normalized mechanical drive detuning, $(\omega_m - \omega_1)/\kappa$. The black solid curve in Figure 2.3(a) demonstrate the maximum peak of the transmission intensity at relatively low control powers. The sharp nature of the spectrum appears because, the coupling of the mechanical drive between $|1\rangle$ and $|3\rangle$ is dominant compared to the control field coupling between $|2\rangle$ and $|3\rangle$. Further increase in the control power results in a gradual decrease in the upper mechanical sideband intensity together with power broadening as exhibited by the red dashed line as well as blue dashed-dotted line in Figure 2.3(a). The normal

mode splitting can be manifested in the upper mechanical sideband by increasing the control power as depicted in Figure 2.3(b). The strong control field gives rise to an increase in the pumping rate between $|2\rangle$ and $|3\rangle$. Consequently, the optical pumping rate becomes more significant than the cavity decay rate κ. Therefore, the population spends a greater fraction of time in the excited state $|2\rangle$ that results in power broadening in the upper mechanical sideband as indicated by the black solid line in Figure 2.3(b). Further increasing the control power leads to the normal mode splitting as delineated by the red dashed line and blue dashed-dotted line in Figure 2.3(b). It is clear from these two curves that the position of one normal mode is almost unaffected, whereas the distance between the other two normal modes keeps on increasing with larger control power [117]. As a result, the mechanical drive with frequency ω_m fails to couple resonantly with the mechanics ω_1, and an asymmetric power spectrum arises as shown in Figure 2.3(b). Moreover, the graphical nature is determined by the roots of $E(\omega_m)$ [24, 117], which are in general complex. The real parts of the roots determine the spectral line peak positions and imaginary parts are associated with their widths. The pole structures can be found out by considering the control power to be 35 mW with all other parameters remaining the same as mentioned earlier. The real parts of the roots of $E(\omega_m)$ provide the intensity maximum when normalized mechanical drive detuning, $(\omega_m - \omega_1)/\kappa$ values $-2.07, -0.32$ and 0.71 are in well agreement with Figure 2.3(b).

Next, we explore the role of the control field phase on the probe transmission by studying Eq. (2.13). Expanding Eq. (2.13), leads to $|t_{pu}|^2 = |t_p|^2 + |\eta t_u|^2 + \eta t_p t_u^* e^{i(\phi_m - \phi_p)} + \eta t_p^* t_u e^{-i(\phi_m - \phi_p)}$ which corresponds to the phase-dependent transmission of the output probe field. The cross-terms give rise to the interference effect between the cavity-generated probe field and the upper mechanical sideband. Moreover, the interference terms can be adjusted by tuning the control field phase ϕ_c while the other two field phases are taken to be equal *i.e.,* ϕ_m=ϕ_p. The phase-sensitive behavior of the control field ϕ_c on the probe transmission is displayed in Figure 2.4. The solid black curve of Figure 2.4 depicts two transparency windows

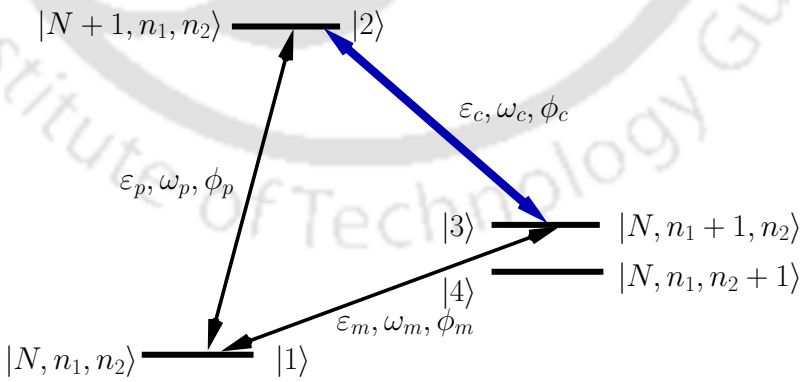

Figure 2.2: The level diagram of the ring cavity optomechanical system. $|N\rangle$, $|n_1\rangle$ and $|n_2\rangle$ are the number states of the cavity mode, phonon modes of the first and second nanomechanical oscillators, respectively. The application of a strong control field to the red-detuned cavity allows the transition $|N+1, n_1, n_2\rangle \leftrightarrow |N, n_1+1, n_2\rangle$. Whereas the presence of a weak probe field increases the cavity photon number by unity. An external weak mechanical force directly couples $|N, n_1, n_2\rangle \leftrightarrow |N, n_1 + 1, n_2\rangle$.

for the output probe field which are created in the absence of mechanical drive. These two transparency windows are located around $\delta \approx \omega_1$ and ω_2 with slightly unequal amplitudes. The unequal amplitudes emerge due to the difference in radiation pressure force experienced by the two nearly degenerate oscillators. Figure 2.4 also confirms that the enhancement as well as suppression of the probe transmission around the upper transparency window can be obtained as the resonance frequency of the external periodic drive (ω_m) matches with the beat frequency between the control and the probe field (δ). Note that the mechanical pump is in-phase with the input probe field. The values of control phase ϕ_c for the red dashed and blue dot-dashed curves of Figure 2.4, are 0 and $\pi/2$, respectively.

We next focus on the probe transmission at the upper transparency window placed at $\delta = \omega_1$. In Figure 2.5, we have plotted probe transmission as a function of normalized

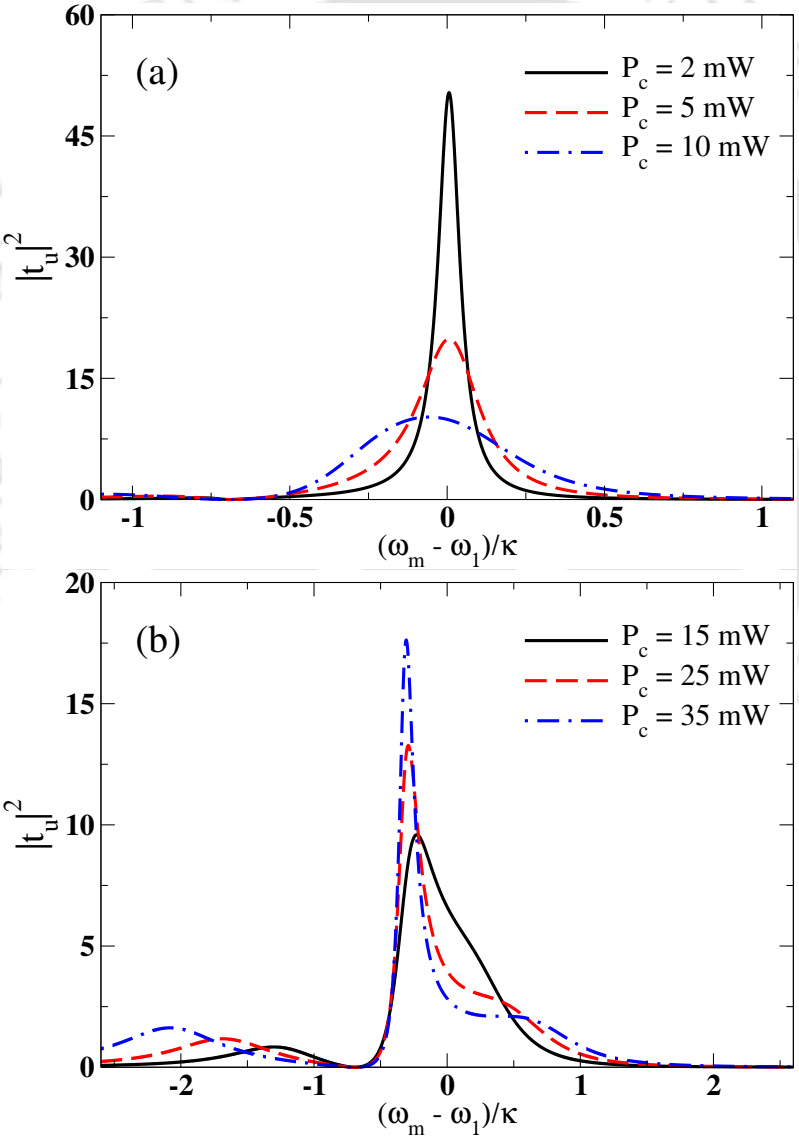

Figure 2.3: Normalised transmission at the upper mechanical sideband is plotted against normalized mechanical drive detuning for different control powers. The other parameters are $\omega_1 = 2\pi \times 56.98$ MHz, $\omega_2 = 2\pi \times 46.62$ MHz, $\gamma_1 = \gamma_2 = 2\pi \times 4.1$ KHz, $\kappa = 2\pi \times 15$ MHz and the effective cavity detuning is $\Delta' = 2\pi \times 51.8$ MHz.

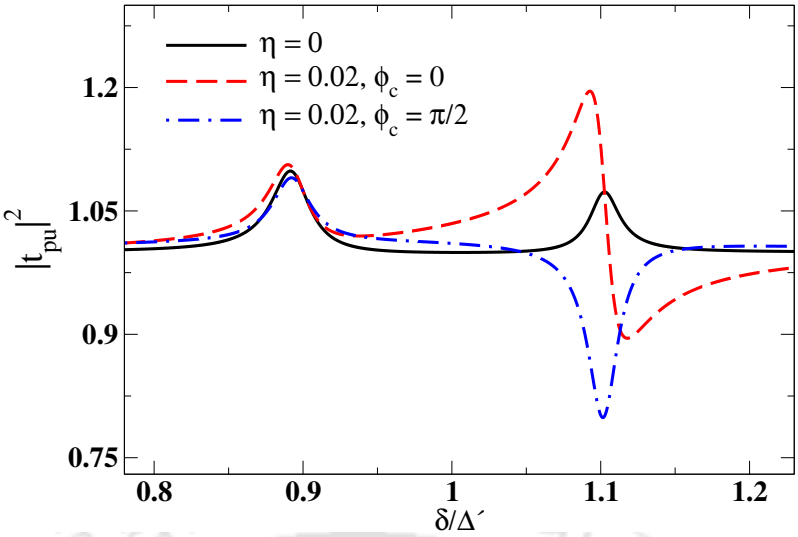

Figure 2.4: The control field phase-dependent normalized transmission of the output probe field is plotted as a function of normalized detuning between the control and the probe field when the mechanical drive is in-phase with the input probe field. All other parameters are the same as before.

mechanical drive amplitude η for different values of ϕ_c. The constructive interference between the cavity-generated probe field and the mechanical pump-induced upper sideband, substantially enhances the output probe intensity for $\phi_c = 0, \pi$, and $3\pi/2$. Nonetheless, the destructive interference between these two components forces the probe transmission to diminish, as seen from the red dashed curve at $\eta = 0.18$.

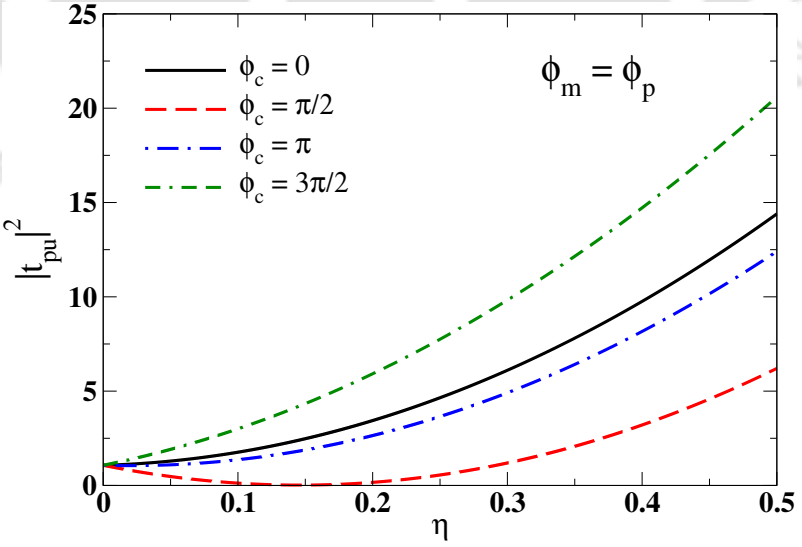

Figure 2.5: The normalized optical probe field transmission through the upper transparency window is plotted as a function of normalized mechanical drive amplitude for different values of the control field phase. Here we consider the control field power to be 2 mW.

2.3.1 Group delay

Superposition of monochromatic waves centred around a carrier frequency (ω_s) can give rise to a light pulse with finite width. The envelope of the light pulse moves with a group velocity inside a dispersive medium. The existence of a transparency window is mandatory for pulse propagation through the otherwise opaque medium. To construct analytical expression for the group delay, we consider the envelope of the optical probe pulse as

$$f(t_0) = \int_{-\infty}^{\infty} \tilde{f}(\omega) e^{-i\omega t_0} d\omega,$$

where $\tilde{f}(\omega)$ corresponds to the envelope function in the frequency domain. Accordingly, the reflected output probe pulse can be expressed as

$$\begin{aligned} f^R(t_0) =& \int_{-\infty}^{\infty} t_{pu}(\omega)\tilde{f}(\omega)e^{-i\omega t_0} d\omega, \\ =& e^{-i\omega_s t_0} \int_{-\infty}^{\infty} t_{pu}(\omega_s+\delta)\tilde{f}(\omega_s+\delta)e^{-i\delta t_0} d\delta. \end{aligned} \tag{2.15}$$

Now we can expand $t_{pu}(\omega_s+\delta)$ in the vicinity of ω_s by Taylor series expansion and keeping the terms upto first order in δ

$$t_{pu}(\omega_s+\delta) \approx t_{pu}(\omega_s) + \delta \frac{dt_{pu}}{d\omega}\bigg|_{\omega_s}. \tag{2.16}$$

On substituting Eq. (2.16) into Eq. (2.15), we find

$$\begin{aligned} f^R(t_0) =& \; e^{-i\omega_s t_0} \int_{-\infty}^{\infty} t_{pu}(\omega_s) e^{-i\delta\left(t_0 + \frac{i}{t_{pu}(\omega_s)} \frac{dt_{pu}}{d\omega}|_{\omega_s}\right)} \tilde{f}(\omega_s+\delta) d\delta, \\ =& \; e^{-i\omega_s t_0} \int_{-\infty}^{\infty} t_{pu}(\omega_s) e^{-i\delta(t_0-\tau_g)} \tilde{f}(\omega_s+\delta) d\delta \\ =& \; t_{pu}(\omega_s) e^{-i\omega_s\tau_g} f(t_0-\tau_g), \end{aligned} \tag{2.17}$$

where time delay is defined as [102]

$$\tau_g = \mathrm{Re}\left[\frac{-i}{t_{pu}(\omega_s)}\left(\frac{dt_{pu}}{d\omega}\right)\bigg|_{\omega_s}\right]. \tag{2.18}$$

We examine the effect of a weak mechanical pump on the probe pulse propagation delay as depicted in Figure 2.6. Here, we focus on the upper transparency window centered at $\delta \approx \omega_1$ and the control field intensity 2 mW and phase $3\pi/2$, respectively. Additionally, the input probe pulse is in phase with the external mechanical drive. The black solid curve of Figure 2.6(a) corresponds to the probe pulse propagation delay $\tau_g = 0.43$ μs for $\eta = 0.07$. Further increase in the mechanical pump amplitude causes a gradual decrease in the probe pulse propagation delay. Even then, it displayed slow light phenomena as confirmed from the red dashed curve in Figure 2.6(a). In Figure 2.6(b), we change the control phase to $\pi/2$ and keep all other parameters the same as mentioned before. For a mechanical pump with

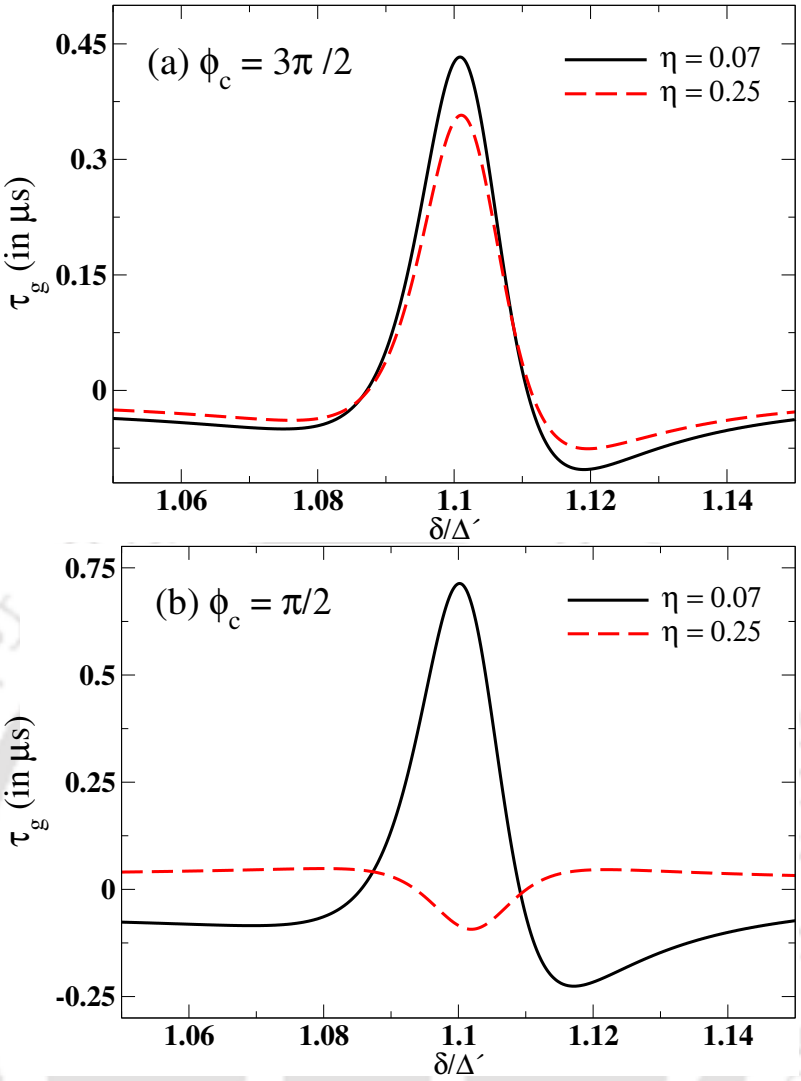

Figure 2.6: Time delay of the probe pulse for different mechanical drive amplitudes have been plotted against the normalized probe detuning δ/Δ' while the control power is 2 mW. The mechanical drive is considered to be in-phase with the probe field. All other parameters are taken as the same as Figure 2.3.

amplitude $\eta = 0.07$, we observe the delay of the output probe pulse as 0.71 μs. It is also evident from the red dashed curve in Figure 2.6(b) that a relatively stronger mechanical pump can switch the light propagation velocity from slow to fast in the presence of control phase $\phi_c = \pi/2$. The probe pulse advancement corresponding to the red dashed curve is 0.09 μs for $\eta = 0.25$.

To verify the above result, we consider the carrier frequency of the Gaussian probe pulse centered at the upper transparency window *i.e.*, $\delta = \omega_1$. The envelope of the pulse can be written as

$$\tilde{f}(\omega) = \frac{\varepsilon_p}{\sqrt{\pi\Gamma^2}} e^{-\frac{(\omega-\omega_s)^2}{\Gamma^2}},$$

where Γ is the spectral width of the pulse. We keep in mind that the spectrum width Γ must be well-contained in the transparency window for a distortionless probe pulse propagation. Successively numerically integrating Eq. (2.15) bring out the temporal profile of the output probe pulse. The pulse parameters such as gain or absorption

and group velocity can be obtained by examining the nature of the transmission coefficient t_{pu}. For numerical integration, we have used the control power 2 mW with phase $\pi/2$. The temporal intensity profile of the input probe pulse with Γ as $2\pi \times 129.5$ kHz is presented by the solid black curve of Figure 2.7. The utilisation

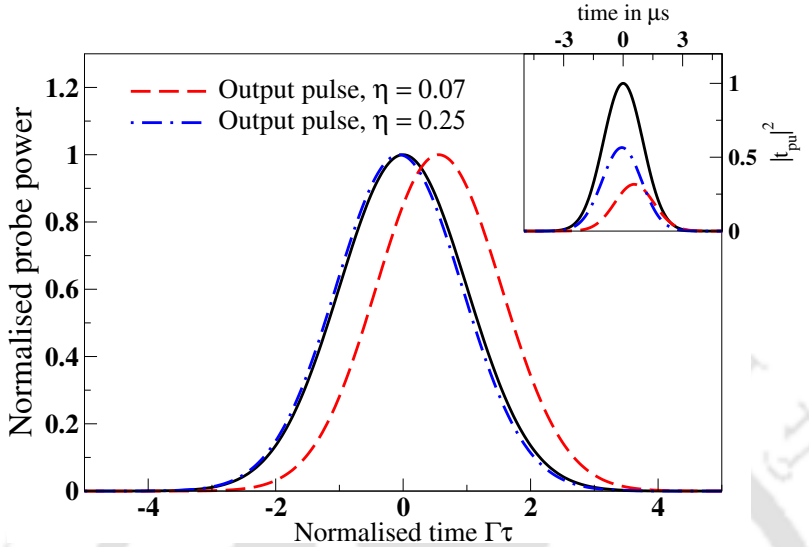

Figure 2.7: The normalized probe pulse intensity with respect to its peak value is plotted against the normalized time $\Gamma\tau$. The solid black curve represents the input probe pulse propagating at speed c through the ring cavity. The red dashed and the blue dot-dashed curves represent the output probe pulse in the presence of mechanical pump with $\eta = 0.07$ and 0.25, respectively. Variation of the relative intensity of the output probe pulse is shown in the inset.

of the weak mechanical driving field $\eta = 0.07$ is visible from the red dashed curve of Figure 2.7 that exhibits the slow pulse propagation. The group delay 0.69 μs is measured from the peak separation between the input pulse and the output pulse. The sensitive nature of the group delay on mechanical pump amplitude can be seen in the blue dot-dashed curve of Figure 2.7. We estimate an advancement of the probe pulse around 0.08 μs. The physics behind the formation of slow and fast probe pulse turns out to be a reasonable suppression of amplitudes due to interference of phases among the constituents waves. It can be understood from Eq. 2.13, which can also be expressed as $|t_{pu}|^2 = |t_p|^2 + |\eta t_u|^2 + \eta t_p t_u^* e^{i(\phi_m - \phi_p)} + \eta t_p^* t_u e^{-i(\phi_m - \phi_p)}$. Here the cross-terms signify the destructive interference between cavity-generated probe pulse and the mechanical pump-induced upper sideband. For normalized mechanical drive amplitude $\eta = 0.07$ and 0.25, the dominating behavior appears through the destructive interference over the upper mechanical sideband intensity. As a result, a reasonable discretion in the probe pulse output has been observed. As depicted in the red dashed and blue dash-dotted curve of the inset of Figure 2.7, the relative power of the output field with respect to input intensity are 0.32 and 0.56 for $\eta = 0.07$ and 0.25, respectively. Interestingly, the temporal width of the probe pulse is almost unaltered during the propagation through the ring cavity optomechanical system. This numerical result is in very good agreement with our analytical results for the probe pulse propagation delay as depicted in Figure 2.6(b). Finally the mechanical coupling intensity and control phase play key roles in changing the probe pulse velocity from slow to fast light.

2.4 Controllable Stokes field generation

In the context of optomechanics, the Stokes field generation through the nonlinear four-wave mixing process has been investigated quite extensively in previous literature [109,123,124]. Further studies [110] illustrate that the phase difference between the applied mechanical pump and the input probe field (*e.g.* $\phi = \phi_m - \phi_p$) leads to the controllable Stokes field generation ($2\omega_c - \omega_p$) while the resonance condition ($\delta = \omega_m = \omega_1$) is well satisfied. However, this section presents the control field phase ϕ_c dependency of the Stokes field generation in a mechanically driven optomechanical system.

To study the Stokes field generation in an optomechanical system, we consider Eq.

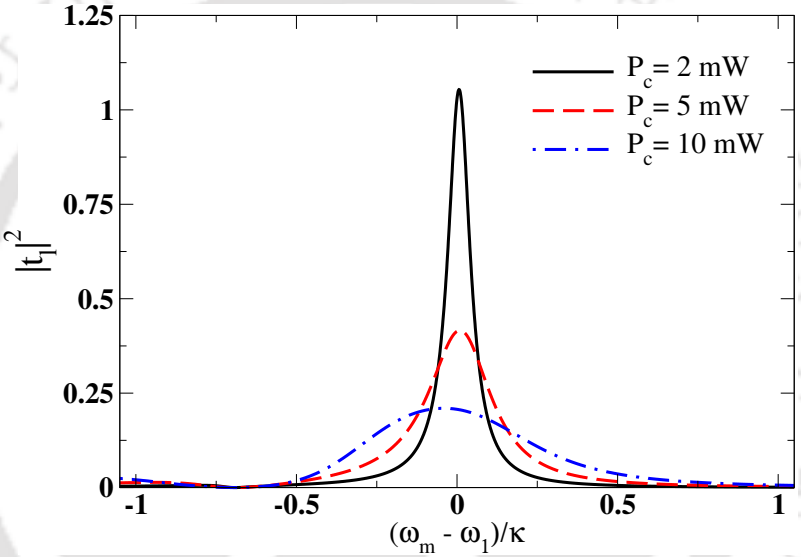

Figure 2.8: The normalized lower sideband transmission is plotted against normalized mechanical drive detuning for three different control powers $P_c = 2, 5$ and 10 mW. All other parameters are same as in Figure 2.3.

(2.14) which can be expressed as $|t_{fl}|^2 = |t_f|^2 + |\eta t_l|^2 + \eta t_l^* t_f e^{i(\phi_m - \phi_p)} + \eta t_f^* t_l e^{-i(\phi_m - \phi_p)}$. The first term corresponds to the radiation pressure induced Stokes field generation. The second term represents the external mechanical pump induced lower mechanical sideband generation. Whereas, the cross-terms emulate the effect of interference between these two components. In Figure 2.8, the lower mechanical sideband intensity ($|t_l|^2$) has been displayed as a function of normalized mechanical drive detuning, $(\omega_m - \omega_1)/\kappa$. The black solid curve of Figure 2.8 demonstrates a significant lower mechanical sideband generation as the mechanical coupling dominates over the weak radiation pressure coupling. Further increase in the control power results in a gradual decrease in the lower sideband intensity along with power broadening as presented by the red dashed and blue dash-dotted lines of Figure 2.8. It is also evident from Figure 2.8 that the lower mechanical sideband intensity is independent of the control field phase due to the absolute square of lower sideband amplitude. The importance of the control field phase becomes distinct after the expansion of $|t_{fl}|^2$. The control phase-induced interference effects that arise from cross terms can persist

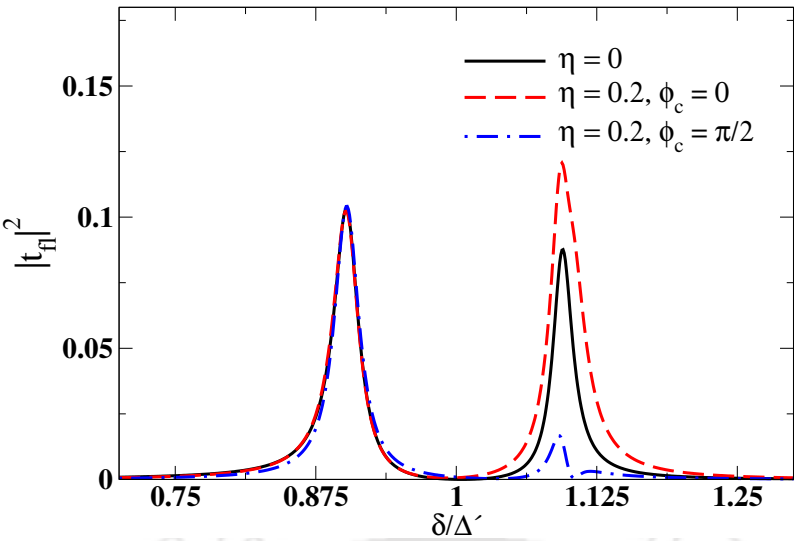

Figure 2.9: The normalized intensity of the generated Stokes field is plotted as a function of normalized detuning between the control and the probe field. The mechanical drive is in-phase with the input probe field. The control power is taken as 2 mW. All other parameters are same as in Figure 2.3.

only around the upper transparency window, as the resonance frequency of the external mechanical pump (ω_m) matches with the beat frequency between the control and the probe field (δ). Hence, the control field phase ϕ_c can be used to manipulate the interference terms that allow controlling the Stokes field generation around the upper transparency window even for a fixed value of ϕ (*e.g.*, $\phi = 0$) as shown in Figure 2.9. The black solid line of Figure 2.9 depicts the radiation pressure-induced Stokes field generation in the absence of the mechanical pump. The enhancement as well as suppression of the Stokes field generation around $\delta = \omega_1$, can be achieved by the application of a weak mechanical pump at different values of control phase ϕ_c. The values of ϕ_c for the red-dashed and blue dot-dashed lines of Figure 2.9 are 0 and $\pi/2$, respectively.

We next concentrate on the Stokes field generation around the upper transparency window ($\delta = \omega_1$). In Figure 2.10, we have plotted $|t_{fl}|^2$ as a function of normalized mechanical drive amplitude η for different control phases ϕ_c. The constructive interference between the cavity-generated Stokes field and the mechanical pump-induced lower sideband enhances the output Stokes field intensity for the control phases $0, \pi$, and $3\pi/2$. The destructive interference between these two components subdues the output Stokes field generation for the normalized mechanical drive amplitude $\eta \approx 0.3$ as seen from the red dashed curve of Figure 2.10. Hence, the phase-dependent control field is the main key behind the enhancement or complete suppression of Stokes field generation in a ring cavity.

2.5 Conclusion

In conclusion, we have carried out theoretical investigations on control field phase assisted tunable group delay of the probe transmission as well as efficient FWM field generation in a ring cavity optomechanical system. The optomechanical system

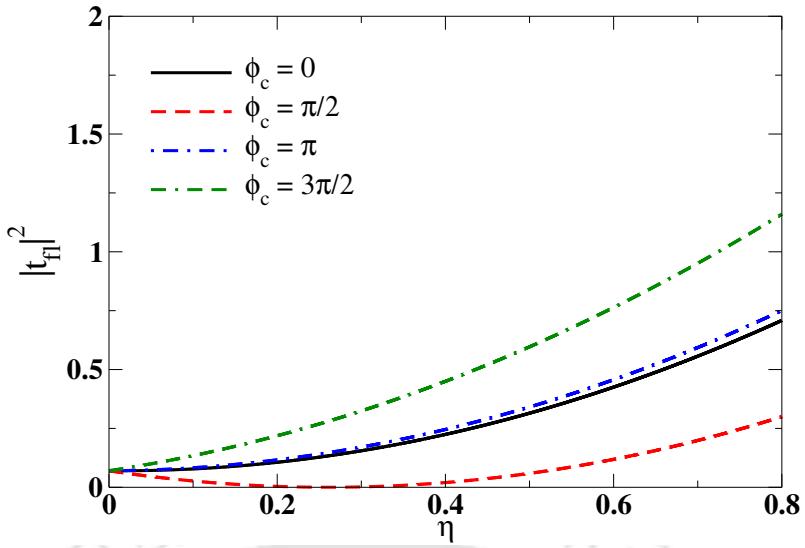

Figure 2.10: The normalized intensity of the generated Stokes field through the upper transparency window is plotted as a function of normalized mechanical drive amplitude for different values of the control phase. The external mechanical pump is considered to be in-phase with the applied probe field ($\phi_m = \phi_p$). Here we consider the control field power to be 2 mW.

consists of a red-detuned ring cavity that is an assembly of two nearly degenerate movable mirrors. A double OMIT window is formed by the application of strong control and weak probe fields provided the two-photon resonance condition is satisfied. We apply an external mechanical drive to modulate the vibration of one of the movable mirrors. We found that the strength of the output probe field around the upper transparency window can be enhanced due to the interference between the cavity-generated probe field and the mechanical drive-induced upper sideband in the presence of a mechanical drive which is in phase with the applied probe field. Moreover, the control field phase-sensitive behavior of the interference provides an extra tunability to control the output probe power around the upper transmission window. We demonstrate that a tunable group delay of the probe pulse in the course of propagation through the upper transparency window can be achieved by using a suitable amplitude of the mechanical pump and the phase of the control field while the relative phase between the probe field and the mechanical drive is kept fixed. To verify this claim, we also study the propagation of a Gaussian probe pulse that is well-contained in the upper transparency window. The presence of the external mechanical pump amplitude along with suitable control field phases can switch the group delay of the probe pulse from slow to fast light. Further, the control field phase can enhance and surpasses the Stokes field generation via FWM. Our work may find potential application for storage and retrieval of the optical signals with the aid of the mechanical oscillator which provides a much longer lifetime than the atomic medium.

Chapter 3

Gain assisted controllable fast light generation in cavity magnomechanics

3.1 Introduction

In the preceding chapter, we have explored the control field phase-dependent response of the output field transmission from a red-detuned ring cavity optomechanical system. There, we have utilized the idea of OMIT. Further investigations in this direction predicted better controllability of light transmission incorporating $\mathcal{PT}$-symmetry in a coupled two-mode optomechanical systems. $\mathcal{PT}$-symmetry elucidates the dynamics of a coupled system characterized by gain and loss. Here, $\mathcal{P}$ stands for the parity operation that results in an interchange between the two constituent modes of the system. The time reversal operator $\mathcal{T}$ takes i to $-i$. $\mathcal{PT}$-symmetry demands the Hamiltonian is commutative with the joint $\mathcal{PT}$ operators *i.e.,* $[H, PT] = 0$. This system possesses a spectrum of entirely real and imaginary eigenvalues that retain distinguishable characteristics [125]. The point separating these two eigenvalues is the exceptional point (EP) [126] where the two eigenvalues coalesce, and the system degenerates. A natural testbed for $\mathcal{PT}$-symmetric Hamiltonian is optical and quantum optical systems [127–129] which already led to the demonstration of some of the exotic phenomena, like nonreciprocal light propagation [130], unidirectional invisibility [131, 132], optical sensing and light stopping [133].

Recently, researchers have been putting tremendous effort into realizing a hybrid system containing a cavity and a ferrimagnetic insulator with high spin density and low damping rate, commonly known as cavity magnonics. In a bias magnetic field, the ferrimagnetic insulator supports quantized magnetization modes, namely, the magnons [82,134]. With strongly coupled magnon-photon modes, cavity magnonics is an excellent platform for studying many strong-coupling cavity QED effects [44, 135, 136]. The shape deformation of the ferrimagnetic insulator induces the coupling between the magnon and the phonon mode [134]. This combined setup of magnon-photon-phonon modes, namely the cavity magnomechanics, has already demonstrated magnomechanically induced transparency [134], magnon-induced dynamical backaction [137], magnon-photon-phonon entanglement [138,139], squeezed state generation [140], magnomechanical storage and retreival of a quantum state

[141]. Exploring the integration of non-Hermitian physics into magnon-assisted hybrid quantum systems is a fascinating endeavor. This approach aims to harness the unique properties of non-Hermitian dynamics to enhance and manipulate the functionality of these systems. The second-order exceptional point is detected in a two-mode cavity-magnoic system, where the gain of the cavity mode is accomplished by using the idea of coherent perfect absorption [142]. Anti-$\mathcal{PT}$ symmetry has been realized experimentally [143], where the adiabatic elimination of the cavity field produces dissipative coupling between two magnon modes. Beyond the unique spectral responses, these non-Hermitian systems can manipulate the output microwave field transmission [144, 145]. The underlying mechanism behind such an application is magnetically induced transparency [134, 146]. Further studies in this direction establish the importance of the weak magnon-phonon coupling to create double transmission windows separated by an absorption peak. Further, manipulating the absorption spectrum is also possible by varying the amplitude and phase of the applied magnetic field [147].

This chapter investigates the effect of medium gain on controllable advancement and transmission of the microwave field generation from a coupled cavity magnomechanical system. Optical coupling between a passive cavity resonator containing ferrimagnetic yttrium iron garnet (YIG) sphere and a gain-assisted auxiliary cavity can form a coupled cavity resonator. An external drive has been used to deform the YIG sphere's shape, resulting in the magnon-phonon interaction in the passive cavity. We show how the gain of the auxiliary cavity helps to overcome absorptive behaviour in our hybrid system. As a result, the output microwave field amplifies at the resonance condition. Moreover, the weak magnon-phonon interaction exhibits anomalous dispersion accompanied by a gain spectrum, demonstrating superluminal light. We also examine how the slope of the dispersion curve can be controlled by tuning the photon hopping interaction strength between the two cavities.

The chapter is organized as follows. In Section 3.2, a theorical model for the compound cavity magnomechanical system with $\mathcal{PT}$-symmetric resonator is described. The Heisenserg equations of motion to govern the expectation values of operators of the system are derived in this Section. In Section 3.3.1, we analyse the stability criteria of the model system and examine the effect of the auxiliary cavity gain on the absorptive and dispersive response of the system in Section 3.3.2. Section 3.3.3 discusses the output probe field transmission. Further, the group velocity of the optical probe pulse has been studied analytically and verified numerically in Section 3.3.4. Finally, we draw our conclusions in Section 3.4.

3.2 Theoretical Model

The system under consideration is a hybrid cavity magnomechanical system that consists of two coupled microwave cavity resonators. One of the resonators is passive and contains a YIG sphere inside it. We refer to this resonator as a cavity magnomechanical (CMM) resonator. Applying a uniform bias magnetic field to the YIG sphere excites the magnon mode. The magnon mode, in turn, couples with the cavity field. Nonetheless, the external bias magnetic field results in shape deformation of the YIG sphere, leading to the magnon-phonon interaction. The second resonator (degenerate with the first one) is coupled to the first resonator via optical tunnelling at a rate J. Two input fields drive the CMM resonator. The ampli-

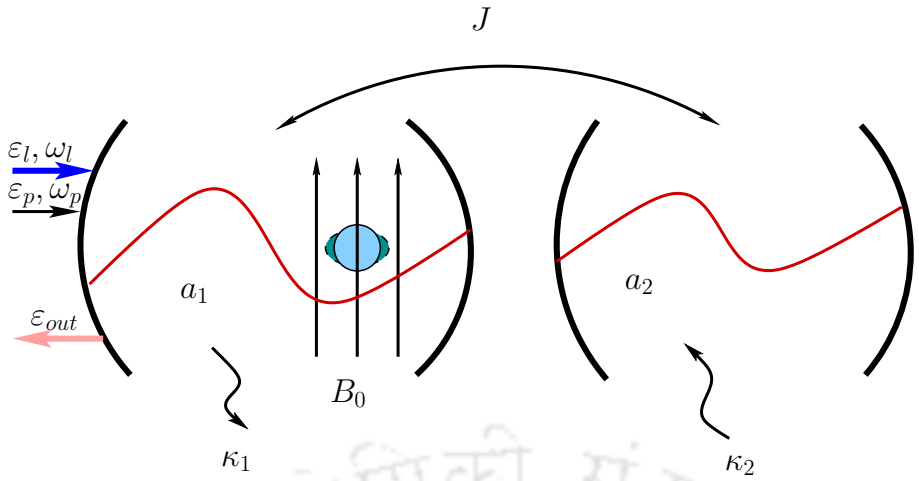

Figure 3.1: The schematic diagram of a hybrid cavity magnomechanical system. The system consists of two coupled microwave cavities. One of them is passive, and another one is active. The passive cavity contains a ferrimagnetic YIG sphere inside it. The applied bias magnetic field produces the magnetostrictive interaction between magnon and phonon. The coupling rates between the magnon-photon and magnon-phonon are g_{ma} and g_{mb}, respectively. Strong control field of frequency ω_l and a weak probe field of frequency ω_p are applied to the passive cavity. The output field is denoted as ε_{out}.

tude of the control, ε_l, and probe fields, ε_p, are given by $\varepsilon_i = \sqrt{P_i/\hbar\omega_i}, (i \in l, p)$ with P_i and ω_i being the power and frequency of the respective input fields. The Hamiltonian of the combined system can be written as

$$\begin{aligned} H &= \hbar\omega_c a_1^\dagger a_1 + \hbar\omega_c a_2^\dagger a_2 + \hbar\omega_m m^\dagger m + \hbar\omega_b b^\dagger b + \hbar J(a_1^\dagger a_2 + a_2^\dagger a_1) \\ &+ \hbar g_{ma}(a_1^\dagger m + a_1 m^\dagger) + \hbar g_{mb} m^\dagger m(b^\dagger + b) + i\hbar\sqrt{2\eta_a\kappa_1}\varepsilon_l(a_1^\dagger e^{-i\omega_l t} - a_1 e^{i\omega_l t}) \\ &+ i\hbar\sqrt{2\eta_a\kappa_1}\varepsilon_p(a_1^\dagger e^{-i\omega_p t} - a_1 e^{i\omega_p t}), \end{aligned} \tag{3.1}$$

where the first four terms of the Hamiltonian describe the free energy associated with each system's constituents. The constituents of our model are characterized by their respective resonance frequencies: ω_c for the cavity mode, ω_m for the magnon mode, ω_b for the phonon mode. The annihilation operators for the cavity, magnon and phonon modes are represented by a_i, $(i = 1, 2)$, m and b, respectively. The fifth term signifies the photon exchange interaction between the two cavities with strength, J. The sixth term appear due to the dipole-dipole interaction, which represents a beam-splitter-like linear interaction, provided the resonance frequency of magnon and photon modes are closely aligned [148]. It is important to note that the magnomechanical interaction arises due to the magnetostrictive effect caused by the external magnetic field. The seventh term of the Hamiltonian describes the radiation pressure-like nonlinear interaction that emerges from the magnetostrictive energy in the case of the phonon frequency, which is much lower than the magnon frequency [134]. Finally, the last two terms signify the interaction between the cavity field and two input fields. The cavity, magnon and phonon decay rates are characterized by κ_1, κ_m and κ_b, respectively. The coupling between the CMM resonator and the output port is given by $\eta_a = \kappa_{c_1}/2\kappa_1$, where κ_{c_1} is the cavity external decay rate. In particular, we will consider the CMM resonator to be working in the

critical-coupling regime where η_a is 1/2. At this point, it is convenient to move to a frame rotating at ω_l. Following the transformation $H_{rot} = RHR^\dagger + i\hbar\,(\partial R/\partial t)\,R^\dagger$ with $R = e^{i\omega_l(a_1^\dagger a_1 + a_2^\dagger a_2 + m^\dagger m)t}$, the Hamiltonian in Eq. (3.1) can be rewritten as

$$\begin{aligned} H_{rot} &= \hbar\Delta_a(a_1^\dagger a_1 + a_2^\dagger a_2) + \hbar\Delta_m m^\dagger m + \hbar\omega_b b^\dagger b + \hbar J(a_1^\dagger a_2 + a_2^\dagger a_1) \\ &+ \hbar g_{ma}(a_1^\dagger m + a_1 m^\dagger) + \hbar g_{mb} m^\dagger m(b^\dagger + b) + i\hbar\sqrt{2\eta_a\kappa_1}\varepsilon_l(a_1^\dagger - a_1) \\ &+ i\hbar\sqrt{2\eta_a\kappa_1}\varepsilon_p(a_1^\dagger e^{-i\delta t} - \text{h.c}), \end{aligned} \tag{3.2}$$

where $\Delta_a = \omega_c - \omega_l$ ($\Delta_m = \omega_m - \omega_l$) and $\delta = \omega_p - \omega_l$ are, respectively, the cavity (magnon) and probe detuning. The mean response of the system can be obtained by the Heisenberg - Langevin equation as $\langle\dot{\mathcal{O}}\rangle = i/\hbar\langle[H_{rot}, \mathcal{O}]\rangle + \langle N\rangle$. Further, we consider the quantum fluctuations (N) as white noise. Then starting form Eq. (3.2), the equations of motion of the system can be expressed as

$$\langle\dot{a_1}\rangle = (-i\Delta_a - \kappa_1)\langle a_1\rangle - ig_{ma}\langle m\rangle - iJ\langle a_2\rangle + \sqrt{2\eta_a\kappa_1}\varepsilon_l + \sqrt{2\eta_a\kappa_1}\varepsilon_p e^{-i\delta t}, \tag{3.3a}$$

$$\langle\dot{m}\rangle = (-i\Delta_m - \kappa_m)\langle m\rangle - ig_{ma}\langle a_1\rangle - ig_{mb}\langle m\rangle(\langle b^\dagger\rangle + \langle b\rangle), \tag{3.3b}$$

$$\langle\dot{b}\rangle = (-i\omega_b - \kappa_b)\langle b\rangle - ig_{mb}\langle m^\dagger\rangle\langle m\rangle, \tag{3.3c}$$

$$\langle\dot{a_2}\rangle = (-i\Delta_a + \kappa_2)\langle a_2\rangle - iJ\langle a_1\rangle, \tag{3.3d}$$

where $\kappa_1(\kappa_2)$ denote the internal energy loss (gain) of the passive (auxiliary) cavity, κ_m and κ_b denote the amplitude decay rate of the magnon mode and phonon mode, respectively. Experimentally one can realize the gain by nullifying the output field from the second cavity that leads to the addition of photons at a rate κ_2 [142]. We note that $\kappa_2 > 0$ corresponds to a coupled passive-active CMM resonators system and $\kappa_2 < 0$ describes a passive-passive coupled CMM resonators system. Assuming the control field amplitude ε_l to be larger than the probe field ε_p, each operator expectation values $\langle\mathcal{O}(t)\rangle$ can be decomposed into its steady-state values $\mathcal{O}_s$ and a small fluctuating term $\delta\mathcal{O}(t)$. The steady-state values of each operator are

$$a_{1s} = \frac{(-i\Delta_a + \kappa_2)(-ig_{ma}m_s + \sqrt{2\eta_a\kappa_1}\varepsilon_l)}{(i\Delta_a + \kappa_1)(-i\Delta_a + \kappa_2) - J^2}, \tag{3.4a}$$

$$m_s = \frac{-ig_{ma}a_{1s}}{i\Delta_m' + \kappa_m}, \tag{3.4b}$$

$$b_s = \frac{-ig_{mb}|m_s|^2}{i\omega_b + \kappa_b}, \tag{3.4c}$$

$$a_{2s} = \frac{iJa_{1s}}{(-i\Delta_a + \kappa_2)}. \tag{3.4d}$$

While the fluctuating parts of Eq. (3.3a)-(3.3d) can be expressed as

$$\delta\dot{a}_1 = -\left(i\Delta_a + \kappa_1\right)\delta a_1 - iJ\delta a_2 - ig_{ma}\delta m + \sqrt{2\eta_a\kappa_1}\varepsilon_p e^{-i\delta t}, \tag{3.5a}$$

$$\delta\dot{m} = -(i\Delta_m' + \kappa_m)\delta m - ig_{ma}\delta a_1 - iG\delta b - iG\delta b^\dagger, \tag{3.5b}$$

$$\delta\dot{b} = -\left(i\omega_b + \kappa_b\right)\delta b - iG\delta m^\dagger - iG^*\delta m, \tag{3.5c}$$

$$\delta\dot{a}_2 = -\left(i\Delta_a - \kappa_2\right)\delta a_2 - iJ\delta a_1, \tag{3.5d}$$

where $\Delta_m' = \Delta_m + g_{mb}(b_s + b_s^*)$ is the effective magnon detuning and $G = g_{mb}m_s$ is the enhanced magnon-phonon coupling strength. For simplicity, we express these fluctuation equations as

$$\frac{d}{dt}|\psi\rangle = H_{eff}|\psi\rangle + F, \tag{3.6}$$

where the fluctuation vector $|\psi\rangle = (\delta a_1, \delta a_1^\dagger, \delta a_2, \delta a_2^\dagger, \delta b, \delta b^\dagger, \delta m, \delta m^\dagger)^T$, and input field $F = (\sqrt{2\eta_a\kappa_1}\varepsilon_p e^{-i\delta t}, \sqrt{2\eta_a\kappa_1}\varepsilon_p e^{i\delta t}, 0, 0, 0, 0, 0, 0)^T$. Next, we adopt the following ansatz to solve Eq. (3.5a)-(3.5d):

$$\delta a_1(t) = A_{1+}e^{-i\delta t} + A_{1-}e^{i\delta t}, \tag{3.7a}$$
$$\delta m(t) = M_{+}e^{-i\delta t} + M_{-}e^{i\delta t}, \tag{3.7b}$$
$$\delta b(t) = B_{+}e^{-i\delta t} + B_{-}e^{i\delta t}, \tag{3.7c}$$
$$\delta a_2(t) = A_{2+}e^{-i\delta t} + A_{2-}e^{i\delta t}. \tag{3.7d}$$

Here A_{i+} and A_{i-} correspond to the i^{th} cavity generated probe field amplitude and the four-wave mixing field amplitude, respectively. By considering $h_1 = -i\Delta_a + i\delta - \kappa_1$, $h_2 = -i\Delta_a - i\delta - \kappa_1$, $h_3 = -i\Delta_a + i\delta + \kappa_2$, $h_4 = -i\Delta_a - i\delta + \kappa_2$, $h_5 = -i\omega_b + i\delta - \kappa_b$, $h_6 = -i\omega_b - i\delta - \kappa_b$, $h_7 = -i\Delta_m' + i\delta - \kappa_m$, $h_8 = -i\Delta_m' - i\delta - \kappa_m$, we obtain A_{1+} which corresponds to the output probe field amplitude from the CMM resonator as

$$A_{1+}(\delta) = \frac{C(\delta)}{D(\delta)}, \tag{3.8}$$

where

$$C(\delta) = -\sqrt{2\eta_a\kappa_1}\,\varepsilon_p\, h_3(h_5\, h_6^*\, h_7\, \Gamma_1 + |G|^2(h_5 - h_6^*)(J^2\, h_7 + h_4^*\, h_2^*\, h_7^* - \Gamma_1)), \tag{3.9a}$$

$$D(\delta) = h_5\, h_6^*\, \Gamma_1(g_{ma}^2\, h_3 + h_7\, \Gamma_2) + |G|^2(h_5 - h_6^*) \\ (J^2(g_{ma}^2\, h_3 + \Gamma_2(h_7 - h_8^*)) - h_4^*(\Gamma_2\Gamma_3 - \Gamma_4)). \tag{3.9b}$$

To express the above equation, we have used

$$\Gamma_1 = J^2\, h_8^* + h_4^*\, g_{ma}^2 + h_2^*\, h_4^*\, h_8^*, \tag{3.10a}$$
$$\Gamma_2 = h_1\, h_3 + J^2, \tag{3.10b}$$
$$\Gamma_3 = g_{ma}^2 - h_2^*\,(h_7 - h_8^*), \tag{3.10c}$$
$$\Gamma_4 = h_2^*\, h_3\, g_{ma}^2. \tag{3.10d}$$

The output field from the CMM resonator is obtained by the cavity input-output relation

$$\varepsilon_{out} = \sqrt{2\eta_a\kappa_1}\langle a_1\rangle - \varepsilon_l - \varepsilon_p e^{-i\delta t}. \tag{3.11}$$

By substituting Eq. (3.7a) into Eq. (3.11), we obtain the normalized output probe field intensity from the CMM resonator as

$$T = |t_p|^2 = \left|\frac{\sqrt{2\eta_a\kappa_1}A_{1+}}{\varepsilon_p} - 1\right|^2. \tag{3.12}$$

In order to numerically simulate the transmitted output probe field spectrum, we use the following experimentally realizable set of parameter values [134, 148]. The degenerate microwave cavities of frequency $\omega_c/2\pi = 7.86$ GHz. The decay rate of the first cavity is $\kappa_1/\pi = 3.35$ MHz. The spin density $\rho = 4.22 \times 10^{27}$ m^{-3} and the diameter of the YIG sphere $D = 25$ μm. It results in 3×10^{16} number of spins

(N_m) present in the YIG sphere. The phonon mode has frequency $\omega_b/2\pi = 11.42$ MHz with decay rate $\kappa_b/\pi = 300$ Hz, and the magnon-phonon coupling strength $g_{mb}/2\pi$ is 1 Hz. The Kittel mode frequency of the YIG sphere is $\omega_m = \gamma_e B_{0,i}$, with gyromagnetic ratio, $\gamma_e/2\pi = 28$ GHz/T and $B_{0,i}$ is the input bias magnetic field amplitude. The magnon decay rate is $\kappa_m = 3.52$ MHz. Magnon-photon coupling strength $g_{ma} = \gamma_e B_{vac}\sqrt{5N_m}/2$ can be controlled by changing the vacuum magnetic field amplitude as $B_{vac} = \sqrt{2\pi\hbar\omega_c/V}$, where V is the volume of the CMM resonator.

3.3 Results

3.3.1 Stability Analysis

Initially we consider the two coupled cavities which are operating under a balanced gain-loss condition ($\kappa_1 = \kappa_2$). The Hamiltonian describing such coupled resonator system ($g_{ma} = g_{mb} = 0$) can be written as

$$H_{cav} = \hbar(\Delta_a - i\kappa_1)\delta a_1^\dagger \delta a_1 + \hbar(\Delta_a + i\kappa_1)\delta a_2^\dagger \delta a_2 + \hbar J(\delta a_1^\dagger \delta a_2 + \delta a_2^\dagger \delta a_1). \quad (3.13)$$

The eigenvalues of H_{cav} are $\lambda_\pm = \Delta_a \pm \sqrt{J^2 - \kappa_1^2}$. Note that the above Hamiltonian remains invariant under the simultaneous parity $\mathcal{P} : a_1 \leftrightarrow a_2$ and time-reversal operation $\mathcal{T} : i \rightarrow -i$ operations, and, its eigenvalues are entirely real and complex for $J > \kappa_1$ and $J < \kappa_1$. The point $J = \kappa_1$, which marks this transition from $\mathcal{PT}$ symmetric to the $\mathcal{PT}$ breaking phase, is known as the exceptional point (EP). One must understand the competitive behaviour between the inter-cavity field coupling and the loss/gain rates to get insight into this transition. For $J > \kappa_1$ the intracavity field amplitudes can be coherently exchanged and thus give rise to a coherent oscillation between the field amplitudes. However, for $J < \kappa_1$ the intracavity field can not be transferred to the other one, resulting in a strong field localization or in other words exponential growth. A quick look at Eq. (3.4a) also suggests such gain-induced dynamic instability in a_1 at $J = \kappa_1$ for $\Delta_a = 0$.

The situation becomes more complicated in the presence of magnon-photon coupling. Now, the combined system ($g_{ma}, g_{mb} \neq 0$) ceases to become $\mathcal{PT}$ symmetric. However, the effect of an additional gain cavity ($\kappa_2 > 0$) can be understood by analyzing the stability diagram of the whole system. In the following, we derive the stability condition by invoking the Routh-Hurwitz criterion which requires all the eigenvalues of H_{eff} have negative real parts. The magenta region of Figure 3.2 suggests that when g_{ma} is small the instability threshold remains close to the $J = \kappa_1$ (the conventional EP for a binary $\mathcal{PT}$ symmetric system). However, with increasing g_{ma} the system reaches instability at a larger exchange interaction J. Such a restriction over the choice of the photon exchange rate parameter J will be followed throughout this work, provided the linearized approximation of each operator holds good. To ensure the linear approximation, we numerically solve Eq. (3.5a)-(3.5d) by invoking the Runge-kutta fourth-order method with all the initial fluctuation values to be zero and focusing on the passive cavity field's fluctuation value (δa_1). To study the effect of photon exchange interaction on the intensity of fluctuation,

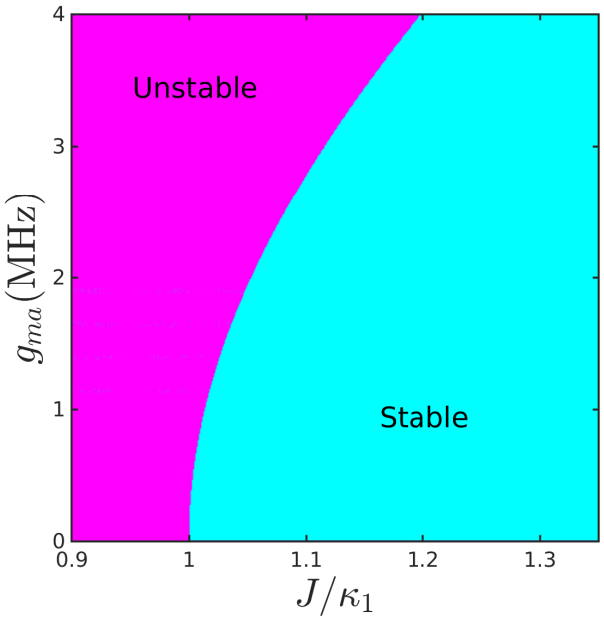

Figure 3.2: The stable and unstable regions are determined as a function of normalized evanescent coupling strength (J/κ_1) and the cavity-magnon coupling strength (g_{ma}) when the loss of the CMM-resonator is perfectly balanced by the gain of the auxiliary cavity ($\kappa_1 = \kappa_2$). We consider the control field intensity to be 10 mW. The other parameters are $\omega_c = 2\pi \times 7.86$ GHz, $\omega_b = 2\pi \times 11.42$ MHz, $\Delta_a = \Delta'_m = \omega_b = 2\pi \times 11.42$ MHz, $\kappa_1 = \kappa_2 = \pi \times 3.35$ MHz, $\kappa_m = \pi \times 1.12$ MHz, $\kappa_b = \pi \times 300$ Hz, and $g_{mb} = 2\pi$ Hz.

we define the following figure of merit as

$$f_c = \left(\frac{\delta a_1^\dagger \delta a_1}{a_{1s}^* a_{1s}} \times 100 \right) \%. \tag{3.14}$$

For $J = 1.30\ \kappa_1$, the intensity of fluctuation in the passive resonator is around 0.01% of its steady-state photon intensity, as shown by the black solid curve of Figure 3.3. Reducing the photon hopping interaction strength enhances the intensity of fluctuation. Finally, at $J = 1.07\ \kappa_1$, we obtain f_c as 0.22% as presented by the blue-dot-dashed curve. Hence, our analysis validates the linearization technique when both microwave cavities operate under balanced gain-loss condition.

3.3.2 Absorption and dispersion spectrum

The magnomechanical system under consideration corresponds to the level diagram of Figure 3.4. Application of a probe field excites the passive cavity mode and allows the transition between $|1\rangle$ and $|2\rangle$. The exchange interaction, J, couples two degenerate excited states $|2\rangle$ and $|5\rangle$. The presence of the magnon-photon coupling distributes the population between the two states $|2\rangle$ and $|3\rangle$. The magnon-phonon

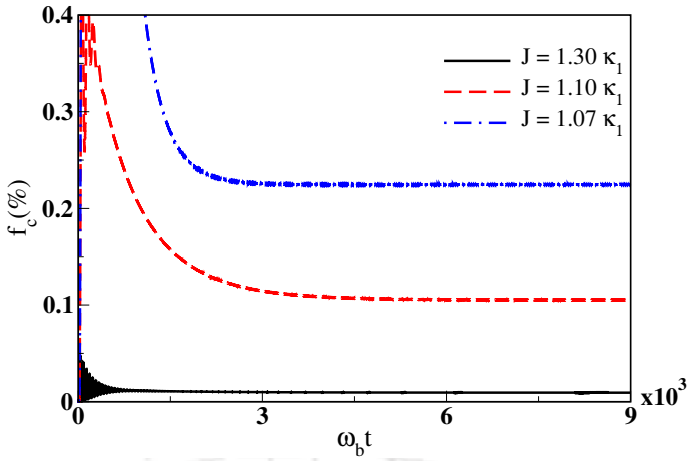

Figure 3.3: The ratio of the noise intensity (of the passive resonator) with respect to the steady-state field intensity (of the passive resonator) is plotted as a function of normalized time under the magnomechanical resonance condition ($\delta = \omega_b$). We consider the control and the probe field intensity to be 10 mW and 10 nW, respectively. All the other parameters are the same as Figure 3.2.

coupling, g_{mb}, couples both the metastable ground states $|3\rangle$ and $|4\rangle$. Here, we consider both the microwave cavities to be passive ($\kappa_2 < 0$) under a weak magnon-photon coupling strength, g_{ma}. In this situation, the magnon-photon hybridization is insignificant. The absorptive and dispersive response can be quantified by the real and imaginary components of $(t_p + 1)$ that will be presented as α and β, respectively. In Figure 3.5(a), we present the absorptive response of the system as a function of normalized probe detuning. The black-solid curve depicts a broad absorption spectrum of the probe field when the exchange interaction is much weaker than the cavity decay rate. One can explain it by considering the level diagram

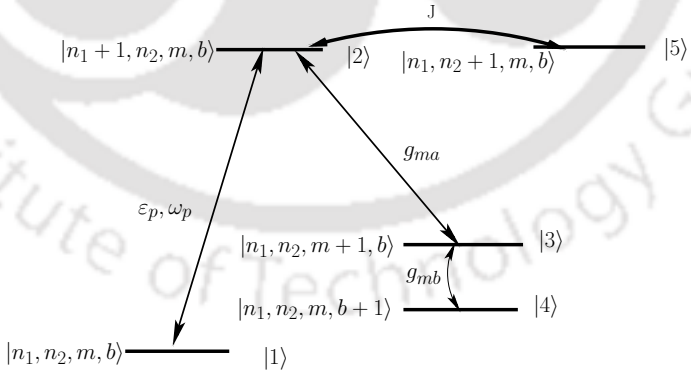

Figure 3.4: Level diagram of the model system. $|n_i\rangle$,$|m\rangle$ and $|b\rangle$ represents the photon number state of i^{th} cavity, magnon mode and phonon mode, respectively. The presence of a weak probe field increases the photon number of CMM resonator by unity. The magnon-photon interaction couples $|n_1 + 1, n_2, m, b\rangle$ and $|n_1, n_2, m + 1, b\rangle$. Whereas g_{mb} couples $|n_1, n_2, m + 1, b\rangle$ and $|n_1, n_2, m, b + 1\rangle$. The hopping interaction between the two cavities directly couples $|n_1 + 1, n_2, m, b\rangle \leftrightarrow |n_1, n_2 + 1, m, b\rangle$.

of Figure 3.4, where the initial population stays in the ground state $|1\rangle$. Applying

a probe field transfers the population from the ground state to the excited state, $|2\rangle$. In addition, the weak magnon-photon coupling (with respect to κ_1) restricts a significant transition from $|2\rangle$ to $|3\rangle$. As a result, it allows the transfer of a fraction of the excited state's population by invoking the exchange interaction J. The

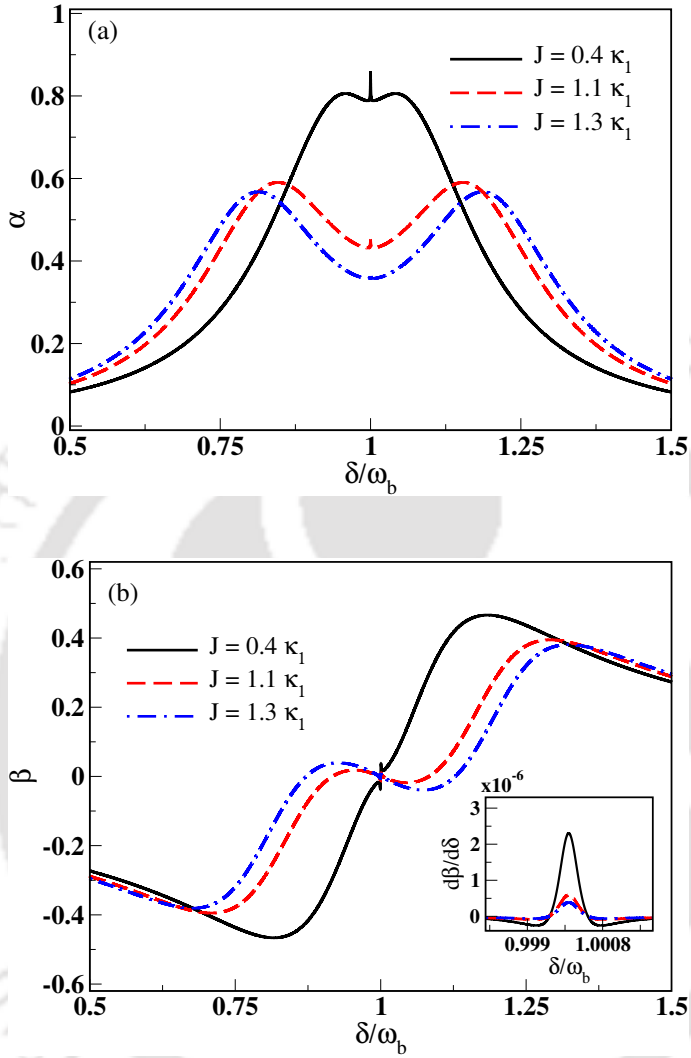

Figure 3.5: (a) Absorption and (b) dispersion spectrum of the model system. The slope of the dispersion curve is shown in the inset. Here we consider both the microwave cavities are passive, with identical decay rates ($\kappa_1 = -\kappa_2$). The magnon-photon couplong strength, g_{ma} is taken as 2 MHz. All the other parameters are the same as in Figure 3.2.

increase in the exchange interaction strength causes a gradual decrease in $|2\rangle$'s population. It reduces the absorption coefficient around the resonance condition except for $\delta = \omega_b$. This phenomenon is shown by the red-dashed and the blue-dot-dashed curve of Figure 3.5(a). We observe a narrow absorption peak inside the broad absorption peak for $J = 0.4\ \kappa_1$. The sharp absorption peak, exactly at $\delta = \omega_b$, occurs due to the magnomechanical resonance. Further increasing the exchange interaction virtually cuts off the population distribution from $|2\rangle$ to $|3\rangle$. As a result, the effect of magnon-phonon resonance also decreases, and the absorption peak at $\delta = \omega_b$ eventually diminishes. In Figure 3.5(b), we present the dispersion spectrum as a

function of normalized detuning δ/ω_b. For the time being, we neglect the effect of magnomechanical coupling and observe the occurrence of anomalous dispersion around $\delta = \omega_b$ for $J = 0.4\ \kappa_1$. Further, increasing the exchange interaction strength more significant than the cavity decay rate can alter the dispersive response from anomalous to normal, as shown by the red-dashed and blue-dot-dashed curves. In the inset of Figure 3.5(b), we plot the slope of the temporal dispersion $d\beta/d\delta$ at the extreme vicinity of the magnon-phonon resonance condition. The positive values of the slope of the temporal dispersion signify anomalous dispersion due to the magnomechanical coupling. However, the steepness of the dispersion curve can be reduced by increasing the exchange interaction strength, as shown by the red-dashed and blue-dot-dashed curves. Note that this dispersion curve is accompanied by absorption. Output transmission of the probe field is prohibited in the presence of huge absorption. Therefore, reducing absorption or introducing the gain to the system is mandatory for observing the group velocity phenomena.

To achieve reasonable transmission at the output, we replace the auxiliary passive

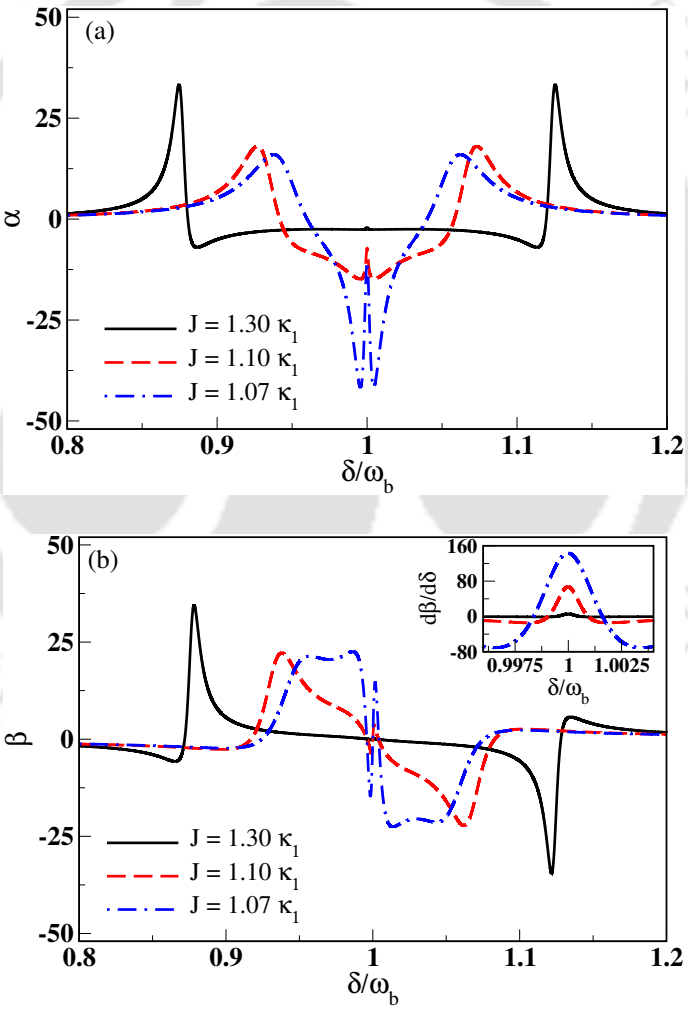

Figure 3.6: (a) Absorption and (b) dispersion spectrum of the model system. The slope of the dispersion curve is shown in the inset. Here we consider the second cavity as a gain cavity, with $\kappa_2 = \kappa_1$. All the other parameters are the same as in Figure 3.2.

cavity with an active one where the second cavity's gain ($\kappa_2 > 0$) completely balances

the first cavity's loss. In this scenario, the stability criterion for the hybrid system allows us to consider the exchange interaction strength J to be greater than 1.053 κ_1 for $g_{ma} = 2$ MHz. We present the absorptive response of the model system in Figure 3.6(a). The black solid curve of Figure 3.6(a) illustrates the occurrence of a double absorption peak spectrally separated by a broad gain regime. The graphical nature is determined by the roots of $D(\delta)$, which are, in general, complex. The real parts of the roots determine the spectral peak position, and the imaginary parts correspond to their widths. To illustrate this, we consider $J = 1.30\ \kappa_1$ with all other parameters remaining the same as earlier. The real parts of the root of $D(\delta)$ present two distinct normal mode positions at δ/ω_b values 0.88 and 1.12. The other two normal modes are spectrally located at the same position $\delta/\omega_b = 1$. The interference between these two normal modes becomes significant while approaching the stability bound as depicted by the red dashed and blue dot-dashed curve of Figure 3.6(a). In turn, it reduces the overall gain of the composite system. Further, we investigate the effect of a gain-assisted auxiliary cavity on the medium's dispersive response in Figure 3.6(b). For $J = 1.30\ \kappa_1$, the two absorption peaks produce two distinct anomalous dispersion regions separated by a broad normal dispersive window. Weakening the exchange interaction strength reveals prominent normal dispersion around the resonance condition except for $\delta = \omega_b$, and the window shrinks. In the inset of Figure 3.6(b), we present the slope of the dispersive response due to the magnomechanical resonance. The black solid curve of Figure 3.6(b) suggests the occurrence of anomalous dispersion at the magnon-phonon resonance condition. Moreover, one can increase the steepness of the dispersion curve by simply approaching the instability threshold, as delineated by the red-dashed and blue-dotted-dashed curve of the inset of Figure 3.6(b). In the consecutive section, we will discuss how the change in the dispersion curve can produce controllable group velocity of the light pulses through the medium and investigate the role of the exchange interaction.

3.3.3 Output probe transmission

The output probe intensity from the system depends on its absorptive response. The equation of Eq. (3.12) dictates the transmission of the probe field and is presented in Figure 3.7. For Figure 3.7(a), we consider both the microwave cavities as passive ones with identical decay rates, *i.e.,* $\kappa_1 = -\kappa_2$. The black solid curve shows a broad absorptive response for $J = 0.40\ \kappa_1$. Increasing the exchange interaction strength causes gradual enhancement in the output probe transmission, as delineated by the red-dashed and blue dot-dashed curve of Figure 3.7(a), and the absorption window splits into two parts. The inset of Figure 3.7(a) suggests the presence of extremely weak transmission dip exactly at $\delta = \omega_b$ for all the three exchange interaction strengths under consideration. In Figure 3.7(b), we present the advantage of using a gain-assisted auxiliary cavity along with a CMM resonator to obtain a controllable amplification of the output probe field. We begin our discussion considering the photon hopping interaction, $J = 1.30\ \kappa_1$. The black solid curve of Figure 3.7(b) estimates the normalized probe transmission of 6.03. Here the normalization is done with respect to the input probe field intensity. By decreasing the parameter J, we approach the unstable region and observe the occurrence of a double transmission peak separated by a sharp and narrow transmission dip. The amplitude of the double transmission peak demonstrates the probe pulse amplifi-

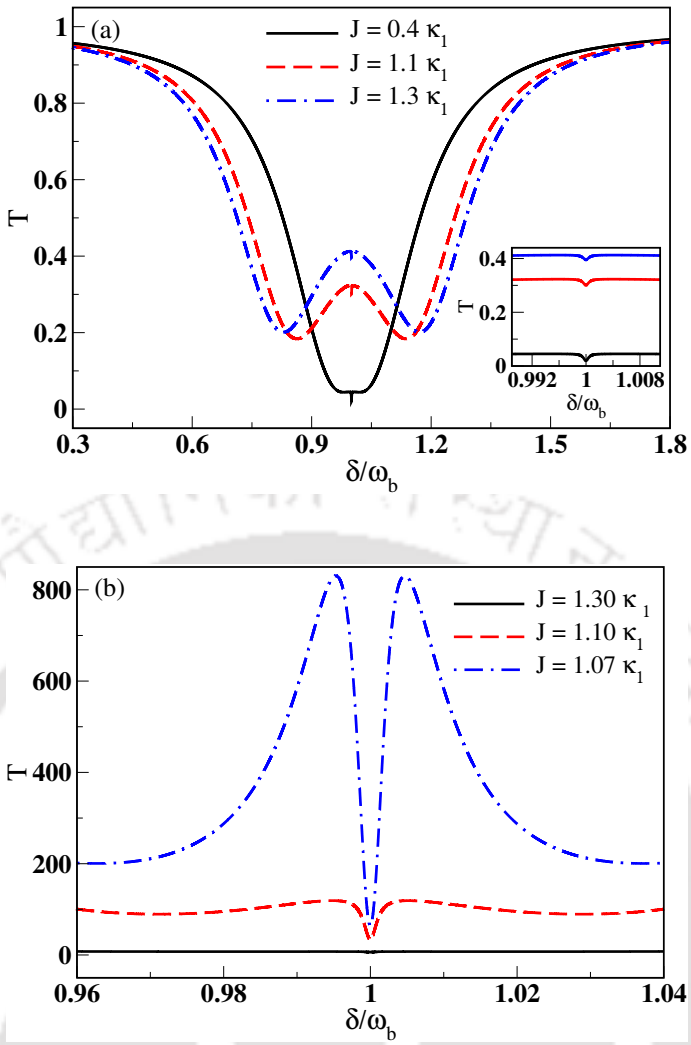

Figure 3.7: Exchange interaction-dependent normalized output probe transmission is plotted as a function of normalized detuning between the control and the probe field when (a) both the cavities are passive ones, in the inset we present the same quantity at the extreme vicinity of the magnomechanical resonance, and (b) one is active and another one is passive. All the other parameters are taken the same as in Figure 3.2.

cation by a factor of 830, as presented by the blue dotted-dashed curve. However, an explicit observation suggests the output probe field amplification by a factor of 67 at the resonance condition $\delta = \omega_b$. Now, to understand the reason behind the probe field amplification, we look closely at the functional form of Eq. (3.12) and note the presence of the parameter Γ_2 in the denominator. Particularly at the magnomechanical resonance condition, it reduces to the condition for $\mathcal{PT}$-symmetry breaking transition for a binary gain-loss cavity system. By approaching the instability threshold, it reduces the denominator of Eq. (3.12) rapidly as compared to the numerator, and the output probe field intensity amplifies as presented in Figure 3.8. Further, we plot the amplitude of the magnomechanical coupling strength ($|G|$) as a function of J. By approaching the instability threshold causes an insignificant decrease in $|G|$, as shown in the inset of Figure 3.8. It also infers that under balanced gain-loss condition, the steady-state field amplitudes corresponding to the passive

cavity, active cavity, and magnon modes do not vary significantly by approaching the instability threshold.

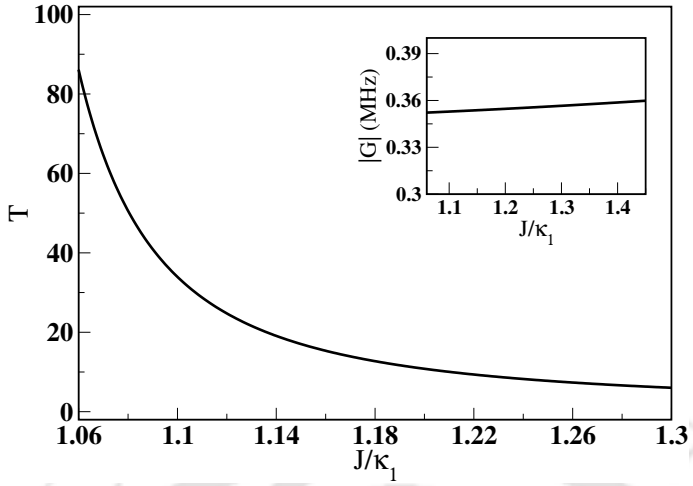

Figure 3.8: The output probe transmission response at $\delta = \omega_b$ is presented as a function of J. In the inset the enhanced magnon-phonon coupling strength is plotted as a function of photon exchange interaction strength. All the other parameters are the same as in Figure 3.2.

3.3.4 Group delay

Controllable group delay has gained much attention due to its potential application in quantum information processing and communication. The dispersive nature of the medium is the key to controlling the group delay of the light pulse under the assumption of low absorption or gain. The pulse with finite width in the time domain is produced by superposing several independent waves with different frequencies centered around a carrier frequency (ω_s). The difference in time between free space propagation and a medium propagation for the same length can create a group delay. The envelope of the input optical pulse is considered as

$$f(t_0) = \int_{-\infty}^{\infty} \tilde{f}(\omega) e^{-i\omega t_0} d\omega,$$

where $\tilde{f}(\omega)$ corresponds to the envelope function in the frequency domain. Accordingly, the reflected output probe pulse can be expressed as

$$f^R(t_0) = \int_{-\infty}^{\infty} t_p(\omega)\tilde{f}(\omega) e^{-i\omega t_0} d\omega, \tag{3.15}$$

$$= t_p(\omega_s) e^{-i\omega_s \tau_g} f(t_0 - \tau_g). \tag{3.16}$$

This expression can be obtained by expanding $t_p(\omega_s + \delta)$ in the vicinity of ω_s by a Taylor series and keeping the terms upto first order in δ. Probe pulse propagation delay is obtained by [102, 149]

$$\tau_g = \mathrm{Re}\left[\frac{-i}{t_p(\omega_s)}\left(\frac{dt_p}{d\omega}\right)\Big|_{\omega_s}\right], \tag{3.17}$$

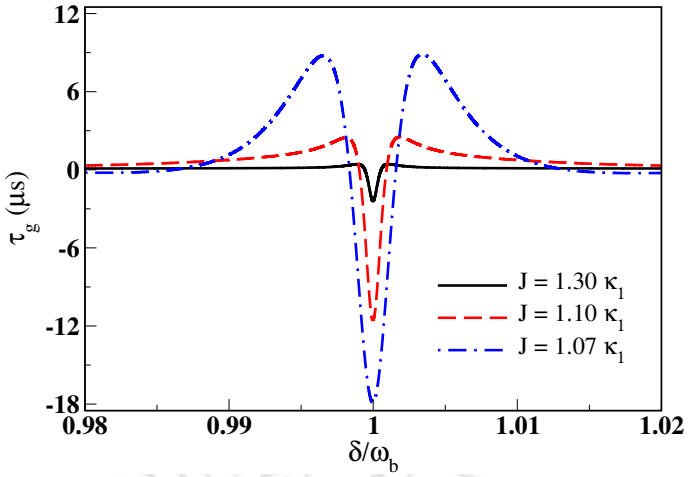

Figure 3.9: Time delay of the probe pulse for different evanescent coupling strength J have been plotted against the normalized probe detuning δ/ω_b, while the control power is 10 mW. All other parameters are taken as the same as in Figure 3.2.

which can be further simplified as

$$\tau_g = \frac{(\alpha(\omega_s)-1)\frac{d\beta}{d\omega}\Big|_{\omega_s} - \beta(\omega_s)\frac{d\alpha}{d\omega}\Big|_{\omega_s}}{|t_p(\omega_s)|^2}. \tag{3.18}$$

From Eq. (3.18), the slope of the medium's absorption and dispersion curves determine the probe pulse propagation delay or advancement. However, Figure 3.6(b) suggests that the value of β is negligibly small near the magnomechanical resonance. Hence, the group delay depends on the first term of the numerator of Eq. (3.18). In Figure 3.9, we examine the effect of photon-photon exchange interaction on the probe pulse propagation delay when both cavities operate under balanced gain-loss

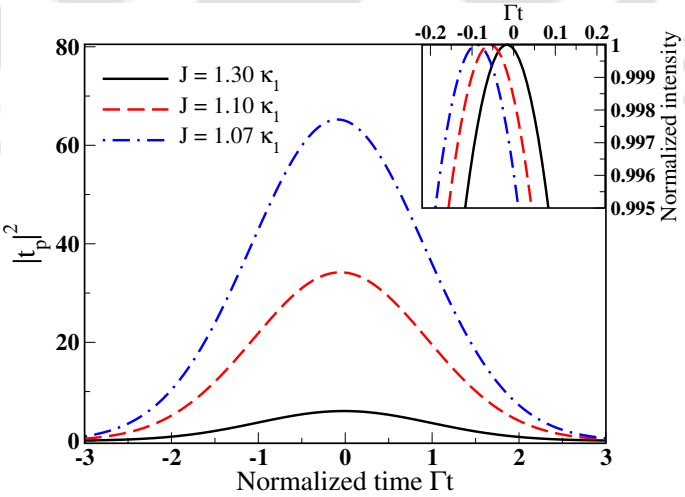

Figure 3.10: The relative intensity of the output probe pulse is plotted against the normalized time (Γt) for different photon-photon exchange interaction strengths when both cavities are operating under balanced gain-loss condition. The input probe pulse width, Γ is taken as 7.17 kHz. All the other parameters are the same as in Figure 3.2.

condition. The system produces anomalous dispersion accompanied by a gain response. The black solid curve of Figure 3.9 depicts the probe pulse advancement of 2.4 μs for the photon hopping interaction strength, $J = 1.3\ \kappa_1$. Moreover, one can enhance the effective gain and the slope of the anomalous dispersion curve by approaching the instability threshold. That, in turn, brings out the superluminosity of the output probe pulse, characterized by the advancement of 17.9 μs as shown by the blue dotted-dashed curve of Figure 3.9.

To verify the above results, we consider a Gaussian probe pulse with a finite width around the resonance condition, *i.e.,* $\delta = \omega_b$, and numerically integrate it by using Eq. (3.15). The shape of the input envelope is considered as,

$$\tilde{f}(\omega) = \frac{\varepsilon_p}{\sqrt{\pi\Gamma^2}} e^{-\frac{(\omega-\omega_s)^2}{\Gamma^2}}, \tag{3.19}$$

where Γ is the spectral width of the optical pulse. We consider Γ to be 7.17 kHz, such that the Gaussian envelope is well-contained inside the gain-window around the resonance condition ($\delta = \omega_b$), as depicted in Figure 3.6(a). The dispersive, absorptive as well as gain response of the system can be demonstrated by examining the effect of the probe transmission coefficient (t_p) on the shape of the input envelope. The gain of the auxiliary cavity manipulates the probe transmission coefficient in such a way that it amplifies the intensity of the output probe pulse. The black solid curve depicts the output probe pulse amplification of 6.2 for photon-hopping interaction strength, $J = 1.30\ \kappa_1$. A decrease in the J value gradually enhances the effective gain in the system. It amplifies the output probe transmission as presented by the red dashed and blue dotted-dashed curves of Figure 3.10. We observe that the output field amplification can reach to a factor of 65.3 while considering the exchange interaction strength to be 1.07 κ_1. Further decreasing the exchange interaction will lead to dynamical instability in our model system. Interestingly, the temporal width of the probe pulse is almost unaltered during the propagation through the magnon-assisted double cavity system. This numerical result agrees with our analytical results for the output probe transmission, as shown in Figure 3.7(b). Moreover, the importance of the photon-photon exchange interaction on the probe pulse propagation advancement can be observed from the inset of Figure 3.10. The peak separation between the input pulse ($t = 0$) and the output pulse for $J = 1.30\ \kappa_1$ estimates the probe pulse advancement of 2.34 μs. The red dashed, and blue dashed-dotted curve of the inset estimates the probe pulse advancement of 8.75 μs and 13.30 μs for $J = 1.10\ \kappa_1$ and 1.07 κ_1, respectively.

3.4 Conclusion

In conclusion, we have theoretically investigated the controllable output field transmission from a critically coupled cavity magnomechanical system. We drive the first cavity with a YIG sphere inside it, establishing the magnon-photon coupling. The photon exchange interaction connects the second microwave cavity with the first. An external magnetic field induces the deformation effect of the YIG sphere. In this work, the interaction between the magnon and photon modes lies under the weak coupling regime. The medium becomes highly absorbent when both cavities are passive, and the output probe transmission is prohibited. We introduce a gain

to the auxiliary cavity to overcome this situation. It is noteworthy that the instability threshold must be close to the conventional exceptional point for a binary $\mathcal{PT}$-symmetric system. At the magnomechanical resonance, the auxiliary cavity produces an effective gain associated with anomalous dispersion. Further, decreasing the photon exchange interaction strength causes gradual enhancement of the effective gain and the steepness of the dispersion spectrum. As a result, we observe a controllable superluminal microwave pulse propagation associated with amplification by a factor of 67. By studying the propagation dynamics of a Gaussian probe pulse of width 7.17 kHz, we confirm that the numerical study is consistent with the analytical results. Our study may find potential applications in weak signal sensing and communication purposes in the newly emerging field of cavity magnomechanics.

Chapter 4

Hybrid Rotational Cavity Optomechanics Using Atomic Superfluid in a Ring

4.1 Introduction

Soon after its experimental realization [150, 151], Bose-Einstein condensate (BEC), has emerged as a prominent and controllable system [152] to investigate and mimic the persistent flow of superfluidity [153] and superconductivity [154]. Especially, when confined in multiply-connected geometries (toroidal traps) [155] such systems exhibit persistent currents of superflow [156]. These geometries can provide (i) topological protection to the quantum circulation [157], (ii) longer dissipationless flow [158], and (iii) 'supersonic' rotations [159]. Since the first experimental illustration of atomic persistent currents in annularly-trapped BEC [160, 161], an incredible progress has been made in this configuration to study atomic superflow for the investigation and development of matter-wave interferometry [162], atomtronic circuits [163–165], topological excitations [166, 167], superfluid hydrodynamics [168, 169], phase slips [170, 171], time crystals [172], gyroscopy [173] and cosmological studies [174].

Therefore, in a toroidal geometry, it is very important to determine the atomic circulation which involves the phase (winding number) measurement of a rotational state. For detecting the winding number, the current state-of-the-art technologies involve destructive methods [175], namely, optical absorption imaging of the atoms in the ring which destroys its superfluid character. Furthermore, *in situ* detection in the existing techniques is difficult due to issues related to the optical resolution of the radius of the vortex which demands time-of-flight expansion methods [176].

In recent studies, our group proposed a versatile method to detect the magnitude [177,178] as well as direction [179] of rotation of a bosonic ring condensate with minimal destruction, *in situ* and in times. Specifically, the method uses the tools of cavity optomechanics [180], a unique platform to explore the radiation-pressure interaction of vibrating elements with the photons confined inside an optical resonator. This method not only improves the rotation sensing by three orders of magnitude but also provides a test bed to manipulate the persistent currents by generating the optomechanical entanglement between matter waves.

The aforementioned radiation-pressure interaction plays a dual role in cavity op-

tomechanics. On one side, it assists in manipulating the properties of the mechanically pliable objects for applications such as quantum ground state cooling [29, 64, 181] and generation of entanglement between macroscopic objects [30, 36, 37, 182]. On the other end, it can also be used to control the quantum properties of the light. For instance, optomechanical interactions can generate squeezed states of light where the quantum fluctuations in one of the optical quadratures are reduced below the shot-noise level. This comes with increasing fluctuations in other orthogonal quadrature [38, 39, 183]. Such engineered squeezed light states play a vital role in enhancing displacement sensitivity in kilometer-sized gravitational wave observatories [184, 185], optical communication [186], and metrology [187, 188].

Interestingly, the rotational analog of cavity optomechanics utilizes radiation torque [189] from the angular momentum exchange between the Laguerre-Gaussian (LG) cavity mode and a spiral phase plate as a rotating mirror [190]. Such systems have been investigated to cool the rotational degrees of freedom to their quantum ground state [191] and for the realization of opto-rotational entanglement [192, 193].

Nowadays, hybrid optomechanical systems [194, 195] pave a versatile pathway in the development of quantum technologies [196]. Such systems take into account of a mechanical oscillator interacting with an electromagnetic field [197] and an additional physical system [198] or a degree of freedom [199]. In this paper, we present a hybrid setup formed by confining an annularly trapped BEC inside a LG cavity. The spiral phase elements serve as the end mirrors of the cavity such that one mirror rotates about the cavity axis through a clamped support. Specifically, in this hybrid system, we explore (i) ponderomotive squeezing *i.e.,* the reduction of quantum fluctuations of the output optical quadratures below the shot noise level at various frequencies, and (ii) the generation of bipartite and tripartite entanglement between the cavity and the matter waves and the macroscopic rotating mirror. The main advantages of our hybrid setup are: (a) From the perspective of toroidal BEC, the atomic rotation in it provides a distinctive tool to correlate the optical amplitude and phase quadratures and provide squeezing of about 87% at a measurement angle of 7° around the frequencies of the Bragg-scattered sidemodes. On the other hand, an optimum ponderomotive squeezing of 40% below the shot noise level occurs at the angular frequency of the rotating mirror that can further be manipulated by the persistent currents of ring BEC. The same effect also controls the bipartite and tripartite entanglement between the atomic superfluids and the macroscopic object, paving a useful resource for quantum information processing. (b) From the point of view of the LG cavity, it is relatively easy to increase the orbital angular momentum (OAM) of the LG mode. Moreover, in such a cavity setup, the optorotational effects scale with the square of OAM [191] in contrast to the linear scaling of the conventional cavity optomechanics. Using these facts, it is comparatively simple to manipulate the optical interaction of the ring BEC and the rotating mirror with a common LG mode. This in turn can be harnessed to increase the ponderomotive squeezing and the simultaneous existence of bipartite and tripartite entanglements. Our hybrid system can be exploited for applications in sensing and quantum teleportation and represents the first proposal involving matter wave rotation in hybrid optomechanics.

The chapter is organized as follows: In Section. 4.2, the details of the hybrid system is shown. The relevant equations for the quantum dynamics, the bistability and stability analysis are provided in Section. 4.3. Section. 4.4 contains a discussion

on ponderomotive squeezing while Section. 4.5 describes the bipartite and tripartite entanglement in our hybrid setup.The final conclusion of this chapter is given in Section. 4.6.

4.2 Model

The configuration under consideration is a hybrid setup consisting of a ring BEC and an optical cavity. In the following, we provide details of each of these elements.

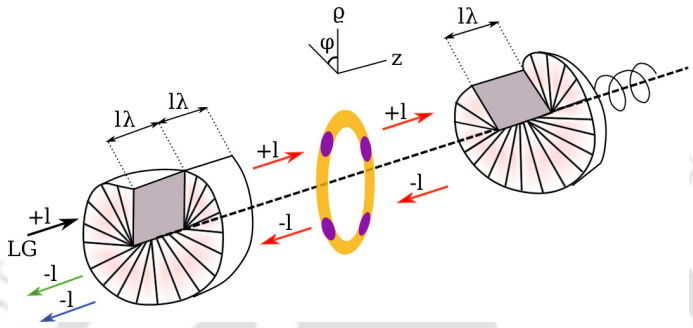

Figure 4.1: Schematic diagram of a hybrid setup consisting of a ring BEC inside a cavity. The cavity comprises two spiral phase elements: one is fixed and partially transmissive, while the other is rotating and highly reflective. The colored arrows show the orbital angular momentum at different positions: The purely extra cavity field, the purely intracavity field, and the intracavity field arising from the intracavity field are green, red, and blue arrows, respectively. The interference between the transmitted and the reflected intracavity fields produces an optical lattice that probes the ring BEC with winding number L_p.

4.2.1 Ring BEC

The first unique ingredient of our hybrid setup is an atomic BEC confined in a ring trap and located inside the optical cavity. In the toroidal trap, the harmonic potential experienced by each condensate atom along the radial (ρ) and axial (z) directions is given by [177]

$$U(\rho, z) = \frac{1}{2} m\omega_\rho \left(\rho - R\right)^2 + \frac{1}{2} m\omega_z z^2 \,, \tag{4.1}$$

where m, ω_ρ (ω_z) and R represent the mass of the condensate atom, harmonic trapping frequency along the radial (axial) direction and radius of the ring trap, respectively. Due to the above potential, we assume that the atomic evolution along radial and axial directions remains unchanged. However, we consider the dynamical evolution along the azimuthal direction, φ, as it is not subjected to any potential. This one-dimensional description is possible to be applied within the current state-of-the-art experiments if the number of atoms N of the condensate obeys the following constraint [200]

$$N < \frac{4R}{3a_{\mathrm{Na}}} \sqrt{\frac{\pi\omega_\rho}{\omega_z}} \,, \tag{4.2}$$

where a_{Na} is the s-wave scattering length of the sodium atoms in the condensate.

4.2.2 Optical Cavity

In our setup, an optical cavity is formed with two spiral phase elements with the same handedness. In this arrangement, the input coupler (IC) is a fixed partially transmissive mirror, and the rear mirror (RM) is perfectly reflective. Now, IC is designed to preserve the OAM of the light while transmitting. On the other hand, it removes OAM of $2l\hbar$ per photon in reflection. The perfect reflection from RM removes $2l\hbar$ angular momentum from each photon. In Figure 4.1, we provide the mode buildup at the various locations along the optic axis for an input Laguerre-Gaussian beam carrying orbital angular momentum $+l\hbar$. With the above design, the radiation torque per photon transferred to RM is written as $\xi_\phi = 2lc\hbar/2L$, where c is the speed of light and L is the cavity length, respectively.

4.3 Quantum Dynamics

4.3.1 Hamiltonian

As described above, the modes carrying OAM $\pm l\hbar$ build up inside the cavity, creating an angular lattice about the cavity axis. From such an optical lattice, some of the condensate atoms get coherently Bragg scattered from a macroscopically occupied rotational state with winding number L_p to states with $L_p \pm 2nl$, with $n = 1, 2, 3, \cdots$. In the following, we consider a dipole potential weaker than the condensate's chemical potential and consider only first-order diffraction, $L_p \to L_p \pm 2l$.

In dimensionless units, the Hamiltonian for our hybrid configuration is expressed as

$$H = H_{\mathrm{BEC}} + H_\phi \, . \tag{4.3}$$

Here, H_{BEC} is one-dimensional Hamiltonian for the azimuthal motion of the ring BEC and is governed by [177]

$$\begin{aligned} H_{\mathrm{BEC}} = \sum_{j=c,d} \left[\frac{\hbar\omega_j}{2} \left(X_j^2 + Y_j^2 \right) + \hbar \left(G X_j + \frac{U_0 N}{2} \right) a^\dagger a \right] \\ + \sum_{j=c,d} 2\hbar\tilde{g}N \Big(X_j^2 + Y_j^2 \Big) + 2\hbar\tilde{g}N \Big(X_c X_d - Y_c Y_d \Big) \, . \end{aligned} \tag{4.4}$$

The first term in the square bracket in Eq. (4.4) denotes the energies of the Bragg-scattered side modes [177] of frequencies $\omega_c = \hbar(L_p + 2l)^2/(2I_a)$ and $\omega_d = \hbar(L_p - 2l)^2/(2I_a)$. The moment of inertia of each atom about the cavity axis is $I_a = mR^2$. The dimensionless position and momentum quadratures are defined as $X_j = \left(j^\dagger + j\right)/\sqrt{2}$ and $Y_j = \left(j - j^\dagger\right)/i\sqrt{2}$, respectively. The second term in the square bracket on the right-hand side of Eq. (4.4) governs the effective optomechanical coupling between the side modes and the optical field with the coupling strength $G = U_0\sqrt{N}/2\sqrt{2}$. Here $U_0 = g_a^2/\Delta_a$ such that g_a gives the interaction between single atom and single photon and Δ_a denotes the atomic detuning. The final two terms arise due to two-body atomic interactions of strength $g = (2\hbar\omega_\rho a_{Na})/R$, which can

be scaled such that $\tilde{g} = g/4\pi\hbar$. Interestingly, from the Bogoliubov analysis, the actual side mode frequencies can be written as $\omega_j' = \sqrt{\omega_j^2 + 4\omega_j \tilde{g} N}$ [201]. However, for the rest of our analysis, we impose $\omega_{c,d} \gg 4\tilde{g}N$ and hence use $\omega_{c,d}' \sim \omega_{c,d}$.

On the other hand, the Hamiltonian for the optical cavity in the rotating frame of the driving laser is governed by

$$H_\phi = -\hbar\Delta_o a^\dagger a + \frac{\hbar\omega_\phi}{2}\left(L_z^2 + \phi^2\right) + \hbar g_\phi a^\dagger a\phi - i\hbar\eta\left(a - a^\dagger\right) , \tag{4.5}$$

where the first two terms describe the free energy of the detuned cavity mode with $\Delta_0 = \omega_l - \omega_0$ and the rotating mirror with resonance frequency ω_ϕ, respectively. Here L_z and ϕ represent the respective dimensionless angular momentum and angular displacement of RM about the cavity axis and these conjugate variables satisfy $[L_z, \phi] = -i$. The third term in Eq. (4.5) governs the radiation torque on RM, giving rise to optorotational coupling given by

$$g_\phi = \frac{cl}{L}\sqrt{\frac{\hbar}{I\omega_\phi}} . \tag{4.6}$$

The moment of inertia of the rotating mirror about the cavity axis is described as $I = MR_m^2/2$, where M (R_m) is the mass (radius) of the RM. Finally, the last term on the right-hand side of Eq. (4.5)represents the cavity drive having amplitude $\eta = \sqrt{P_{in}\gamma_o/(\hbar\omega_o)}$, where P_{in} is the input drive power and γ_o is the cavity linewidth.

Using Eq. (4.3), we derive the Heisenberg equations of motion and include damping and noise appropriately to obtain the following quantum Langevin equations

$$\dot{a} - i\left[\tilde{\Delta} - G\left(X_c + X_d\right) - g_\phi\phi\right]a = -\frac{\gamma_o}{2}a + \eta + \sqrt{\gamma_o}a_{in} , \tag{4.7a}$$

$$\ddot{X}_c + \gamma_m\dot{X}_c + \Omega_c^2 X_c = -\tilde{\omega}_c G a^\dagger a - \mathcal{A}X_d + \Omega_c\epsilon_c , \tag{4.7b}$$

$$\ddot{X}_d + \gamma_m\dot{X}_d + \Omega_d^2 X_d = -\tilde{\omega}_d G a^\dagger a + \mathcal{A}X_c + \Omega_d\epsilon_d , \tag{4.7c}$$

$$\ddot{\phi} + \gamma_\phi\dot{\phi} + \omega_\phi^2\phi = -\omega_\phi g_\phi a^\dagger a + \omega_\phi\epsilon_\phi , \tag{4.7d}$$

where $\tilde{\Delta} = \Delta_o - \frac{U_0 N}{2}$ is the effective cavity detuning and γ_m (γ_ϕ) is the damping of each condensate side mode (RM). Further, we have written the quantities $\Omega_{c,d}^2 = \left(\omega_{c,d} + 4\tilde{g}N\right)^2 - 4\tilde{g}^2N^2$, $\tilde{\omega}_{c,d} = \omega_{c,d} + 2\tilde{g}N$, $\mathcal{A} = 2\tilde{g}N\left(\omega_c - \omega_d\right)$. In the above Heisenberg-Langevin equation, $a_{in}(t)$ represents the vacuum Gaussian noise of average $\langle a_{in}(t)\rangle = 0$, injected into the cavity, and its fluctuations are delta-correlated as

$$\langle \delta a_{in}(t)\delta a_{in}^\dagger(t')\rangle = \delta(t - t') . \tag{4.8}$$

Additionally, ϵ_j ($j = c, d$), and ϵ_ϕ in the quantum Langevin equation describe the Brownian noise in the condensate side modes and the rotating mirror, respectively. Their average values are zero and fluctuations at respective temperatures T_j and T_ϕ obey following correlations

$$\langle \epsilon_j(t)\epsilon_j(t')\rangle = \frac{\gamma_m}{\Omega_j}\int_{-\infty}^{+\infty}\frac{d\omega}{2\pi}e^{-i\omega(t-t')}\omega\left[1 + \coth\frac{\hbar\omega}{2k_BT_j}\right] , \tag{4.9}$$

$$\langle \epsilon_\phi(t)\epsilon_\phi(t')\rangle = \frac{\gamma_\phi}{\omega_\phi}\int_{-\infty}^{+\infty}\frac{d\omega}{2\pi}e^{-i\omega(t-t')}\omega\left[1 + \coth\frac{\hbar\omega}{2k_BT_\phi}\right] , \tag{4.10}$$

where k_B is Boltzmann's constant.

4.3.2 Steady State

Following the linearization approach, each operator $\mathcal{O}(t)$ can be decomposed into its steady-state values $\mathcal{O}_s$ and a small fluctuation $\delta\mathcal{O}(t)$. The steady-state values of each operator are

$$a_s = \frac{\eta}{\sqrt{\Delta'^2 + \left(\frac{\gamma_o}{2}\right)^2}}\,, \tag{4.11a}$$

$$X_{cs} = -\tilde{\Omega}_c G a_s^2\,, \tag{4.11b}$$

$$X_{ds} = -\tilde{\Omega}_d G a_s^2\,, \tag{4.11c}$$

$$\phi_s = -\frac{g_\phi}{\omega_\phi} a_s^2\,, \tag{4.11d}$$

where modified cavity detuning is given by $\Delta' = \tilde{\Delta} + \tilde{\Omega} G^2 a_s^2 + \frac{g_\phi^2}{\omega_\phi} a_s^2$ and $\tilde{\Omega} = \tilde{\Omega}_c + \tilde{\Omega}_d$, such that $\tilde{\Omega}_{c,d} = \left(\tilde{\omega}_{c,d}\Omega_{d,c}^2 \mp \tilde{\omega}_{d,c}\mathcal{A}\right) / \left(\mathcal{A}^2 + \Omega_c^2\Omega_d^2\right)$. Here the phase of the cavity drive is chosen such that a_s is real. When the effective cavity detuning is larger than the critical value, $\tilde{\Delta}_{cr} = -\sqrt{3}\gamma_0/2$, the above steady-state solution of $|a_s|^2$ manifests a bistable response concerning the input drive field intensity as depicted in Figure 4.2(a). Additionally Figure 4.2(b) suggests the input drive field intensity ($P_{in} > P_{cr}$) can lead to the bistability response in $|a_s|^2$ where the critical power is $P_{cr} = \hbar\omega_0\gamma_0^2/3\sqrt{3}\left(\tilde{\Omega}G^2 + g_\phi^2/\omega_\phi\right)$. In the remainder of the paper, we choose the parameters to avoid the bistable regime and keep our system monostable. This can also be achieved by using electronic feedback [202, 203], which allows us to choose the modified detuning, Δ', independently of the radiation pressure.

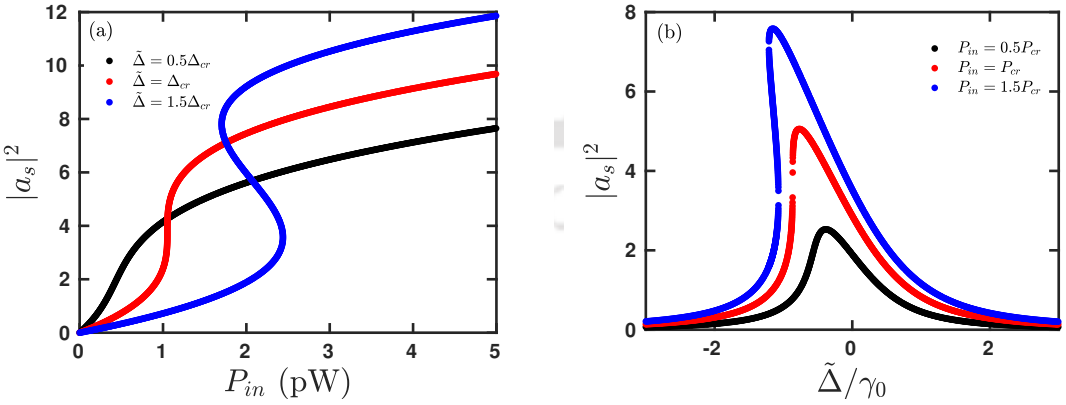

Figure 4.2: Bistability plot as a function of (a) input power and (b) cavity detuning. Here $\tilde{\Delta}_{\rm cr}/2\pi = -0.17$ MHz, and $P_{\rm cr} = 1$ pW. The parameters used are $R = 12$ μm, $N = 10^4$, $\omega_\rho/2\pi = \omega_z/2\pi = 840$ Hz, $\gamma_o/2\pi = 0.2$ MHz, $\Delta_a/2\pi = 5.4$ GHz, $g_a/2\pi = 0.7$ MHz, $U_0/2\pi = 90.7$ Hz, $L_p = 1$, $l = 10$, $G/2\pi = 3.2$ kHz, $\gamma_m/2\pi = 0.8$ Hz, $\omega_o/2\pi = 10^{15}$ Hz, $a_{\rm Na} = 0.1$ nm, $\tilde{g} = 14\tilde{g}_m$, $\tilde{g}_m/2\pi = 78.8$ μHz, $L = 4$ mm, $M = 3.08$ μg, $\omega_\phi/2\pi = 653$ Hz, $\gamma_\phi = 0.1\gamma_m$, and $R_m = 15$ μm.

4.3.3 Stability Analysis

The fluctuation part of Eq. (4.7a)-(4.7d) can be expressed as a set of linearized equations

$$\dot{u}(t) = \tilde{F}u(t) + v(t) \ , \tag{4.12}$$

where the fluctuation vector $u(t) = (\delta X_c(t), \delta Y_c(t), \delta X_d(t), \delta Y_d(t), \delta Q(t), \delta P(t), \delta\phi(t), \delta L_z(t))^T$ and the input noise vector $v(t) = \left(0, \epsilon_c(t), 0, \epsilon_d(t), \sqrt{\gamma_0}\delta Q_{in}(t), \sqrt{\gamma_0}\delta P_{in}(t), 0, \epsilon_\phi(t)\right)^T$, respectively. We have expressed the cavity field fluctuations in terms of their amplitude and phase quadratures as $\delta Q = (\delta a + \delta a^\dagger)/\sqrt{2}$, and $\delta P = -i\left(\delta a - \delta a^\dagger\right)/\sqrt{2}$. The explicit form of the drift matrix $\tilde{F}$ is given by

$$\tilde{F} = \begin{pmatrix} 0 & \Omega_c & 0 & 0 & 0 & 0 & 0 & 0 \\ -\Omega_c & -\gamma_m & -\frac{\mathcal{A}}{\Omega_c} & 0 & -\frac{\tilde{\omega}_c G_r}{\Omega_c} & 0 & 0 & 0 \\ 0 & 0 & 0 & \Omega_d & 0 & 0 & 0 & 0 \\ \frac{\mathcal{A}}{\Omega_d} & 0 & -\Omega_d & -\gamma_m & -\frac{\tilde{\omega}_d G_r}{\Omega_d} & 0 & 0 & 0 \\ 0 & 0 & 0 & 0 & -\frac{\gamma_o}{2} & -\Delta' & 0 & 0 \\ -G_r & 0 & -G_r & 0 & \Delta' & -\frac{\gamma_o}{2} & -g_\phi^r & 0 \\ 0 & 0 & 0 & 0 & 0 & 0 & 0 & \omega_\phi \\ 0 & 0 & 0 & 0 & -g_\phi^r & 0 & -\omega_\phi & -\gamma_\phi \end{pmatrix} . \tag{4.13}$$

The enhanced side modes-cavity coupling strength and optorotational coupling are described as $G_r = \sqrt{2}Ga_s$, and $g_\phi^r = \sqrt{2}g_\phi a_s$, respectively. We derive the stability condition for the hybrid rotational cavity optomechanical system by invoking the Routh-Hurwitz criterion [204], which suggests all the eigenvalues of $\tilde{F}$ must have negative real parts. From Figure 4.3, it is evident that our system lies in the stable region for the weaker single photon optorotational coupling strength with respect to the side mode-cavity coupling strength. Moreover, increasing g_ϕ results gradual decrease in the characteristics frequency bound of the RM.

4.4 Ponderomotive Squeezing

In this section, we analyze the hybrid system to manipulate the quantum properties of the output light. Our interest, in particular, is to reduce the quantum fluctuations in the optical quadratures well below the shot noise level and to describe the influence of quantum circulation on the optical squeezing.

4.4.1 Quadrature Noise Spectrum

To describe the ponderomotive squeezing, we invoke the homodyne measurement technique and obtain the quadrature noise spectrum of the output optical field. The homodyne-detected signal can be expressed as [39, 205]

$$Q_\theta^{out}(\omega) = Q_{out}(\omega)\cos\theta + P_{out}(\omega)\sin\theta \ , \tag{4.14}$$

where θ determines the measured field quadrature and is adjusted experimentally. The cavity relates the output and input field quadratures as $Q_{out}(\omega) = \sqrt{\gamma_o}\delta Q(\omega) -$

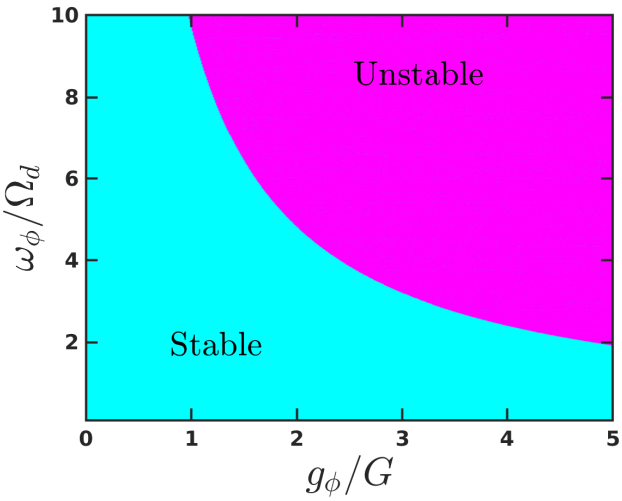

Figure 4.3: The stable and unstable regions are determined as functions of the normalized optorotational coupling g_ϕ/G and the normalized frequency of the rotating mirror ω_ϕ/Ω_d. We consider $\Delta^{'} = \omega_\phi$, $P_{\rm in} = 12.4$ fW. The other parameters are the same as in Figure 4.2.

$Q_{in}(\omega)$, and $P_{out}(\omega) = \sqrt{\gamma_o}\delta P(\omega) - P_{in}(\omega)$. The output quadrature noise spectrum is then calculated as

$$\begin{aligned} S(\omega) = {} & |\xi_1(\omega)|^2 + |\xi_2(\omega)|^2 + i\left[\xi_1^*(\omega)\xi_2(\omega) - \xi_2^*(\omega)\xi_1(\omega)\right] \\ & - 2\gamma_m\omega\left[\frac{|\xi_3(\omega)|^2}{\Omega_c} + \frac{|\xi_4(\omega)|^2}{\Omega_d}\right]\left[1 - \coth\left(\frac{\hbar\omega}{2k_BT}\right)\right] \\ & - 2\frac{\gamma_\phi\omega}{\omega_\phi}|\xi_5(\omega)|^2\left[1 - \coth\left(\frac{\hbar\omega}{2k_BT_\phi}\right)\right]. \end{aligned} \tag{4.15}$$

A full derivation of the above spectrum and detailed expressions of ξ_i's are given in Appendix A.1. Note that the noise spectrum in Eq. (4.15) is normalized in such a way that $S(\omega) = 1$ represents a shot-noise level [38].

In Figure 4.4, we show the power spectral density (PSD) of the optical quadrature as a function of the response frequency for different homodyne measurement angles. Here the black dotted curve represents the shot noise level. For $\theta = 90^\circ$, the phase quadrature of the output optical field results in three Lorentzian peaks on top of the shot noise background at the characteristic frequencies, $\Omega_d/2\pi \sim 595$ Hz, and $\Omega_c/2\pi \sim 717$ Hz corresponding to side modes of the rotating BEC, and the rotating mirror, $\omega_\phi/2\pi \sim 653$ Hz, respectively. It is evident that the fluctuations remain above the vacuum noise in this scenario. However, decreasing the measurement angle θ reduces the value of $S(\omega)$ well below the shot noise level near the atomic side mode frequencies as presented by the blue dot-dashed curve of Figure 4.4(a). It is a clear signature of the ponderomotive squeezing which occurs due to the existence

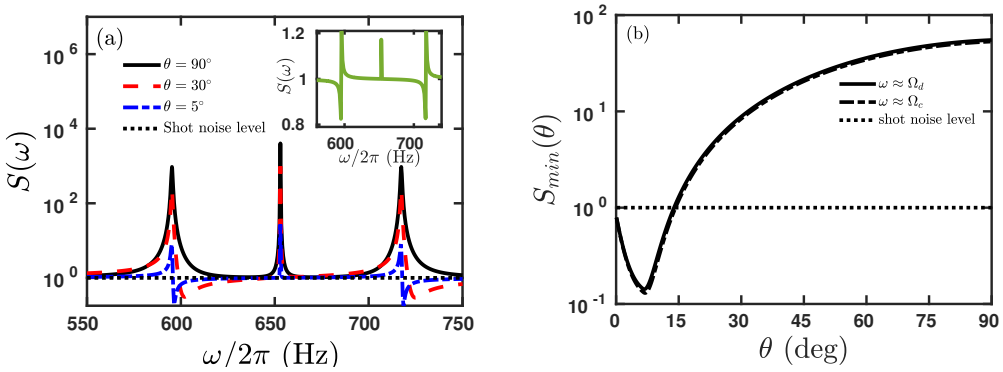

Figure 4.4: (a) Power spectral density (PSD) of the output optical quadrature as a function of the response frequency $\omega/2\pi$, for the measurement angles $\theta = 90°$ (black solid line), $\theta = 30°$ (red dashed line), and $\theta = 5°$ (blue dot-dashed line). (b) PSDs as a function of the measurement angle θ. Black solid, and black dot-dashed curves are produced by fixing the response frequency near Ω_d and Ω_c, respectively. Also, in these plots the spectrum is normalized to the shot noise (black dotted line). Parameters used are $T = 10$ nK, $T_\phi = 1$ mK and other parameters are same as in Figure 4.3.

of correlations between optical amplitude and phase quadratures. For instance, at a measurement angle, $\theta = 5°$, the output optical noise is reduced by 84% below the shot noise within a bandwidth of 20 Hz around $\omega = \Omega_c, \Omega_d$ and the amplitude quadratures become asymmetric like the Fano lineshape [206]. Such a line profile arises due to the interference effects generated by the optical quadratures and the resonant process produced by the atomic density modulation driven by amplitude quadrature [207]. In Figure 4.4(a), we set the effective cavity detuning equal to ω_ϕ. As a result, the correlation between amplitude and phase quadratures of the input field produces a small squeezing at $\theta = 0°$ [205], as shown in the inset of Figure 4.4(a).

As discussed above, the measurement angle during the homodyne detection plays a crucial role to reduce the spectral noise below the shot noise. Now, in Figure 4.4(b), we display the PSD by tuning the measurement angle in the range $[0, 180°]$ by fixing the response frequencies around the mechanical side modes . For our parameters, the maximum noise reduction near the mechanical side mode frequencies occurs around $\theta = 7°$ and the maximum of 87% ponderomotive squeezing is obtained.

4.4.2 Optimum Squeezing

In the preceding section, we have described that in our hybrid model, ponderomotive squeezing can be generated by choosing appropriate measurement angle. This happens only around the frequencies of the mechanical side modes. However, the fluctuations in the noise spectral density at the frequency of the rotating mirror still remains well above the background noise floor. In order to reduce the fluctuations, we optimize the optical quadrature squeezing spectrum $S_{opt}(\omega)$ by choosing $\theta(\omega)$ in

such a way that $dS(\omega)/d\theta = 0$ for all the frequencies [39]. This gives

$$\theta_{opt}(\omega) = \frac{1}{2}\arctan\left[-\frac{B_2(\omega)}{B_1(\omega)}\right] , \tag{4.16}$$

where the expressions of $B_1(\omega)$ and $B_2(\omega)$ are too involved and are shown in the Appendix A.1. The optimized squeezing spectrum is presented in Figure 4.5. The

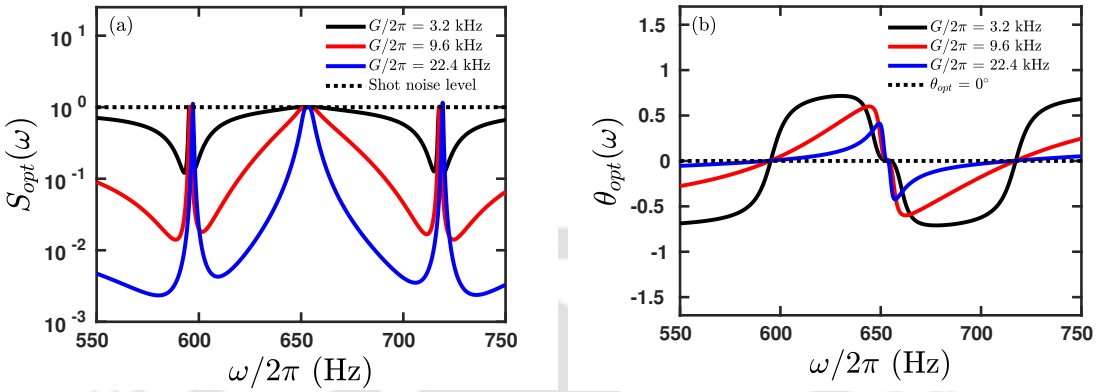

Figure 4.5: Optimized PSD of the optical quadrature as a function of the response frequency for $G/2\pi = 3.2$ kHz (black solid line), $G/2\pi = 9.6$ kHz (red solid line), and $G/2\pi = 22.4$ kHz (blue solid line). Parameters used are same as in Figure 4.2.

exciting findings of the optimized squeezing spectrum are: (i) there is a significant reduction in the fluctuations below the shot noise level at the vicinity of the side mode frequencies $\Omega_{c,d}$. (ii) Increasing the coupling strength between the atomic side modes with the cavity enhances the ponderomotive squeezing near the atomic side mode frequencies. Further, we observe a significant enhancement in the optical squeezing spectrum at the side mode frequencies $\Omega_{c,d}$. To understand its reason, we plot the optimized homodyne angle as a function of the frequency as depicted in Figure 4.5(b). The black-solid, red-solid, and blue-solid curves suggest the optimized homodyne angle becomes zero at the atomic side mode frequencies and at the mirror frequency. At these specific frequencies, the major contribution to the optimized optical squeezing spectrum originates from the first term of Eq. 4.15 ($|\xi_1(\omega)|^2$), only. The vanishingly small functional values of $\tilde{F}_2$ (Eq. A.7) at Ω_c, Ω_d, and ω_ϕ lead the optimal squeezing to the unity.

So far we have described the ponderomotive squeezing in our hybrid system by tuning various parameters. However, such squeezing occurs only at the frequencies of the Bragg-scattered mechanical side modes, whereas the optical quadrature fluctuations at the frequency of rotating mirror reduced just to the level of shot noise. In Figure 4.6, we explore the influence of the persistent flow in the ring BEC to manipulate the noise reduction and to achieve ponderomotive squeezing at the resonance frequency of the rotating mirror when one of the atomic side modes (c mode) degenerates with the mirror frequency. The blue solid curve of Figure 4.6, suggests the increase in the winding number of the BEC enhances its interaction with the OAM carrying input field ($l = 15$) to obtain 40% of ponderomotive squeezing. A weaker topological charge of the input field requires a relatively higher winding number of the rotating BEC to produce a similar amount of ponderomotive squeezing.

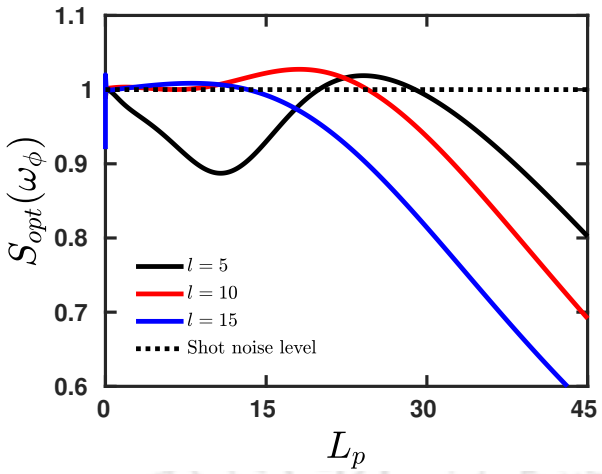

Figure 4.6: Optimized PSD of the output optical quadrature plotted at the frequency of the rotating mirror as a function of the winding number L_p. Parameters used are same as in Figure 4.2.

Additionally, for lower L_p values, the atomic collisions dominate to give rise to the optical mode squeezing.

4.5 Entanglement

In the preceding section, we have exploited the radiation pressure force to squeeze the quantum fluctuations of the output light field. The radiation pressure also plays a crucial role in cooling down the rotational mirror to its quantum ground state and producing entanglement. In particular, our hybrid system sets a stage where the interactions between the atomic side modes with the optical field and the radiation torque play a pivotal role in obtaining the bipartite entanglements between various degrees of freedom.

4.5.1 Bipartite Entanglement

To quantify the entanglement between various subsystems, we use the linearized dynamics of Eq. (4.12) and the Gaussian character of the quantum noise to achieve the stationary Gaussian state, which can be fully characterized by a 8×8 covariance matrix V, whose elements are written as $V_{ij} = \frac{1}{2}\langle u_i(\infty)u_j(\infty)+u_j(\infty)u_i(\infty)\rangle$. Under the stable condition, the covariance matrix V satisfies the Lyapunov equation [180]

$$\tilde{F}V + V\tilde{F}^T = -D, \tag{4.17}$$

where the matrix of the stationary noise correlation function is $D = \text{diag}\{0, \gamma_m(2n_c+1), 0, \gamma_m(2n_d+1), \gamma_0/2, \gamma_0/2, 0, \gamma_\phi(2n_m+1)\}$. The mean thermal excitation for the BEC side modes and the mechanical excitations of the rotating mirror are $n_i = (\exp\{\hbar\Omega_i/k_BT\}-1)^{-1}$ $(i = c, d)$, and $n_m = (\exp\{\hbar\omega_\phi/k_BT_\phi\}-1)^{-1}$, respectively. Using the above formalism, we study the two body entanglement in the hybrid

system by evaluating the logarithmic negativity E, defined as [208]

$$E = \max[0, -\ln 2\eta^{-}] \,, \tag{4.18}$$

where $\eta^{-} = 2^{-1/2}[\Sigma(V) - [\Sigma(V)^2 - 4\det(V_{sub})]^{1/2}]^{1/2}$, with $\Sigma(V) = \det A + \det B - 2\det C$. Here, V_{sub} is a generic 4×4 submatrix

$$V_{sub} = \begin{pmatrix} A & C \\ C^T & B \end{pmatrix} \,, \tag{4.19}$$

representing a particular bipartite system under consideration. A, B and C are 2×2 blocks of the covariance matrix. The bipartite entanglement exists if $E > 0$ *i.e.,* when $\eta^{-} < 1/2$.

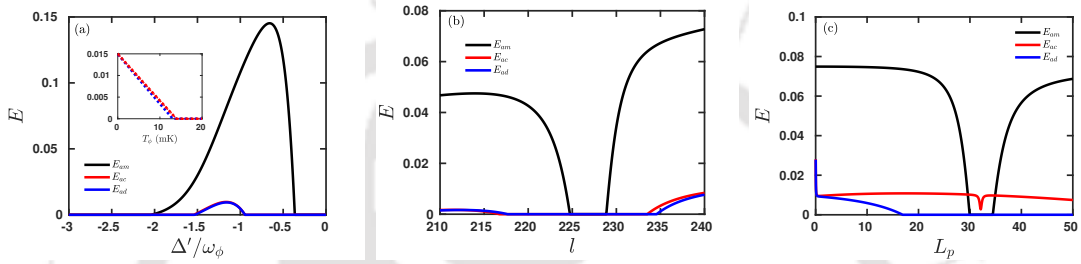

Figure 4.7: Various bipartite entanglements are plotted as a function of (a) cavity detuning when the orbital angular momentum of the input field $l = 243$ (b) the OAM of the driving field for $L_p = 1$ and (c) the winding number of BEC for $l = 243$ while the cavity detuning is $\Delta' = -1.2\omega_\phi$. We consider the resonance frequency of the rotating mirror to be $\omega_\phi = 3$ MHz, mass of the mirror $M = 0.1$ ng, radius $R_m = 20$ μm, the cavity length $L = 1$ mm, $\gamma_0/2\pi = 0.48$ MHz, $\gamma_m/2\pi = 0.8$ Hz, $\gamma_\phi/2\pi = 4.77$ Hz, $\omega_0/2\pi = 10^{15}$ Hz, $G/2\pi = 7.67$ kHz, $U_0/2\pi = 153.5$ Hz, $\Delta_a = 1.04$ GHz, $\omega_\rho/2\pi = 8.4$ kHz, and $a_{Na} = 2.5$ nm. The input power of the driving field is 0.19 nW. The bath temperature of the rotating mirror is $T_\phi = 5$ mK and the temperature of the atomic side modes are $T = 10$ nK. All the other parameters are same as in Figure 4.2.

In Figure 4.7(a), we study the influence of the cavity detuning on the bipartite entanglements in our hybrid system. E_{am}, E_{ac}, and E_{ad} denote the bipartite entanglements between cavity-mirror, cavity-atomic c mode, and cavity-atomic d mode, respectively. The black solid curve suggests the optimal cavity-mirror entanglement occurs around $\Delta' \approx -0.6\omega_\phi$. However, the blue and red solid curves represent the optimal values of E_{ac} and E_{ad} at $\Delta' \approx -1.2\omega_\phi$. The entanglement between the cavity and the atomic side modes sustains up to the bath temperature of the rotating mirror $T_\phi \approx 13$ mK, as presented by the inset of Figure 4.7(a). In Figure 4.7(b) and (c), we investigate the influence of the topological charge of the input optical drive and atomic rotation on the entanglement properties between various bipartite subsystems, respectively. The prominent interaction strength between the optical and the acoustic modes produces a more significant entanglement response than cavity-atomic side modes. More interestingly, our study predicts diminishing entanglements at a specific region of the OAM of the input beam. Also, the black solid curve of Figure 4.7(c) suggests for the topological charge of the input beam

$l = 243$ [209–213], the entanglement between the optical and the acoustic mode diminishes when the L_p values lie between 30 and 34. Moreover, the two Bragg scattered atomic side modes produce distinct entanglement responses arising from the optimal cavity detuning condition $\Delta' = -1.2\omega_\phi = -\Omega_{c,d}$. Now, to explain the diminishing entanglements, we determine the energy of the rotating mirror, which is given by

$$\begin{aligned} U &= \frac{\hbar\omega_\phi}{2}\left[\langle\delta\phi^2\rangle + \langle\delta L_z^2\rangle\right] = \frac{\hbar\omega_\phi}{2}\left(V_{77} + V_{88}\right) \\ &= \hbar\omega_\phi\left(n_{eff} + \frac{1}{2}\right), \end{aligned} \tag{4.20}$$

where the steady-state mean phonon number (n_{eff}) is associated with the effective mirror temperature (T_{eff}) by the relation $n_{eff} = (\exp(\hbar\omega_\phi/k_B T_{eff}) - 1)^{-1}$. In Figure 4.8 and in its inset, we present the effect of the OAM of the driving field and the angular momentum of atomic BEC on the steady-state phonon number, respectively. The solid black curve anticipates two distinct peaks in the effective phonon response stemming from the cooling inhibition associated with the topological charge $l \approx 226$ and 227, and the red solid curve of the inset depicts the suppression of cooling when the winding number L_p lies between 30 and 34. In the subsequent discussion, we demonstrate how the occurrence of the dark modes suppresses the cooling mechanism by introducing a center of mass coordinate (X_{1cm}, P_{1cm}) and a relative coordinate (X_{1r}, P_{1r}) as

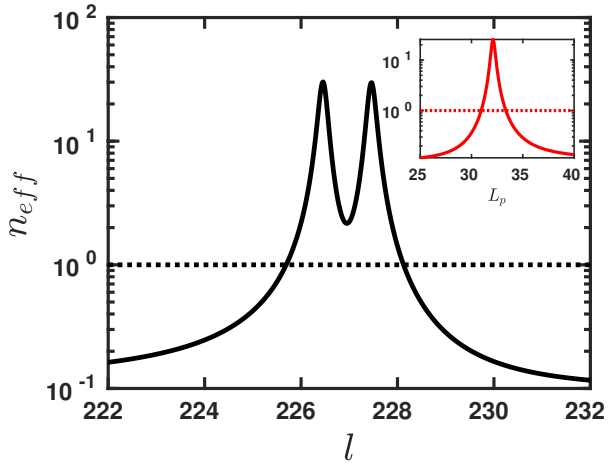

Figure 4.8: The mean phonon number of the rotating mirror as a function of the topological charge of the input field when $L_p = 1$. The inset presents the variation of effective phonon number as a function of the winding number of BEC for $l = 243$. The dotted lines correspond to the unity of the effective phonon number. All the other parameters are the same as in Figure 4.7.

$$\begin{aligned} X_{1cm} &= \frac{GX_d + g_\phi\phi}{\sqrt{G^2 + g_\phi^2}}, P_{1cm} = \frac{GY_d + g_\phi L_z}{\sqrt{G^2 + g_\phi^2}}, \\ X_{1r} &= \frac{G\phi - g_\phi X_d}{\sqrt{G^2 + g_\phi^2}}, P_{1r} = \frac{GL_z - g_\phi Y_d}{\sqrt{G^2 + g_\phi^2}}. \end{aligned} \tag{4.21}$$

Neglecting the atom-atom interaction, we can further express the Hamiltonian of Eq. 4.3 as

$$
\begin{aligned}
H = & -\hbar\left(\Delta_0 - \frac{U_0 N}{2}\right) a^\dagger a - i\hbar\eta(a - a^\dagger) + \frac{\hbar\omega_c}{2}\left(X_c^2 + Y_c^2\right) + \hbar G X_c a^\dagger a \\
& + \frac{\hbar}{2}\left(\frac{\omega_d G^2 + \omega_\phi g_\phi^2}{G^2 + g_\phi^2}\right)\left(X_{1cm}^2 + P_{1cm}^2\right) + \hbar\sqrt{G^2 + g_\phi^2} X_{1cm} a^\dagger a \\
& + \frac{\hbar}{2}\frac{G g_\phi}{G^2 + g_\phi^2}(\omega_\phi - \omega_d)(X_{1cm}X_{1r} + X_{1r}X_{1cm} + P_{1cm}P_{1r} + P_{1r}P_{1cm}) \\
& + \frac{\hbar}{2}\left(\frac{\omega_d g_\phi^2 + \omega_\phi G^2}{G^2 + g_\phi^2}\right)\left(X_{1r}^2 + P_{1r}^2\right), \qquad (4.22)
\end{aligned}
$$

where the sixth and the seventh terms correspond to the interaction of the center of mass coordinates with the optical field and the relative coordinate, respectively. The above analysis shows that when $L_p = 1$ and $l \approx 226$, one of the atomic side mode frequency ω_d matches with ω_ϕ and the relative coordinate is decoupled from the center of mass coordinate as well as the optical mode. Nonetheless, it is straightforward to show the existence of another set of center of mass and relative coordinates defined as

$$
\begin{aligned}
X_{2cm} &= \frac{G X_c + g_\phi \phi}{\sqrt{G^2 + g_\phi^2}}, P_{2cm} = \frac{G Y_c + g_\phi L_z}{\sqrt{G^2 + g_\phi^2}}, \\
X_{2r} &= \frac{G\phi - g_\phi X_c}{\sqrt{G^2 + g_\phi^2}}, P_{2r} = \frac{G L_z - g_\phi Y_c}{\sqrt{G^2 + g_\phi^2}}, \qquad (4.23)
\end{aligned}
$$

such that when $\omega_c = \omega_\phi$, the relative coordinate decouples from the center of mass and the cavity field. Hence, the radiation torque cooling is suppressed when the two atomic side modes degenerate with the acoustic mode ($\omega_\phi = \omega_{c,d}$) as the relative coordinate stays in the initial thermal state. Comparing Figure 4.7(b) and Figure 4.8, we can say that cooling a rotating mirror close to its quantum ground state ($l < 225$ and $l > 230$) helps to maintain quantum correlations. As a result, entanglement persists. However, between $l = 226$ and 227, the phonon number attains a minimum value of 2.2, which signifies the proximity of the quantum ground state. Even at these low phonon numbers, the quantum fluctuations are sufficiently strong to disrupt the coherence necessary to attain any entanglement.

4.5.2 Tripartite Entanglement

Lastly, we study the tripartite entanglements between the cavity, mirror, and atomic side modes by quantifying the minimum residual contangle as [214, 215]

$$
\mathcal{R}_\tau^{\min} = \min\left[\mathcal{R}_\tau^{a|mk}, \mathcal{R}_\tau^{m|ak}, \mathcal{R}_\tau^{k|am}\right], \qquad (4.24)
$$

where, $\mathcal{R}_\tau^{i|jk} = C_{i|jk} - C_{i|j} - C_{i|k} \geq 0$ $(i, j, k = \text{cavity}(a), \text{mirror}(m),$ atomic c or d modes), is the residual contangle written in terms of contangle $C_{u|v}$ of subsystems of u and v (see Ref. [138] for more details of calculating $\mathcal{R}_\tau^{\min}$). The black solid and the red solid curve of Figure 4.9(a) suggest that the tripartite entanglements between the three

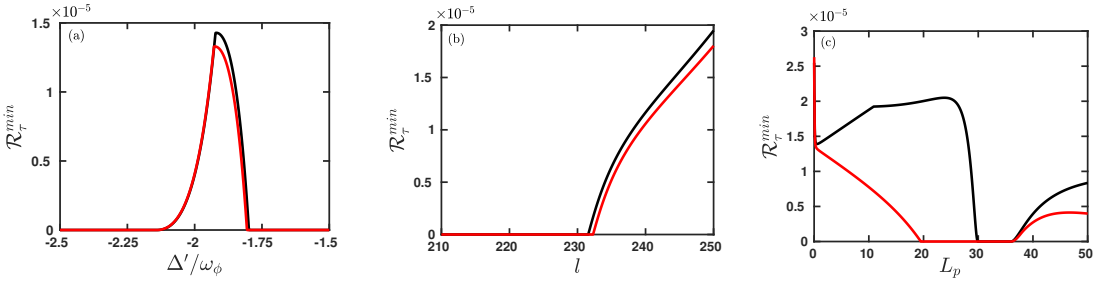

Figure 4.9: Tripartite entanglement in terms of minimum residual contangle versus (a) cavity detuning for $l = 243$, (b) the OAM of the driving field for $L_p = 1$ and $\Delta' = -1.9\omega_\phi$. The black solid curve accounts for the tripartite entanglement associated with the cavity-mirror-atomic c mode. The red solid curve accounts for the tripartite entanglement associated with the cavity-mirror-atomic d mode. All the other parameters are same as in Figure 4.7.

constituents of the model system (cavity, mirror, and c-or d-modes) are optimized when the cavity detuning $\Delta' = -1.9\omega_\phi$. Moreover, the tripartite entanglement arises when there's frequent optical interaction with matter waves, particularly in proportion to the number of lattice maxima ($2l$). It means that the likelihood of optical interaction increases as the number of lattice maxima increases. When such interactions become frequent, they can lead to the emergence of tripartite entanglement, as shown in Figure 4.9(b). In Figure 4.9(c), we present the tripartite entanglement between the cavity, mirror, and atomic side modes as a function of the winding number of the condensate atoms when the topological charge of the driving field is $l = 243$. The black solid curve presents the diminishing effect of the three body entanglement around $L_p = 30$ due to the thermal fluctuations of the rotating mirror. The red solid curve depicts the tripartite entanglement response between the cavity, mirror, and the atomic d-mode. The presence of the atomic d-mode produces a wider range in L_p, where the tripartite entanglement does not persist. Moreover, the very distinct three-body entanglement response can be utilized to distinguish clearly between the two atomic side modes.

4.6 Conclusion

This chapter presents an unique hybrid opto-rotational system consisting of a ring BEC confined inside a LG cavity. The system shows a distinctive way to squeeze the quantum fluctuations of the output light field quadratures below the shot noise. With the experimentally feasible parameters and for a measurement angle of 7°, we achieved 87% of the ponderomotive squeezing around the frequencies of Bragg-scattered sidemodes. Furthermore, two very distinct systems in the hybrid configuration gets coupled to a common cavity mode. As a consequence, the optical squeezing of about 40% occurs even at the mirror frequency and can further be manipulated by the persistent currents in the annularly trapped BEC. This hybrid system also provides a versatile pathway to utilize the atomic interactions and the radiation pressure force to produce bipartite and tripartite entanglement between different physical entities of the system. Interestingly, the quantum correlations in

the system last under the cooling conditions of the rotating end mirror and correspondingly there exists a parameter regime where the entanglement survives. These results may find interesting applications in atomtronics, sensing and quantum information processing.

Chapter 5

Conclusions and future plan

In this thesis, we delved into the multifaceted realm of radiation pressure in nanophotonics. Our research extended to diverse hybrid systems, including a ring cavity resonator with two movable mirrors, a cavity magnomechanical system consisting of two interacting microwave cavities, and an annularly trapped Bose-Einstein condensate (BEC) in an optorotational system driven by Laguerre-Gaussian mode. We address two types of problems related to hybrid systems. The first type focuses on achieving controllable output probe pulse generation from dispersive optomechanical and cavity magnomechanical systems, as discussed in Chapters 2 and 3. In the second type, we explore various quantum effects, such as ponderomotive squeezing and entanglement generation, among various subsystems of a hybrid optorotational system containing annularly trapped BEC.

In Chapter 2, we propose a unique scheme to control the group velocity of the transmitted probe pulse depending upon the phase properties of the control field from a red-detuned ring cavity resonator that consists of two nearly degenerate movable mirrors. To probe the effect of the robust control field, we apply a weak probe field to the system and identify a double transparency window when the two-photon resonance condition holds. Further, a weak mechanical drive to one of the movable mirrors produces a controllable output probe field and the Four-Wave mixing (FWM) field around the upper transmission window. The controllability of the output probe (FWM) field arises from interference between the cavity-generated Stokes (anti-Stokes) field and the mechanical drive-induced upper mechanical (lower mechanical) sideband when the mechanical drive is in phase with the input probe field. Moreover, the control field phase-sensitive interference effect produces an extra tunability to control the output probe transmission and the generated Four-Wave mixing field through the upper transmission window. Our investigation reveals that the presence of the external mechanical pump amplitude along with suitable control field phases can switch the group delay of the probe pulse from slow to fast light and verify it by studying the propagation of a Gaussian probe pulse well contained in the transparency window.

In Chapter 3, we investigated the controllable probe field generation in a magnomechanical resonator system. The system comprises two coupled microwave resonators. One consists of a ferrimagnetic yttrium iron garnet (YIG) sphere. Applying a uniform bias magnetic field excites the magnon mode inside the YIG sphere. That,

in turn, couples with the cavity mode. The shape deformation due to the external bias magnetic field produces magnon-phonon coupling. In the weak magnon-photon coupling condition, the output probe field intensity diminishes as the system becomes highly absorptive when both cavities are passive. However, we overcome the situation by replacing the passive auxiliary cavity with an active one. The introduction of the active auxiliary cavity produces an effective gain associated with an anomalous dispersion when the magnomechanical resonance condition holds. As a result, the output probe field amplifies, and the negative time delay suggests the superluminal probe field propagation. Further, tuning the exchange interaction strength between the cavities alters the effective gain and the slope of the dispersion curve of the system. Interestingly, our study finds the existence of an upper bound for the intensity amplification and the advancement of the probe pulse that comes from the stability condition of the system.

In Chapter 4, we investigate various quantum effects, such as ponderomotive squeezing and entanglement generation in a hybrid optorotational system consisting of an annularly trapped Bose-Einstein condensate (BEC) inside it. The spiral phase plates act as the end mirrors of the cavity. The input coupler is a fixed mirror, whereas the rear mirror rotates torsionally with a clamped support. We externally drive the cavity by Lauguerre-Gaussian (LG) modes. The annularly trapped rotating condensates interact with the intracavity field and produce two atomic side modes interacting with the cavity field. We observe that the noise spectral density contains three peaks; two peak positions correspond to two different atomic side mode frequencies, and another arises at the mirror frequency due to the optorotational coupling. With the experimentally feasible parameters and the measurement angle 7°, the optical field is squeezed by 87% around the side mode frequencies over the bandwidth of 20 Hz. Further, the atomic circulations and the topological charge of the drive field play instrumental roles in squeezing the output optical field around 40%. Our study identifies a suitable range of parameters for creating entanglement between different components of the hybrid model system that can be achieved with current experimental capabilities. We found that when one of the side modes aligns with the rotational mirror, the entanglement between the cavity and the mirror mode disappears due to cooling inhibition. Additionally, the unique, distinctive behavior of the tripartite entanglement between the cavity, atomic side modes, and the mirror can be used to differentiate between the two atomic side modes.

Future Plan

In the future, we could expand to an optomechanical array to enable the study of quantum many-body dynamics. It would be interesting to investigate the feasibility of transferring quantum information over long distances without distortion and to use the optomechanical array as a storage device for later retrieval. We can also play with various optomechanical coupling strengths to study the non-reciprocal photon transmission through the optomechanical array. Further, we could explore the potential of ponderomotive squeezing within this optomechanical array platform. To our knowledge, this research area is still quite open.

Appendix A

Appendix of chapter 4

A.1 Power Spectral Density

To obtain the output quadrature noise spectrum, we use following input-output relation,

$$a_{out}(\omega) = \sqrt{\gamma_o}\delta a(\omega) - \delta a_{in}(\omega) \ . \tag{A.1}$$

From Eq. (A.1), we can write following quadrature relations

$$Q_{out}(\omega) = \sqrt{\gamma_o}\delta Q(\omega) - Q_{in}(\omega) \ , \tag{A.2}$$
$$P_{out}(\omega) = \sqrt{\gamma_o}\delta P(\omega) - P_{in}(\omega) \ , \tag{A.3}$$

By Fourier transforming the Eq. (4.12), we obtain the output optical quadratures as

$$\begin{aligned} Q_{out}(\omega) &= \Big[\sqrt{\gamma_o}\tilde{F}_2(\omega) - 1\Big]Q_{in}(\omega) + i\sqrt{\gamma_o}\tilde{F}_3(\omega)P_{in}(\omega) + \sqrt{2\gamma_o}\tilde{F}_5(\omega)\epsilon_c(\omega) \\ &\quad + \sqrt{2\gamma_o}\tilde{F}_7(\omega)\epsilon_d(\omega) + \sqrt{2\gamma_o}\tilde{F}_9(\omega)\epsilon_\phi(\omega) \ , \\ P_{out}(\omega) &= -i\sqrt{\gamma_o}\Big[2\tilde{F}_1(\omega) + \tilde{F}_3(\omega)\Big]Q_{in}(\omega) + \Big[\sqrt{\gamma_o}\tilde{F}_2(\omega) - 1\Big]P_{in}(\omega) \\ &\quad - i\sqrt{2\gamma_o}\tilde{F}_4(\omega)\epsilon_c(\omega) - i\sqrt{2\gamma_o}\tilde{F}_6(\omega)\epsilon_d(\omega) - i\sqrt{2\gamma_o}\tilde{F}_8(\omega)\epsilon_\phi(\omega) \ , \end{aligned} \tag{A.4}$$

where $\tilde{F}_i(\omega)$'s are complicated complex functions written as below,

$$\begin{aligned} \tilde{F}_1(\omega) &= \frac{ia_s^2\sqrt{\gamma_0}}{D(\omega)}[G^2A_\phi(\omega)[\tilde{\omega}_c(\mathcal{A} + \tilde{A}_d(\omega)) + \tilde{\omega}_d(\tilde{A}_c(\omega) - \mathcal{A})] \\ &\quad + \omega_\phi g_\phi^2[\mathcal{A}^2 + \tilde{A}_c(\omega)\tilde{A}_d(\omega)]], \\ \tilde{F}_2(\omega) &= \frac{\sqrt{\gamma_0}}{D(\omega)}[\mathcal{A}^2 + \tilde{A}_c(\omega)\tilde{A}_d(\omega)]A_3(\omega)A_\phi(\omega), \\ \tilde{F}_3(\omega) &= \frac{i\Delta'\sqrt{\gamma_0}}{D(\omega)}A_\phi(\omega)[\mathcal{A}^2 + \tilde{A}_c(\omega)\tilde{A}_d(\omega)], \\ \tilde{F}_4(\omega) &= -\frac{iGa_s\Omega_c}{D(\omega)}A_3(\omega)A_\phi(\omega)[\mathcal{A} + \tilde{A}_d(\omega)], \\ \tilde{F}_5(\omega) &= \frac{\Delta'\Omega_cGa_s}{D(\omega)}A_\phi(\omega)[\mathcal{A} + \tilde{A}_d(\omega)], \end{aligned}$$

$$\tilde{F}_6(\omega) = -\frac{iGa_s\Omega_d}{D(\omega)}A_3(\omega)A_\phi(\omega)[\tilde{A}_c(\omega) - \mathcal{A}],$$
$$\tilde{F}_7(\omega) = \frac{\Delta'\Omega_d Ga_s}{D(\omega)}A_\phi(\omega)[-\mathcal{A} + \tilde{A}_c(\omega)],$$
$$\tilde{F}_8(\omega) = -\frac{ig_\phi a_s\omega_\phi}{D(\omega)}A_3(\omega)[\mathcal{A}^2 + \tilde{A}_c(\omega)\tilde{A}_d(\omega)],$$
$$\tilde{F}_9(\omega) = \frac{\Delta'\omega_\phi g_\phi a_s}{D(\omega)}[\mathcal{A}^2 + \tilde{A}_c(\omega)\tilde{A}_d(\omega)]. \tag{A.5}$$

Further, using Eq. (A.4) in Eq. (4.14), we obtain

$$Q_\theta^{out}(\omega) = \xi_1(\omega)Q_{in}(\omega) + \xi_2(\omega)P_{in}(\omega) + \xi_3(\omega)\epsilon_c(\omega) + \xi_4(\omega)\epsilon_d(\omega) + \xi_5(\omega)\epsilon_\phi(\omega)\ , \tag{A.6}$$

where, ξ_i's can be expressed as

$$\xi_1(\omega) = -i\sqrt{\gamma_o}\left[2\tilde{F}_1(\omega) + \tilde{F}_3(\omega)\right]\sin\theta + \left[\sqrt{\gamma_o}\tilde{F}_2(\omega) - 1\right]\cos\theta\ ,$$
$$\xi_2(\omega) = \left[\sqrt{\gamma_o}\tilde{F}_2(\omega) - 1\right]\sin\theta + i\sqrt{\gamma_o}\tilde{F}_3(\omega)\cos\theta\ ,$$
$$\xi_3(\omega) = -i\sqrt{2\gamma_o}\tilde{F}_4(\omega)\sin\theta + \sqrt{2\gamma_o}\tilde{F}_5(\omega)\cos\theta\ ,$$
$$\xi_4(\omega) = -i\sqrt{2\gamma_o}\tilde{F}_6(\omega)\sin\theta + \sqrt{2\gamma_o}\tilde{F}_7(\omega)\cos\theta\ ,$$
$$\xi_5(\omega) = -i\sqrt{2\gamma_o}\tilde{F}_8(\omega)\sin\theta + \sqrt{2\gamma_o}\tilde{F}_9(\omega)\cos\theta\ . \tag{A.7}$$

The output quadrature spectrum is obtained from the definition

$$S(\omega) = \frac{1}{\pi}\int_{-\infty}^{\infty} d\omega' \langle Q_\theta^{out}(\omega')Q_\theta^{out}(\omega)\rangle\ . \tag{A.8}$$

By using the following correlation relations

$$\langle Q_{in}(\omega')Q_{in}(\omega)\rangle = \langle P_{in}(\omega')P_{in}(\omega)\rangle = \pi\delta(\omega' + \omega)\ ,$$
$$\langle Q_{in}(\omega')P_{in}(\omega)\rangle = -\langle P_{in}(\omega')Q_{in}(\omega)\rangle = i\pi\delta(\omega' + \omega)\ ,$$
$$\langle \epsilon_{c,d}(\omega')\epsilon_{c,d}(\omega)\rangle = 2\pi\frac{\gamma_m\omega'}{\Omega_{c,d}}\left[1 + \coth\left(\frac{\hbar\omega'}{2k_BT}\right)\right]\delta(\omega' + \omega)\ ,$$
$$\langle \epsilon_\phi(\omega')\epsilon_\phi(\omega)\rangle = 2\pi\frac{\gamma_\phi\omega'}{\omega_\phi}\left[1 + \coth\left(\frac{\hbar\omega'}{2k_BT_\phi}\right)\right]\delta(\omega' + \omega)\ , \tag{A.9}$$

we obtain the analytical expression of Eq. 4.15.

A.2 Optimized Squeezing

The optimized angle in Eq. (4.16) is expressed in terms of $B_1(\omega)$ and $B_2(\omega)$ and their expressions are given below

$$B_1(\omega) = |\kappa_1(\omega)|^2 - |\kappa_3(\omega)|^2 + i(\kappa_1^*(\omega)\kappa_2(\omega) - \kappa_1(\omega)\kappa_2^*(\omega) - \kappa_2^*(\omega)\kappa_3(\omega)$$

$$+\kappa_3^*(\omega)\kappa_2(\omega)) - 2\gamma_m\frac{\omega}{\Omega_c}\left[1-\coth\left(\frac{\hbar\omega}{2K_BT}\right)\right]\left(|\kappa_4(\omega)|^2-|\kappa_5(\omega)|^2\right)$$
$$-2\gamma_m\frac{\omega}{\Omega_d}\left[1-\coth\left(\frac{\hbar\omega}{2K_BT}\right)\right]\left(|\kappa_6(\omega)|^2-|\kappa_7(\omega)|^2\right)$$
$$-2\gamma_\phi\frac{\omega}{\omega_\phi}\left[1-\coth\left(\frac{\hbar\omega}{2K_BT_\phi}\right)\right]\left(|\kappa_8(\omega)|^2-|\kappa_9(\omega)|^2\right), \tag{A.10}$$

$$B_2(\omega) = -2\gamma_m\frac{\omega}{\Omega_c}\left[1-\coth\left(\frac{\hbar\omega}{2K_BT}\right)\right](\kappa_4^*(\omega)\kappa_5(\omega)+\kappa_4(\omega)\kappa_5^*(\omega))$$
$$-2\gamma_m\frac{\omega}{\Omega_d}\left[1-\coth\left(\frac{\hbar\omega}{2K_BT}\right)\right](\kappa_6^*(\omega)\kappa_7(\omega)+\kappa_6(\omega)\kappa_7^*(\omega))$$
$$-2\gamma_\phi\frac{\omega}{\omega_\phi}\left[1-\coth\left(\frac{\hbar\omega}{2K_BT_\phi}\right)\right](\kappa_9(\omega)\kappa_8^*(\omega)+\kappa_9^*(\omega)\kappa_8(\omega))$$
$$+\kappa_1^*(\omega)\kappa_2(\omega)+\kappa_2^*(\omega)\kappa_1(\omega)+\kappa_2^*(\omega)\kappa_3(\omega)+\kappa_2(\omega)\kappa_3^*(\omega)$$
$$+i\left(\kappa_1^*(\omega)\kappa_3(\omega)-\kappa_3^*(\omega)\kappa_1(\omega)\right) \tag{A.11}$$

where κ_i's are written as

$$\kappa_1(\omega) = -i\sqrt{\gamma_o}\left[2\tilde{F}_1(\omega)+\tilde{F}_3(\omega)\right], \kappa_2(\omega) = \sqrt{\gamma_o}\tilde{F}_2(\omega)-1, \kappa_3(\omega) = i\sqrt{\gamma_o}\tilde{F}_3(\omega),$$
$$\kappa_4(\omega) = -i\sqrt{2\gamma_o}\tilde{F}_4(\omega), \kappa_5(\omega) = \sqrt{2\gamma_o}\tilde{F}_5(\omega), \kappa_6(\omega) = -i\sqrt{2\gamma_o}\tilde{F}_6(\omega),$$
$$\kappa_7(\omega) = \sqrt{2\gamma_o}\tilde{F}_7(\omega), \kappa_8(\omega) = -i\sqrt{2\gamma_o}\tilde{F}_8(\omega), \kappa_9(\omega) = \sqrt{2\gamma_o}\tilde{F}_9(\omega). \tag{A.12}$$

Bibliography

[1] James Clerk Maxwell. *A treatise on electricity and magnetism*, volume 1. Clarendon press, 1873.

[2] Peter Lebedew. Untersuchungen über die druckkräfte des lichtes. *Annalen der Physik*, 311(11):433–458, 1901.

[3] VB Braginsky, AB Manukin, and William O Hamilton. Measurement of weak forces in physics experiments, 1978.

[4] V.B. Braginsky, S.E. Strigin, and S.P. Vyatchanin. Parametric oscillatory instability in fabry–perot interferometer. *Physics Letters A*, 287(5):331–338, 2001.

[5] V. B. Braginskiĭ, A. B. Manukin, and M. Yu. Tikhonov. Investigation of Dissipative Ponderomotive Effects of Electromagnetic Radiation. *Soviet Journal of Experimental and Theoretical Physics*, 31:829, January 1970.

[6] A. Schliesser, O. Arcizet, R. Rivière, G. Anetsberger, and T. J. Kippenberg. Resolved-sideband cooling and position measurement of a micromechanical oscillator close to the heisenberg uncertainty limit. *Nature Physics*, 5(7):509–514, Jul 2009.

[7] A Schliesser, G Anetsberger, R Rivière, O Arcizet, and T J Kippenberg. High-sensitivity monitoring of micromechanical vibration using optical whispering gallery mode resonators. *New Journal of Physics*, 10(9):095015, sep 2008.

[8] Matt Eichenfield, Jasper Chan, Ryan M. Camacho, Kerry J. Vahala, and Oskar Painter. Optomechanical crystals. *Nature*, 462(7269):78–82, Nov 2009.

[9] Tal Carmon, Hossein Rokhsari, Lan Yang, Tobias J. Kippenberg, and Kerry J. Vahala. Temporal behavior of radiation-pressure-induced vibrations of an optical microcavity phonon mode. *Phys. Rev. Lett.*, 94:223902, Jun 2005.

[10] T. J. Kippenberg, H. Rokhsari, T. Carmon, A. Scherer, and K. J. Vahala. Analysis of radiation-pressure induced mechanical oscillation of an optical microcavity. *Phys. Rev. Lett.*, 95:033901, Jul 2005.

[11] H. Rokhsari, T. J. Kippenberg, T. Carmon, and K. J. Vahala. Radiation-pressure-driven micro-mechanical oscillator. *Opt. Express*, 13(14):5293–5301, Jul 2005.

[12] Ivan Favero, Sebastian Stapfner, David Hunger, Philipp Paulitschke, Jakob Reichel, Heribert Lorenz, Eva M. Weig, and Khaled Karrai. Fluctuating nanomechanical system in a high finesse optical microcavity. *Opt. Express*, 17(15):12813–12820, Jul 2009.

[13] Xiaoshun Jiang, Qiang Lin, Jessie Rosenberg, Kerry Vahala, and Oskar Painter. High-q double-disk microcavities for cavity optomechanics. *Opt. Express*, 17(23):20911–20919, Nov 2009.

[14] Gustavo S. Wiederhecker, Long Chen, Alexander Gondarenko, and Michal Lipson. Controlling photonic structures using optical forces. *Nature*, 462(7273):633–636, Dec 2009.

[15] Dustin Kleckner and Dirk Bouwmeester. Sub-kelvin optical cooling of a micromechanical resonator. *Nature*, 444(7115):75–78, Nov 2006.

[16] S. Gigan, H. R. Böhm, M. Paternostro, F. Blaser, G. Langer, J. B. Hertzberg, K. C. Schwab, D. Bäuerle, M. Aspelmeyer, and A. Zeilinger. Self-cooling of a micromirror by radiation pressure. *Nature*, 444(7115):67–70, Nov 2006.

[17] O. Arcizet, P.-F. Cohadon, T. Briant, M. Pinard, and A. Heidmann. Radiation-pressure cooling and optomechanical instability of a micromirror. *Nature*, 444(7115):71–74, Nov 2006.

[18] J. D. Thompson, B. M. Zwickl, A. M. Jayich, Florian Marquardt, S. M. Girvin, and J. G. E. Harris. Strong dispersive coupling of a high-finesse cavity to a micromechanical membrane. *Nature*, 452(7183):72–75, Mar 2008.

[19] A M Jayich, J C Sankey, B M Zwickl, C Yang, J D Thompson, S M Girvin, A A Clerk, F Marquardt, and J G E Harris. Dispersive optomechanics: a membrane inside a cavity. *New Journal of Physics*, 10(9):095008, sep 2008.

[20] J. C. Sankey, C. Yang, B. M. Zwickl, A. M. Jayich, and J. G. E. Harris. Strong and tunable nonlinear optomechanical coupling in a low-loss system. *Nature Physics*, 6(9):707–712, Sep 2010.

[21] D. J. Wilson, C. A. Regal, S. B. Papp, and H. J. Kimble. Cavity optomechanics with stoichiometric sin films. *Phys. Rev. Lett.*, 103:207204, Nov 2009.

[22] C. A. Regal, J. D. Teufel, and K. W. Lehnert. Measuring nanomechanical motion with a microwave cavity interferometer. *Nature Physics*, 4(7):555–560, Jul 2008.

[23] T. Rocheleau, T. Ndukum, C. Macklin, J. B. Hertzberg, A. A. Clerk, and K. C. Schwab. Preparation and detection of a mechanical resonator near the ground state of motion. *Nature*, 463(7277):72–75, Jan 2010.

[24] G. S. Agarwal and Sumei Huang. Electromagnetically induced transparency in mechanical effects of light. *Phys. Rev. A*, 81:041803, Apr 2010.

[25] Kenan Qu and G. S. Agarwal. Phonon-mediated electromagnetically induced absorption in hybrid opto-electromechanical systems. *Phys. Rev. A*, 87:031802, Mar 2013.

[26] Xiao-Yun Wang, Liu-Gang Si, Zeng-Xing Liu, Xiao-Hu Lu, and Ying Wu. Tunable optical amplification arising from blue detuning in a quadratically coupled optomechanical system. *J. Opt. Soc. Am. B*, 36(5):1355–1362, May 2019.

[27] Hui Jing, S. K. Özdemir, Xin-You Lü, Jing Zhang, Lan Yang, and Franco Nori. $\mathcal{PT}$-symmetric phonon laser. *Phys. Rev. Lett.*, 113:053604, Jul 2014.

[28] Massimiliano Rossi, David Mason, Junxin Chen, Yeghishe Tsaturyan, and Albert Schliesser. Measurement-based quantum control of mechanical motion. *Nature*, 563(7729):53–58, Nov 2018.

[29] C. Genes, D. Vitali, P. Tombesi, S. Gigan, and M. Aspelmeyer. Ground-state cooling of a micromechanical oscillator: Comparing cold damping and cavity-assisted cooling schemes. *Phys. Rev. A*, 77:033804, Mar 2008.

[30] Claudiu Genes, David Vitali, and Paolo Tombesi. Simultaneous cooling and entanglement of mechanical modes of a micromirror in an optical cavity. *New Journal of Physics*, 10(9):095009, sep 2008.

[31] Jeff T. Hill, Amir H. Safavi-Naeini, Jasper Chan, and Oskar Painter. Coherent optical wavelength conversion via cavity optomechanics. *Nature Communications*, 3(1):1196, Nov 2012.

[32] Chunhua Dong, Victor Fiore, Mark C Kuzyk, Lin Tian, and Hailin Wang. Optical wavelength conversion via optomechanical coupling in a silica resonator. *Annalen der Physik*, 527(1-2):100–106, 2015.

[33] Victor Fiore, Yong Yang, Mark C. Kuzyk, Russell Barbour, Lin Tian, and Hailin Wang. Storing optical information as a mechanical excitation in a silica optomechanical resonator. *Phys. Rev. Lett.*, 107:133601, Sep 2011.

[34] D. Vitali, S. Gigan, A. Ferreira, H. R. Böhm, P. Tombesi, A. Guerreiro, V. Vedral, A. Zeilinger, and M. Aspelmeyer. Optomechanical entanglement between a movable mirror and a cavity field. *Phys. Rev. Lett.*, 98:030405, Jan 2007.

[35] Claudiu Genes, Andrea Mari, David Vitali, and Paolo Tombesi. Quantum effects in optomechanical systems. *Advances in atomic, molecular, and optical physics*, 57:33–86, 2009.

[36] David Vitali, Stefano Mancini, and Paolo Tombesi. Stationary entanglement between two movable mirrors in a classically driven fabry–perot cavity. *Journal of Physics A: Mathematical and Theoretical*, 40(28):8055, jun 2007.

[37] Stefano Mancini, Vittorio Giovannetti, David Vitali, and Paolo Tombesi. Entangling macroscopic oscillators exploiting radiation pressure. *Phys. Rev. Lett.*, 88:120401, Mar 2002.

[38] C. Fabre, M. Pinard, S. Bourzeix, A. Heidmann, E. Giacobino, and S. Reynaud. Quantum-noise reduction using a cavity with a movable mirror. *Phys. Rev. A*, 49:1337–1343, Feb 1994.

[39] S. Mancini and P. Tombesi. Quantum noise reduction by radiation pressure. *Phys. Rev. A*, 49:4055–4065, May 1994.

[40] Ö. O. Soykal and M. E. Flatté. Strong field interactions between a nanomagnet and a photonic cavity. *Phys. Rev. Lett.*, 104:077202, Feb 2010.

[41] Ö. O. Soykal and M. E. Flatté. Size dependence of strong coupling between nanomagnets and photonic cavities. *Phys. Rev. B*, 82:104413, Sep 2010.

[42] Hans Huebl, Christoph W. Zollitsch, Johannes Lotze, Fredrik Hocke, Moritz Greifenstein, Achim Marx, Rudolf Gross, and Sebastian T. B. Goennenwein. High cooperativity in coupled microwave resonator ferrimagnetic insulator hybrids. *Phys. Rev. Lett.*, 111:127003, Sep 2013.

[43] Rui Hou, Wei Zhang, Xue Han, Hong-Fu Wang, and Shou Zhang. Magnon blockade based on the kerr nonlinearity in cavity electromagnonics. *Phys. Rev. A*, 109:033721, Mar 2024.

[44] Ji-kun Xie, Sheng-li Ma, and Fu-li Li. Quantum-interference-enhanced magnon blockade in an yttrium-iron-garnet sphere coupled to superconducting circuits. *Phys. Rev. A*, 101:042331, Apr 2020.

[45] Jie Zhao, Longhao Wu, Tiefu Li, Yu-xi Liu, Franco Nori, Yulong Liu, and Jiangfeng Du. Phase-controlled pathway interferences and switchable fast-slow light in a cavity-magnon polariton system. *Phys. Rev. Appl.*, 15:024056, Feb 2021.

[46] Hong-Ping Xu, Yan Wang, Ji-Ming Gao, Ai-Xia Zhang, Ju-Kui Xue, and Zi-Fa Yu. Kerr nonlinearity assisted magnetically induced transparency in cavity magnon polaritons. *Opt. Lett.*, 49(2):367–370, Jan 2024.

[47] M. S. Ebrahimi, Ali Motazedifard, and M. Bagheri Harouni. Single-quadrature quantum magnetometry in cavity electromagnonics. *Phys. Rev. A*, 103:062605, Jun 2021.

[48] A. L. Schawlow and C. H. Townes. Infrared and optical masers. *Phys. Rev.*, 112:1940–1949, Dec 1958.

[49] H.G. Dehmelt. Radiofrequency spectroscopy of stored ions i: Storage**part ii: Spectroscopy is now scheduled to appear in volume v of this series. volume 3 of *Advances in Atomic and Molecular Physics*, pages 53–72. Academic Press, 1968.

[50] Wolfgang Paul. Electromagnetic traps for charged and neutral particles. *Rev. Mod. Phys.*, 62:531–540, Jul 1990.

[51] John Prodan, Alan Migdall, William D. Phillips, Ivan So, Harold Metcalf, and Jean Dalibard. Stopping atoms with laser light. *Phys. Rev. Lett.*, 54:992–995, Mar 1985.

[52] Franco Dalfovo, Stefano Giorgini, Lev P. Pitaevskii, and Sandro Stringari. Theory of bose-einstein condensation in trapped gases. *Rev. Mod. Phys.*, 71:463–512, Apr 1999.

[53] K. B. Davis, M. O. Mewes, M. R. Andrews, N. J. van Druten, D. S. Durfee, D. M. Kurn, and W. Ketterle. Bose-einstein condensation in a gas of sodium atoms. *Phys. Rev. Lett.*, 75:3969–3973, Nov 1995.

[54] Gabriele De Chiara, Mauro Paternostro, and G. Massimo Palma. Entanglement detection in hybrid optomechanical systems. *Phys. Rev. A*, 83:052324, May 2011.

[55] C. Genes, D. Vitali, and P. Tombesi. Emergence of atom-light-mirror entanglement inside an optical cavity. *Phys. Rev. A*, 77:050307, May 2008.

[56] Theo Torres, Sam Patrick, Antonin Coutant, Maurício Richartz, Edmund W. Tedford, and Silke Weinfurtner. Rotational superradiant scattering in a vortex flow. *Nature Physics*, 13(9):833–836, Sep 2017.

[57] Sam Patrick. Rotational superradiance with bogoliubov dispersion. *Classical and Quantum Gravity*, 38(9):095010, apr 2021.

[58] Henning Moritz, Thilo Stöferle, Michael Köhl, and Tilman Esslinger. Exciting collective oscillations in a trapped 1d gas. *Phys. Rev. Lett.*, 91:250402, Dec 2003.

[59] Peter W. Milonni and Joseph H. Eberly. *Laser Physics*. John Wiley & Sons, Inc., 1986.

[60] Christopher C Gerry and Peter L Knight. *Introductory quantum optics*. Cambridge university press, 2023.

[61] E.T. Jaynes and F.W. Cummings. Comparison of quantum and semiclassical radiation theories with application to the beam maser. *Proceedings of the IEEE*, 51(1):89–109, 1963.

[62] Gerald Hechenblaikner, Markus Gangl, Peter Horak, and Helmut Ritsch. Cooling an atom in a weakly driven high-q cavity. *Phys. Rev. A*, 58:3030–3042, Oct 1998.

[63] Rui Xu, Deng-Gao Lai, Bang-Pin Hou, Adam Miranowicz, and Franco Nori. Millionfold improvement in multivibration-feedback optomechanical refrigeration via auxiliary mechanical coupling. *Phys. Rev. A*, 106:033509, Sep 2022.

[64] I. Wilson-Rae, N. Nooshi, W. Zwerger, and T. J. Kippenberg. Theory of ground state cooling of a mechanical oscillator using dynamical backaction. *Phys. Rev. Lett.*, 99:093901, Aug 2007.

[65] Jasper Chan, T. P. Mayer Alegre, Amir H. Safavi-Naeini, Jeff T. Hill, Alex Krause, Simon Gröblacher, Markus Aspelmeyer, and Oskar Painter. Laser cooling of a nanomechanical oscillator into its quantum ground state. *Nature*, 478(7367):89–92, Oct 2011.

[66] Michael Schmidt, Max Ludwig, and Florian Marquardt. Optomechanical circuits for nanomechanical continuous variable quantum state processing. *New Journal of Physics*, 14(12):125005, dec 2012.

[67] P. Zoller, Th. Beth, D. Binosi, R. Blatt, H. Briegel, D. Bruss, T. Calarco, J. I. Cirac, D. Deutsch, J. Eisert, A. Ekert, C. Fabre, N. Gisin, P. Grangiere, M. Grassl, S. Haroche, A. Imamoglu, A. Karlson, J. Kempe, L. Kouwenhoven, S. Kröll, G. Leuchs, M. Lewenstein, D. Loss, N. Lütkenhaus, S. Massar, J. E. Mooij, M. B. Plenio, E. Polzik, S. Popescu, G. Rempe, A. Sergienko, D. Suter, J. Twamley, G. Wendin, R. Werner, A. Winter, J. Wrachtrup, and A. Zeilinger. Quantum information processing and communication. *The European Physical Journal D - Atomic, Molecular, Optical and Plasma Physics*, 36(2):203–228, Nov 2005.

[68] Zhenshan Yang and J. E. Sipe. Generating entangled photons via enhanced spontaneous parametric downconversion in algaas microring resonators. *Opt. Lett.*, 32(22):3296–3298, Nov 2007.

[69] Juan P. Torres, K. Banaszek, and I.A. Walmsley. Chapter 5 - engineering nonlinear optic sources of photonic entanglement. volume 56 of *Progress in Optics*, pages 227–331. Elsevier, 2011.

[70] Christophe Couteau. Spontaneous parametric down-conversion. *Contemporary Physics*, 59(3):291–304, 2018.

[71] Marc Sansa, Martial Defoort, Ariel Brenac, Maxime Hermouet, Louise Banniard, Alexandre Fafin, Marc Gely, Christophe Masselon, Ivan Favero, Guillaume Jourdan, and Sébastien Hentz. Optomechanical mass spectrometry. *Nature Communications*, 11(1):3781, Jul 2020.

[72] E. Gavartin, P. Verlot, and T. J. Kippenberg. A hybrid on-chip optomechanical transducer for ultrasensitive force measurements. *Nature Nanotechnology*, 7(8):509–514, Aug 2012.

[73] G. Anetsberger, O. Arcizet, Q. P. Unterreithmeier, R. Rivière, A. Schliesser, E. M. Weig, J. P. Kotthaus, and T. J. Kippenberg. Near-field cavity optomechanics with nanomechanical oscillators. *Nature Physics*, 5(12):909–914, Dec 2009.

[74] Bei-Bei Li, Jan Bílek, Ulrich B. Hoff, Lars S. Madsen, Stefan Forstner, Varun Prakash, Clemens Schäfermeier, Tobias Gehring, Warwick P. Bowen, and Ulrik L. Andersen. Quantum enhanced optomechanical magnetometry. *Optica*, 5(7):850–856, Jul 2018.

[75] K.-J. Boller, A. Imamoğlu, and S. E. Harris. Observation of electromagnetically induced transparency. *Phys. Rev. Lett.*, 66:2593–2596, May 1991.

[76] Michael Fleischhauer, Atac Imamoglu, and Jonathan P. Marangos. Electromagnetically induced transparency: Optics in coherent media. *Rev. Mod. Phys.*, 77:633–673, Jul 2005.

[77] A. B. Matsko, Y. V. Rostovtsev, O. Kocharovskaya, A. S. Zibrov, and M. O. Scully. Nonadiabatic approach to quantum optical information storage. *Phys. Rev. A*, 64:043809, Sep 2001.

[78] Claudia Mewes and Michael Fleischhauer. Two-photon linewidth of light "stopping" via electromagnetically induced transparency. *Phys. Rev. A*, 66:033820, Sep 2002.

[79] A. S. Zibrov, A. B. Matsko, O. Kocharovskaya, Y. V. Rostovtsev, G. R. Welch, and M. O. Scully. Transporting and time reversing light via atomic coherence. *Phys. Rev. Lett.*, 88:103601, Feb 2002.

[80] Tarak Nath Dey and G. S. Agarwal. Storage and retrieval of light pulses at moderate powers. *Phys. Rev. A*, 67:033813, Mar 2003.

[81] Victor Fiore, Chunhua Dong, Mark C. Kuzyk, and Hailin Wang. Optomechanical light storage in a silica microresonator. *Phys. Rev. A*, 87:023812, Feb 2013.

[82] Yutaka Tabuchi, Seiichiro Ishino, Toyofumi Ishikawa, Rekishu Yamazaki, Koji Usami, and Yasunobu Nakamura. Hybridizing ferromagnetic magnons and microwave photons in the quantum limit. *Phys. Rev. Lett.*, 113:083603, Aug 2014.

[83] David E McClelland, Nergis Mavalvala, Yanbei Chen, and Roman Schnabel. Advanced interferometry, quantum optics and optomechanics in gravitational wave detectors. *Laser & Photonics Reviews*, 5(5):677–696, 2011.

[84] CF Ockeloen-Korppi, E Damskägg, J-M Pirkkalainen, M Asjad, AA Clerk, F Massel, MJ Woolley, and MA Sillanpää. Stabilized entanglement of massive mechanical oscillators. *Nature*, 556(7702):478–482, 2018.

[85] Subhadeep Chakraborty and Amarendra K Sarma. Entanglement dynamics of two coupled mechanical oscillators in modulated optomechanics. *Physical Review A*, 97(2):022336, 2018.

[86] Peter Rabl. Photon blockade effect in optomechanical systems. *Physical review letters*, 107(6):063601, 2011.

[87] Jie-Qiao Liao, Franco Nori, et al. Photon blockade in quadratically coupled optomechanical systems. *Physical Review A*, 88(2):023853, 2013.

[88] Hong Xie, Chang-Geng Liao, Xiao Shang, Ming-Yong Ye, and Xiu-Min Lin. Phonon blockade in a quadratically coupled optomechanical system. *Physical Review A*, 96(1):013861, 2017.

[89] Albert Schliesser, Georg Anetsberger, Rémi Rivière, Olivier Arcizet, and Tobias J Kippenberg. High-sensitivity monitoring of micromechanical vibration using optical whispering gallery mode resonators. *New Journal of Physics*, 10(9):095015, 2008.

[90] Jasper Chan, Amir H Safavi-Naeini, Jeff T Hill, Seán Meenehan, and Oskar Painter. Optimized optomechanical crystal cavity with acoustic radiation shield. *Applied Physics Letters*, 101(8):081115, 2012.

[91] Marcelo Davanco, Serkan Ates, Yuxiang Liu, and Kartik Srinivasan. Si 3 n 4 optomechanical crystals in the resolved-sideband regime. *Applied Physics Letters*, 104(4):041101, 2014.

[92] Houxun Miao, Kartik Srinivasan, and Vladimir Aksyuk. A microelectromechanically controlled cavity optomechanical sensing system. *New Journal of Physics*, 14(7):075015, 2012.

[93] EG Harris. Two-stream instability in a cold inhomogeneous plasma in a strong magnetic field. *The Physics of Fluids*, 7(10):1572–1577, 1964.

[94] Stephen E Harris, JE Field, and A Imamoğlu. Nonlinear optical processes using electromagnetically induced transparency. *Physical Review Letters*, 64(10):1107, 1990.

[95] K-J Boller, A Imamoğlu, and Stephen E Harris. Observation of electromagnetically induced transparency. *Physical Review Letters*, 66(20):2593, 1991.

[96] Michael Fleischhauer, Atac Imamoglu, and Jonathan P Marangos. Electromagnetically induced transparency: Optics in coherent media. *Reviews of modern physics*, 77(2):633, 2005.

[97] Lene Vestergaard Hau, Stephen E Harris, Zachary Dutton, and Cyrus H Behroozi. Light speed reduction to 17 metres per second in an ultracold atomic gas. *Nature*, 397(6720):594–598, 1999.

[98] Chien Liu, Zachary Dutton, Cyrus H Behroozi, and Lene Vestergaard Hau. Observation of coherent optical information storage in an atomic medium using halted light pulses. *Nature*, 409(6819):490–493, 2001.

[99] Peng-Cheng Ma, Jian-Qi Zhang, Yin Xiao, Mang Feng, and Zhi-Ming Zhang. Tunable double optomechanically induced transparency in an optomechanical system. *Physical Review A*, 90(4):043825, 2014.

[100] H Jing, Şahin K Özdemir, Z Geng, Jing Zhang, Xin-You Lü, Bo Peng, Lan Yang, and Franco Nori. Optomechanically-induced transparency in parity-time-symmetric microresonators. *Scientific reports*, 5(1):1–7, 2015.

[101] Hao Lü, Yajing Jiang, Yu-Zhu Wang, and Hui Jing. Optomechanically induced transparency in a spinning resonator. *Photonics Research*, 5(4):367–371, 2017.

[102] A. H. Safavi-Naeini, T. P. Mayer Alegre, J. Chan, M. Eichenfield, M. Winger, Q. Lin, J. T. Hill, D. E. Chang, and O. Painter. Electromagnetically induced transparency and slow light with optomechanics. *Nature*, 472(7341):69–73, Apr 2011.

[103] Bin Chen, Cheng Jiang, and Ka-Di Zhu. Slow light in a cavity optomechanical system with a bose-einstein condensate. *Physical Review A*, 83(5):055803, 2011.

[104] M Karuza, C Biancofiore, M Bawaj, C Molinelli, M Galassi, R Natali, P Tombesi, G Di Giuseppe, and D Vitali. Optomechanically induced transparency in a membrane-in-the-middle setup at room temperature. *Physical Review A*, 88(1):013804, 2013.

[105] John D Teufel, Dale Li, MS Allman, K Cicak, AJ Sirois, JD Whittaker, and RW Simmonds. Circuit cavity electromechanics in the strong-coupling regime. *Nature*, 471(7337):204–208, 2011.

[106] Sumei Huang and GS Agarwal. Electromagnetically induced transparency from two-phonon processes in quadratically coupled membranes. *Physical Review A*, 83(2):023823, 2011.

[107] Chenjun Wu, Yuhai Xiang, Shaoxing Qu, Yihu Song, and Qiang Zheng. Numerical study of millimeter-scale magnetorheological elastomer robot for undulatory swimming. *Journal of Physics D: Applied Physics*, 53(23):235402, 2020.

[108] Xiao-Yun Wang, Liu-Gang Si, Zeng-Xing Liu, Xiao-Hu Lu, and Ying Wu. Tunable optical amplification arising from blue detuning in a quadratically coupled optomechanical system. *JOSA B*, 36(5):1355–1362, 2019.

[109] Qing He, Fazal Badshah, Thamer Alharbi, Liping Li, and Linfeng Yang. Normal-mode splitting in a linear and quadratic optomechanical system with an ensemble of two-level atoms. *J. Opt. Soc. Am. B*, 37(1):148–156, Jan 2020.

[110] Xun-Wei Xu and Yong Li. Controllable optical output fields from an optomechanical system with mechanical driving. *Phys. Rev. A*, 92:023855, Aug 2015.

[111] Hiroyuki Suzuki, Eric Brown, and Ray Sterling. Nonlinear dynamics of an optomechanical system with a coherent mechanical pump: Second-order sideband generation. *Physical Review A*, 92(3):033823, 2015.

[112] Tian-Xiang Lu, Ya-Feng Jiao, Hui-Lai Zhang, Farhan Saif, and Hui Jing. Selective and switchable optical amplification with mechanical driven oscillators. *Physical Review A*, 100(1):013813, 2019.

[113] Yongchao Zhang, Kexun Yan, Zhangyin Zhai, Xintian Bian, Fen Zuo, Hualing Yu, and Cheng Jiang. Mechanical driving mediated slow light in a quadratically coupled optomechanical system. *JOSA B*, 37(3):650–657, 2020.

[114] Cheng Jiang, Yuanshun Cui, Zhangyin Zhai, Hualing Yu, Xiaowei Li, and Guibin Chen. Phase-controlled amplification and slow light in a hybrid optomechanical system. *Optics express*, 27(21):30473–30485, 2019.

[115] Cheng Jiang, Yuanshun Cui, Xintian Bian, Fen Zuo, Hualing Yu, and Guibin Chen. Phase-dependent multiple optomechanically induced absorption in multimode optomechanical systems with mechanical driving. *Physical Review A*, 94(2):023837, 2016.

[116] WZ Jia, LF Wei, Yong Li, and Yu-xi Liu. Phase-dependent optical response properties in an optomechanical system by coherently driving the mechanical resonator. *Physical Review A*, 91(4):043843, 2015.

[117] Sumei Huang. Double electromagnetically induced transparency and narrowing of probe absorption in a ring cavity with nanomechanical mirrors. *Journal of Physics B: Atomic, Molecular and Optical Physics*, 47(5):055504, 2014.

[118] PN Lebedev. *Annalen der Physik*, 6:433, 1901.

[119] Ernest Fox Nichols and Gordon Ferrie Hull. The pressure due to radiation. In *Proceedings of the American Academy of Arts and Sciences*, volume 38, pages 559–599. JSTOR, 1903.

[120] Jian-Qi Zhang, Yong Li, Mang Feng, and Yi Xu. Precision measurement of electrical charge with optomechanically induced transparency. *Physical Review A*, 86(5):053806, 2012.

[121] Sumei Huang and GS Agarwal. Normal-mode splitting in a coupled system of a nanomechanical oscillator and a parametric amplifier cavity. *Physical Review A*, 80(3):033807, 2009.

[122] Qiang Lin, Jessie Rosenberg, Darrick Chang, Ryan Camacho, Matt Eichenfield, Kerry J Vahala, and Oskar Painter. Coherent mixing of mechanical excitations in nano-optomechanical structures. *Nature Photonics*, 4(4):236–242, 2010.

[123] Sumei Huang and GS Agarwal. Normal-mode splitting and antibunching in stokes and anti-stokes processes in cavity optomechanics: radiation-pressure-induced four-wave-mixing cavity optomechanics. *Physical Review A*, 81(3):033830, 2010.

[124] Cheng Jiang, Bin Chen, and Ka-Di Zhu. Controllable nonlinear responses in a cavity electromechanical system. *JOSA B*, 29(2):220–225, 2012.

[125] Ramy El-Ganainy, Konstantinos G. Makris, Mercedeh Khajavikhan, Ziad H. Musslimani, Stefan Rotter, and Demetrios N. Christodoulides. Non-hermitian physics and pt symmetry. *Nature Physics*, 14(1):11–19, Jan 2018.

[126] W D Heiss. The physics of exceptional points. *Journal of Physics A: Mathematical and Theoretical*, 45(44):444016, oct 2012.

[127] K. G. Makris, R. El-Ganainy, D. N. Christodoulides, and Z. H. Musslimani. Beam dynamics in pt symmetric optical lattices. *Phys. Rev. Lett.*, 100:103904, Mar 2008.

[128] Z. H. Musslimani, K. G. Makris, R. El-Ganainy, and D. N. Christodoulides. Optical solitons in pt periodic potentials. *Phys. Rev. Lett.*, 100:030402, Jan 2008.

[129] A. Guo, G. J. Salamo, D. Duchesne, R. Morandotti, M. Volatier-Ravat, V. Aimez, G. A. Siviloglou, and D. N. Christodoulides. Observation of pt-symmetry breaking in complex optical potentials. *Phys. Rev. Lett.*, 103:093902, Aug 2009.

[130] Bo Peng, Şahin Kaya Özdemir, Fuchuan Lei, Faraz Monifi, Mariagiovanna Gianfreda, Gui Lu Long, Shanhui Fan, Franco Nori, Carl M. Bender, and Lan Yang. Parity–time-symmetric whispering-gallery microcavities. *Nature Physics*, 10(5):394–398, May 2014.

[131] Stefano Longhi. Invisibility in -symmetric complex crystals. *Journal of Physics A: Mathematical and Theoretical*, 44(48):485302, nov 2011.

[132] Liang Feng, Ye-Long Xu, William S. Fegadolli, Ming-Hui Lu, José E. B. Oliveira, Vilson R. Almeida, Yan-Feng Chen, and Axel Scherer. Experimental demonstration of a unidirectional reflectionless parity-time metamaterial at optical frequencies. *Nature Materials*, 12(2):108–113, Feb 2013.

[133] Tamar Goldzak, Alexei A. Mailybaev, and Nimrod Moiseyev. Light stops at exceptional points. *Phys. Rev. Lett.*, 120:013901, Jan 2018.

[134] Xufeng Zhang, Chang-Ling Zou, Liang Jiang, and Hong X. Tang. Cavity magnomechanics. *Science Advances*, 2(3):e1501286, 2016.

[135] Xufeng Zhang, Chang-Ling Zou, Liang Jiang, and Hong X. Tang. Strongly coupled magnons and cavity microwave photons. *Phys. Rev. Lett.*, 113:156401, Oct 2014.

[136] Guo-Qiang Zhang and J. Q. You. Higher-order exceptional point in a cavity magnonics system. *Phys. Rev. B*, 99:054404, Feb 2019.

[137] C. A. Potts, E. Varga, V. A. S. V. Bittencourt, S. Viola Kusminskiy, and J. P. Davis. Dynamical backaction magnomechanics. *Phys. Rev. X*, 11:031053, Sep 2021.

[138] Jie Li, Shi-Yao Zhu, and G. S. Agarwal. Magnon-photon-phonon entanglement in cavity magnomechanics. *Phys. Rev. Lett.*, 121:203601, Nov 2018.

[139] Jie Li and Simon Gröblacher. Entangling the vibrational modes of two massive ferromagnetic spheres using cavity magnomechanics. *Quantum Science and Technology*, 6(2):024005, feb 2021.

[140] Jie Li, Shi-Yao Zhu, and G. S. Agarwal. Squeezed states of magnons and phonons in cavity magnomechanics. *Phys. Rev. A*, 99:021801(R), Feb 2019.

[141] Bijita Sarma, Thomas Busch, and Jason Twamley. Cavity magnomechanical storage and retrieval of quantum states. *New Journal of Physics*, 23(4):043041, apr 2021.

[142] Dengke Zhang, Xiao-Qing Luo, Yi-Pu Wang, Tie-Fu Li, and J. Q. You. Observation of the exceptional point in cavity magnon-polaritons. *Nature Communications*, 8(1):1368, Nov 2017.

[143] Jie Zhao, Yulong Liu, Longhao Wu, Chang-Kui Duan, Y-X Liu, and Jiangfeng Du. Observation of anti-$\mathcal{PT}$-symmetry phase transition in the magnon-cavity-magnon coupled system. *Phys. Rev. Appl.*, 13:014053, Jan 2020.

[144] Fei Wang and Chengdeng Gou. Magnon-induced absorption via quantum interference. *Opt. Lett.*, 48(5):1164–1167, Mar 2023.

[145] Cui Kong, Hao Xiong, and Ying Wu. Magnon-induced nonreciprocity based on the magnon kerr effect. *Phys. Rev. Appl.*, 12:034001, Sep 2019.

[146] Kamran Ullah, M. Tahir Naseem, and Özgür E. Müstecaplioğlu. Tunable multiwindow magnomechanically induced transparency, fano resonances, and slow-to-fast light conversion. *Phys. Rev. A*, 102:033721, Sep 2020.

[147] Xiyun Li, Wen-Xing Yang, Tao Shui, Ling Li, Xin Wang, and Zhen Wu. Phase control of the transmission in cavity magnomechanical system with magnon driving. *Journal of Applied Physics*, 128(23):233101, 2020.

[148] Jayakrishnan M. P. Nair, Debsuvra Mukhopadhyay, and Girish S. Agarwal. Cavity-mediated level attraction and repulsion between magnons. *Phys. Rev. B*, 105:214418, Jun 2022.

[149] Sanket Das and Tarak N. Dey. Phase-dependent controllable field generation in a ring cavity resonator. *J. Opt. Soc. Am. B*, 39(3):859–868, Mar 2022.

[150] M. H. Anderson, J. R. Ensher, M. R. Matthews, C. E. Wieman, and E. A. Cornell. Observation of bose-einstein condensation in a dilute atomic vapor. *Science*, 269(5221):198–201, 1995.

[151] Kendall B Davis, M-O Mewes, Michael R Andrews, Nicolaas J van Druten, Dallin S Durfee, DM Kurn, and Wolfgang Ketterle. Bose-einstein condensation in a gas of sodium atoms. *Physical review letters*, 75(22):3969, 1995.

[152] Anthony J. Leggett. Bose-einstein condensation in the alkali gases: Some fundamental concepts. *Rev. Mod. Phys.*, 73:307–356, Apr 2001.

[153] SI Vilchynskyy, AI Yakimenko, KO Isaieva, and AV Chumachenko. The nature of superfluidity and bose-einstein condensation: From liquid 4he to dilute ultracold atomic gases. *Low Temperature Physics*, 39(9):724–740, 2013.

[154] Takahiro Hashimoto, Yuichi Ota, Akihiro Tsuzuki, Tsubaki Nagashima, Akiko Fukushima, Shigeru Kasahara, Yuji Matsuda, Kohei Matsuura, Yuta Mizukami, Takasada Shibauchi, Shik Shin, and Kozo Okazaki. Bose-einstein condensation superconductivity induced by disappearance of the nematic state. *Science Advances*, 6(45):eabb9052, 2020.

[155] Alexander L. Fetter. Rotating trapped bose-einstein condensates. *Rev. Mod. Phys.*, 81:647–691, May 2009.

[156] Erich J. Mueller, Paul M. Goldbart, and Yuli Lyanda-Geller. Multiply connected bose-einstein-condensed alkali-metal gases: Current-carrying states and their decay. *Phys. Rev. A*, 57:R1505–R1508, Mar 1998.

[157] Arnab Das, Jacopo Sabbatini, and Wojciech H. Zurek. Winding up superfluid in a torus via bose einstein condensation. *Scientific Reports*, 2(1):352, Apr 2012.

[158] Scott Beattie, Stuart Moulder, Richard J. Fletcher, and Zoran Hadzibabic. Persistent currents in spinor condensates. *Phys. Rev. Lett.*, 110:025301, Jan 2013.

[159] Yanliang Guo, Romain Dubessy, Mathieu de Goër de Herve, Avinash Kumar, Thomas Badr, Aurélien Perrin, Laurent Longchambon, and Hélène Perrin. Supersonic rotation of a superfluid: A long-lived dynamical ring. *Phys. Rev. Lett.*, 124:025301, Jan 2020.

[160] C. Ryu, M. F. Andersen, P. Cladé, Vasant Natarajan, K. Helmerson, and W. D. Phillips. Observation of persistent flow of a bose-einstein condensate in a toroidal trap. *Phys. Rev. Lett.*, 99:260401, Dec 2007.

[161] A. Ramanathan, K. C. Wright, S. R. Muniz, M. Zelan, W. T. Hill, C. J. Lobb, K. Helmerson, W. D. Phillips, and G. K. Campbell. Superflow in a toroidal bose-einstein condensate: An atom circuit with a tunable weak link. *Phys. Rev. Lett.*, 106:130401, Mar 2011.

[162] G. Edward Marti, Ryan Olf, and Dan M. Stamper-Kurn. Collective excitation interferometry with a toroidal bose-einstein condensate. *Phys. Rev. A*, 91:013602, Jan 2015.

[163] C. Ryu, P. W. Blackburn, A. A. Blinova, and M. G. Boshier. Experimental realization of josephson junctions for an atom squid. *Phys. Rev. Lett.*, 111:205301, Nov 2013.

[164] Saurabh Pandey, Hector Mas, Georgios Vasilakis, and Wolf von Klitzing. Atomtronic matter-wave lensing. *Phys. Rev. Lett.*, 126:170402, Apr 2021.

[165] L. Amico, M. Boshier, G. Birkl, A. Minguzzi, C. Miniatura, L.-C. Kwek, D. Aghamalyan, V. Ahufinger, D. Anderson, N. Andrei, A. S. Arnold, M. Baker, T. A. Bell, T. Bland, J. P. Brantut, et al. Roadmap on atomtronics: State of the art and perspective. *AVS Quantum Science*, 3(3):039201, Aug 2021.

[166] Rina Kanamoto, Lincoln D. Carr, and Masahito Ueda. Topological winding and unwinding in metastable bose-einstein condensates. *Phys. Rev. Lett.*, 100:060401, Feb 2008.

[167] L. Corman, L. Chomaz, T. Bienaimé, R. Desbuquois, C. Weitenberg, S. Nascimbène, J. Dalibard, and J. Beugnon. Quench-induced supercurrents in an annular bose gas. *Phys. Rev. Lett.*, 113:135302, Sep 2014.

[168] Stephen Eckel, Jeffrey G. Lee, Fred Jendrzejewski, Noel Murray, Charles W. Clark, Christopher J. Lobb, William D. Phillips, Mark Edwards, and Gretchen K. Campbell. Hysteresis in a quantized superfluid 'atomtronic' circuit. *Nature*, 506(7487):200–203, Feb 2014.

[169] Yi-Hsieh Wang, A Kumar, F Jendrzejewski, Ryan M Wilson, Mark Edwards, S Eckel, G K Campbell, and Charles W Clark. Resonant wavepackets and shock waves in an atomtronic squid. *New Journal of Physics*, 17(12):125012, dec 2015.

[170] K. C. Wright, R. B. Blakestad, C. J. Lobb, W. D. Phillips, and G. K. Campbell. Driving phase slips in a superfluid atom circuit with a rotating weak link. *Phys. Rev. Lett.*, 110:025302, Jan 2013.

[171] Stuart Moulder, Scott Beattie, Robert P. Smith, Naaman Tammuz, and Zoran Hadzibabic. Quantized supercurrent decay in an annular bose-einstein condensate. *Phys. Rev. A*, 86:013629, Jul 2012.

[172] Patrik Öhberg and Ewan M. Wright. Quantum time crystals and interacting gauge theories in atomic bose-einstein condensates. *Phys. Rev. Lett.*, 123:250402, Dec 2019.

[173] J. J. Cooper, D. W. Hallwood, and J. A. Dunningham. Entanglement-enhanced atomic gyroscope. *Phys. Rev. A*, 81:043624, Apr 2010.

[174] S. Eckel, A. Kumar, T. Jacobson, I. B. Spielman, and G. K. Campbell. A rapidly expanding bose-einstein condensate: An expanding universe in the lab. *Phys. Rev. X*, 8:021021, Apr 2018.

[175] A Kumar, N Anderson, W D Phillips, S Eckel, G K Campbell, and S Stringari. Minimally destructive, doppler measurement of a quantized flow in a ring-shaped bose–einstein condensate. *New Journal of Physics*, 18(2):025001, feb 2016.

[176] D. V. Freilich, D. M. Bianchi, A. M. Kaufman, T. K. Langin, and D. S. Hall. Real-time dynamics of single vortex lines and vortex dipoles in a bose-einstein condensate. *Science*, 329(5996):1182–1185, 2010.

[177] Pardeep Kumar, Tushar Biswas, Kristian Feliz, Rina Kanamoto, M.-S. Chang, Anand K. Jha, and M. Bhattacharya. Cavity optomechanical sensing and manipulation of an atomic persistent current. *Phys. Rev. Lett.*, 127:113601, Sep 2021.

[178] Nalinikanta Pradhan, Pardeep Kumar, Rina Kanamoto, Tarak Nath Dey, M. Bhattacharya, and Pankaj Kumar Mishra. Cavity optomechanical detection of persistent currents and solitons in a bosonic ring condensate. *Phys. Rev. Res.*, 6:013104, Jan 2024.

[179] Nalinikanta Pradhan, Pardeep Kumar, Rina Kanamoto, Tarak Nath Dey, M. Bhattacharya, and Pankaj Kumar Mishra. Ring bose-einstein condensate in a cavity: Chirality detection and rotation sensing. *Phys. Rev. A*, 109:023524, Feb 2024.

[180] Markus Aspelmeyer, Tobias J. Kippenberg, and Florian Marquardt. Cavity optomechanics. *Rev. Mod. Phys.*, 86:1391–1452, Dec 2014.

[181] Florian Marquardt, Joe P. Chen, A. A. Clerk, and S. M. Girvin. Quantum theory of cavity-assisted sideband cooling of mechanical motion. *Phys. Rev. Lett.*, 99:093902, Aug 2007.

[182] M. Paternostro, D. Vitali, S. Gigan, M. S. Kim, C. Brukner, J. Eisert, and M. Aspelmeyer. Creating and probing multipartite macroscopic entanglement with light. *Phys. Rev. Lett.*, 99:250401, Dec 2007.

[183] Kenan Qu and G S Agarwal. Strong squeezing via phonon mediated spontaneous generation of photon pairs. *New Journal of Physics*, 16(11):113004, oct 2014.

[184] J. Aasi, J. Abadie, B. P. Abbott, R. Abbott, T. D. Abbott, M. R. Abernathy, C. Adams, T. Adams, P. Addesso, R. X. Adhikari, C. Affeldt, O. D. Aguiar, P. Ajith, B. Allen, E. Amador Ceron, et al. Enhanced sensitivity of the ligo gravitational wave detector by using squeezed states of light. *Nature Photonics*, 7(8):613–619, Aug 2013.

[185] D. Ganapathy, W. Jia, M. Nakano, V. Xu, N. Aritomi, T. Cullen, N. Kijbunchoo, S. E. Dwyer, A. Mullavey, L. McCuller, R. Abbott, I. Abouelfettouh, R. X. Adhikari, A. Ananyeva, S. Appert, et al. Broadband quantum enhancement of the ligo detectors with frequency-dependent squeezing. *Phys. Rev. X*, 13:041021, Oct 2023.

[186] Christian Peuntinger, Bettina Heim, Christian R. Müller, Christian Gabriel, Christoph Marquardt, and Gerd Leuchs. Distribution of squeezed states through an atmospheric channel. *Phys. Rev. Lett.*, 113:060502, Aug 2014.

[187] Chang-Woo Lee, Jae Hoon Lee, and Hyojun Seok. Squeezed-light-driven force detection with an optomechanical cavity in a mach–zehnder interferometer. *Scientific Reports*, 10(1):17496, Oct 2020.

[188] B. J. Lawrie, P. D. Lett, A. M. Marino, and R. C. Pooser. Quantum sensing with squeezed light. *ACS Photonics*, 6(6):1307–1318, Jun 2019.

[189] H Shi and M Bhattacharya. Optomechanics based on angular momentum exchange between light and matter. *Journal of Physics B: Atomic, Molecular and Optical Physics*, 49(15):153001, jun 2016.

[190] M. Bhattacharya. Rotational cavity optomechanics. *J. Opt. Soc. Am. B*, 32(5):B55–B60, May 2015.

[191] M. Bhattacharya and P. Meystre. Using a laguerre-gaussian beam to trap and cool the rotational motion of a mirror. *Phys. Rev. Lett.*, 99:153603, Oct 2007.

[192] M. Bhattacharya, P.-L. Giscard, and P. Meystre. Entanglement of a laguerre-gaussian cavity mode with a rotating mirror. *Phys. Rev. A*, 77:013827, Jan 2008.

[193] M. Bhattacharya, P.-L. Giscard, and P. Meystre. Entangling the rovibrational modes of a macroscopic mirror using radiation pressure. *Phys. Rev. A*, 77:030303, Mar 2008.

[194] B. Rogers, N. Lo Gullo, G. De Chiara, G. M. Palma, and M. Paternostro. Hybrid optomechanics for quantum technologies. *Quantum Measurements and Quantum Metrology*, 2(1):000010247820140002, 2014.

[195] Ondřej Černotík, Claudiu Genes, and Aurélien Dantan. Interference effects in hybrid cavity optomechanics. *Quantum Science and Technology*, 4(2):024002, jan 2019.

[196] Shabir Barzanjeh, André Xuereb, Simon Gröblacher, Mauro Paternostro, Cindy A. Regal, and Eva M. Weig. Optomechanics for quantum technologies. *Nature Physics*, 18(1):15–24, Jan 2022.

[197] C. A. Regal, J. D. Teufel, and K. W. Lehnert. Measuring nanomechanical motion with a microwave cavity interferometer. *Nature Physics*, 4(7):555–560, Jul 2008.

[198] Anil Kumar Chauhan and Asoka Biswas. Atom-assisted quadrature squeezing of a mechanical oscillator inside a dispersive cavity. *Phys. Rev. A*, 94:023831, Aug 2016.

[199] Levi P. Neukirch, Eva von Haartman, Jessica M. Rosenholm, and A. Nick Vamivakas. Multi-dimensional single-spin nano-optomechanics with a levitated nanodiamond. *Nature Photonics*, 9(10):653–657, Oct 2015.

[200] Olivier Morizot, Yves Colombe, Vincent Lorent, Hélène Perrin, and Barry M. Garraway. Ring trap for ultracold atoms. *Phys. Rev. A*, 74:023617, Aug 2006.

[201] Rina Kanamoto, Hiroki Saito, and Masahito Ueda. Quantum phase transition in one-dimensional bose-einstein condensates with attractive interactions. *Phys. Rev. A*, 67:013608, Jan 2003.

[202] A. Schliesser, P. Del'Haye, N. Nooshi, K. J. Vahala, and T. J. Kippenberg. Radiation pressure cooling of a micromechanical oscillator using dynamical backaction. *Phys. Rev. Lett.*, 97:243905, Dec 2006.

[203] O. Arcizet, P.-F. Cohadon, T. Briant, M. Pinard, and A. Heidmann. Radiation-pressure cooling and optomechanical instability of a micromirror. *Nature*, 444(7115):71–74, Nov 2006.

[204] Edmund X. DeJesus and Charles Kaufman. Routh-hurwitz criterion in the examination of eigenvalues of a system of nonlinear ordinary differential equations. *Phys. Rev. A*, 35:5288–5290, Jun 1987.

[205] Xunnong Xu and Jacob M. Taylor. Squeezing in a coupled two-mode optomechanical system for force sensing below the standard quantum limit. *Phys. Rev. A*, 90:043848, Oct 2014.

[206] Andrei Militaru, Massimiliano Rossi, Felix Tebbenjohanns, Oriol Romero-Isart, Martin Frimmer, and Lukas Novotny. Ponderomotive squeezing of light by a levitated nanoparticle in free space. *Phys. Rev. Lett.*, 129:053602, Jul 2022.

[207] Lorenzo Magrini, Victor A. Camarena-Chávez, Constanze Bach, Aisling Johnson, and Markus Aspelmeyer. Squeezed light from a levitated nanoparticle at room temperature. *Phys. Rev. Lett.*, 129:053601, Jul 2022.

[208] R. Ghobadi, A. R. Bahrampour, and C. Simon. Quantum optomechanics in the bistable regime. *Phys. Rev. A*, 84:033846, Sep 2011.

[209] Jingwen Zhou, Jihong Tang, Yaling Yin, Yong Xia, and Jianping Yin. Fundamental probing limit on the high-order orbital angular momentum of light. *Opt. Express*, 32(4):5339–5352, Feb 2024.

[210] Ali Mardan Dezfouli, Denis Abramović, Mario Rakić, and Hrvoje Skenderović. Detection of the orbital angular momentum state of light using sinusoidally shaped phase grating. *Applied Physics Letters*, 120(19):191106, 05 2022.

[211] Wenjun Ni, Rui Liu, Chunyong Yang, Yongsheng Tian, Jin Hou, Perry Ping Shum, and Shaoping Chen. Annular phase grating-assisted recording of an ultrahigh-order optical orbital angular momentum. *Opt. Express*, 30(21):37526–37535, Oct 2022.

[212] Jonathan Pinnell, Valeria Rodríguez-Fajardo, and Andrew Forbes. Probing the limits of orbital angular momentum generation and detection with spatial light modulators. *Journal of Optics*, 23(1):015602, dec 2020.

[213] Chao He, Yijie Shen, and Andrew Forbes. Towards higher-dimensional structured light. *Light: Science & Applications*, 11(1):205, Jul 2022.

[214] Gerardo Adesso and Fabrizio Illuminati. Entanglement in continuous-variable systems: recent advances and current perspectives. *Journal of Physics A: Mathematical and Theoretical*, 40(28):7821, jun 2007.

[215] Gerardo Adesso and Fabrizio Illuminati. Continuous variable tangle, monogamy inequality, and entanglement sharing in gaussian states of continuous variable systems. *New Journal of Physics*, 8(1):15, jan 2006.

List of publications

The following are described in this thesis:

- Sanket Das and Tarak N. Dey, "Phase-dependent controllable field generation in a ring cavity resonator", J. Opt. Soc. Am. B **39**(3), 859-868 (2022).
- Sanket Das, Subhadeep Chakraborty, and Tarak N. Dey, "Gain-assisted controllable fast-light generation in cavity magnomechanics", Phys. Rev. A **108** 033517 (2023).
- Sanket Das, Pardeep Kumar, M. Bhattacharya, and Tarak N. Dey, "Hybrid Rotational Cavity Optomechanics Using Atomic Superfluid in a Ring", arXiv:2407.01990 [quant-ph]

The following is not described in this thesis:

- Sreeshna Subhash, Sanket Das, Tarak Nath Dey, Yong Li, and Sankar Davuluri,"Enhancing the force sensitivity of a squeezed light optomechanical interferometer", Opt. Express 31(**1**), 177-191 (2023).

Conferences and schools attended

- **SERB School on Frontiers in Quantum Optics**, Organized by the Dept. of physics, IIT Guwahati during 1-19 December 2017.
- **XLII Annual Meeting of the Optical Society of India, OSI- International Symposium of Optics**, Organized by Indian Institute of Technology Kanpur, Kanpur- 208016, Uttar Pradesh, India in September 2018.
- **IEEE workshop on recent advances in photonics**, Organized by Indian Institute of Technology Guwahati, Guwahati-781039, India in December 2019.
- **Raman Conference on Light and Matter Physics** Organized by Raman Research Institute, Bangalore, India in August 2023.